

Numerical Simulation of the Heating of X-Ray Bright Points in the Solar Corona

Dissertation

zur Erlangung des mathematisch-naturwissenschaftlichen Doktorgrades

“Doctor rerum naturalium”

der Georg-August-Universität Göttingen

vorgelegt von

Setareh Javadi Dogaheh

aus Tehran / Iran

Göttingen 2010

Bibliografische Information der Deutschen Nationalbibliothek

Die Deutsche Nationalbibliothek verzeichnet diese Publikation in der Deutschen Nationalbibliografie; detaillierte bibliografische Daten sind im Internet über <http://dnb.d-nb.de> abrufbar.

Referent: Prof. Dr. S. Dreizler

Korreferent: Prof. Dr. J. Buechner

Tag der mündlichen Prüfung: 24. September 2010

ISBN 978-3-942171-42-7

uni-edition GmbH 2011

<http://www.uni-edition.de>

© Setareh Javadi Dogahch



This work is distributed under a
Creative Commons Attribution 3.0 License

Printed in Germany

Contents

1	Introduction	7
1.1	Coronal Bright Point properties and models	7
1.2	Modelings of the coronal heating	13
1.3	The scope of this work	20
2	The MHD model	23
2.1	MHD equations	23
2.2	Resistivity models	25
2.3	Normalization values	27
2.3.1	Transport coefficients	27
2.3.2	Normalized equations	29
2.4	Initial conditions	29
2.5	Boundary conditions	32
2.6	Simulation properties	33
2.7	Diagnostic methods	33
3	About the relative importance of compressional heating and current dissipation for the formation of coronal X-ray Bright Points	35
3.1	Simulation model	36
3.1.1	Equations	36
3.1.2	Simulation box and normalization	37
3.1.3	Resistivity models	38
3.1.4	Initial and boundary conditions	39
3.2	Simulation setup	40
3.3	Simulation results	41
3.4	Energy balance	42
3.4.1	Global effect of current dissipation and compression	42
3.4.2	Influence of different resistivity models	48
3.4.3	Flux tube heating	52
3.5	Summary and discussion	55
4	The consequences of the consideration of heat conduction and radiative loss in the formation of a coronal X-ray Bright Point	57
4.1	The model	59
4.2	Initial state	60
4.3	Simulation results	60

4.4	Effect of the heat conduction and radiative loss	63
4.5	Analysis of the energy transport	66
4.6	Analysis of the thermal balance along magnetic flux tubes	69
4.7	Squashing factor calculations	72
4.8	Conclusions	74
5	Discussion and outlook	81
A	Normalization of the energy equation	83
B	Derivation of the energy transport equations	85
C	Resistivity values	87
	Bibliography	89
	Publications	95
	Acknowledgements	97
	Curriculum Vitae	99

Summary

The goal of this thesis work is the investigation of the heating of X-ray Bright Points (BPs) in the solar corona by means of three-dimensional magnetohydrodynamics (MHD) numerical simulation.

- BPs are an important feature of solar coronal heating whose understanding is still not achieved.
- We used the most advanced observation of BP properties obtained by the Japanese spacecraft, "Hinode".
- For the numerical simulation we used LINMOD3D numerical simulation model, which was developed by Büchner (2004a,b) in the group of 'Theory and simulation of solar system plasmas', at the Max-Planck-Institute for Solar System Research. The model contains a compressible and resistive plasma. To obtain the initial magnetic field an extrapolation of the observed line-of sight (LOS) component of photospheric magnetic field is performed. The simulation code was adjusted to include the observed photospheric magnetic field corresponding an X-ray Bright point (BP) observed a time by the Hinode spacecraft.
- We consider a rectangular simulation box including the BP region that covers the solar atmosphere from the photosphere to about 15 Mm inside the solar corona. The horizontal size corresponds to an area of $46.4 \text{ Mm} \times 46.4 \text{ Mm}$ at the solar surface. The magnetic features associated to this BP are properly covered.
- To investigate the dynamic evolution of the solar atmosphere above a BP, we modified the boundary conditions according to the solar observations. A local-correlation-tracking (LCT) was carried out to obtain the plasma velocity at the photosphere. Using this velocities to perturb the plasma, the location of the current concentrations in the simulation box were found, which coincide with the location of the observed temperature enhancement in an arc-shaped structure above the main opposite photospheric magnetic flux concentration associated to the BP.
- We investigated which role Joule dissipation could play as a heating mechanism in the MHD modelling of the solar corona. A comparison of the role of different contributions in the energy (temperature) balance, namely the work done by the Lorentz force, pressure gradient force and Joule heating, indicated surprisingly the importance of adiabatic compression for the temperature enhancement in the BP region. In contrary, the role of Joule dissipation appeared to be rather small. We

tested this result for different resistivity models. The results showed that the pressure gradient force is acting more actively than the current dissipation for increasing the thermal energy, independent of the resistivity model.

- For a better localization of the heating processes we determined the differential flux tube integrated contributions to the energy balance. This way we could proof that the temperature enhancements follows the pattern of the energy change rates and the corresponding forces involved. We came to the conclusion that the upward energy flow is due to the plasma motion at the footpoints of the coronal magnetic fields, which energizes the plasma confined in coronal magnetic flux tubes and makes them rise to the higher corona.
- Moving towards a more realistic model of the coronal heating, we studied the influence of heat conduction along the magnetic field lines as well as the influence of radiative losses for the case of optically thin plasmas, on the heat energy and temperature distribution along coronal magnetic flux tubes. This way we could get temperature enhancement that are by some thousand Kelvins less than the case that does not include these two effects. However, The results before and after the inclusion of heat conduction and radiative cooling are qualitatively similar. This indicates that the dynamic evolution of the plasma is governed by magnetic structure mainly. Although heat conduction results in downflow of the heat from the upper atmosphere and therefore, in a less steep temperature gradient in the transition region. This leads to higher densities at a lower latitude and higher values of heat would be radiated away. To maintain the coronal temperature an additional heating source is needed to balance the heat loss mechanisms.

1 Introduction

1.1 Coronal Bright Point properties and models

Coronal Bright Points (BPs) are small coronal features, ($30'' - 40''$) of locally enhanced emission in X-ray and EUV seen in the sun. They were first observed in X-rays by Vaiana et al., (1970) but later also in radio and EUV wavelengths. Their average lifetime, see Fig. 1.1, varies from 8 hrs determined by X-ray observations by (Golub et al., 1974) and it goes to 20 hrs in EUV lines (Zhang et al., 2001). Using higher resolution observations (Scherrer et al., 1979) could show that BPs consist of a some miniature loops at different temperatures. These bright loops that evolve on timescales of ~ 6 min was shown by (Ugarte-urra., 2004) that experience intensity oscillations.

BPs are distributed over all latitudes and longitudes of the quiet-sun corona, as shown in Fig. 1.2 taken from (Golub et al., 1974). They appear in both maximum and minimum of solar activity and are likely to contribute actively to maintaining the coronal temperature during the solar activity minima.

BPs are known to be closely linked to small scale photospheric magnetic features with opposite polarities, (Krieger et al., 1971, Brown et al., 2001). The occurrence of BPs was found to be more likely close to the boundaries of the super-granulation magnetic network. However approximately one-third of the BPs that appear per day, are due to emerging bipolar fluxes. The rest is related to magnetic bipoles associated with cancelling flux, known as Cancelling Magnetic Features (CMFs), Harvey 1985.

First theoretical models of CMFs involving magnetic reconnection was developed by e.g., Priest et al., 1994, Parnell et al., 1994, Longcope 1998. In the cancelling magnetic feature model by Priest et al., 1994 two magnetic flux regions of opposite polarity that are initially not connected, interact through three phases, namely:

- Pre-interaction phase
- Interaction phase
- Cancellation phase

These phases are depicted in a two-dimensional image, (see Fig. 1.3 taken from Priest et al., 1994). They correspond to the occurrence of the BP to the reconnection of the magnetic field associated with two opposite magnetic polarities that are assumed to be of the same strength and located in a uniform overlying field at photospheric height, (see Fig. 1.4). The process start with pre-interaction phase at which the two magnetically unconnected fragments with opposite polarities begin to approach each other until their opposite directed magnetic fields come into contact at a null point (in an 2D image). In

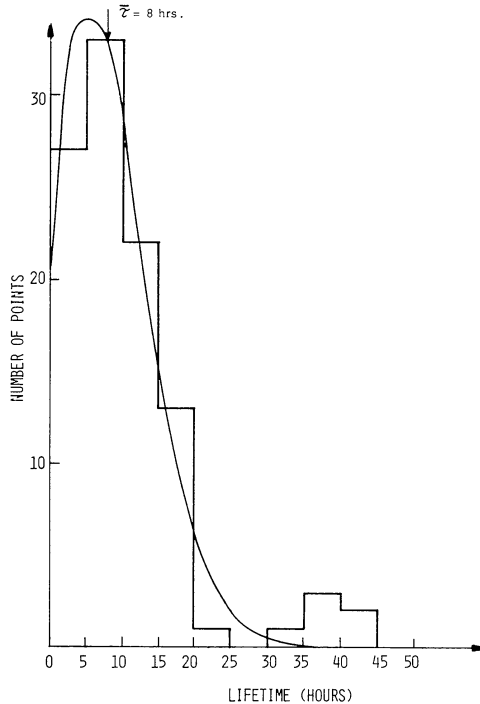


Figure 1.1: Number of bright points is shown versus their lifetime. The lifetime distribution is fitted by a Poisson distribution with a mean lifetime of 8 hrs, (Golub et al., 1974)

the interaction phase the null point start to become an X-point and result in magnetic reconnection. The X-point then is supposed to rise up from photosphere into the corona and the local heating of the plasma and the brightening can appear in the form of an X-ray BP. The BP can last for some hours depending on its associated photospheric driver. The cancellation phase comes as the strength of the magnetic fragments decreases and the X-point moves down until it disappears finally in the photosphere, when one or both of the fragments are completely cancelled. This stage can end up with formation of two horizontal flux tube locating above and below the photosphere, (see bottom panel of Fig. 1.3). A mathematical model to describe this process is given at Priest et al., 1994, at which the potential field of the two equal opposite magnetic polarities are initially disconnected. The poles start to approach slowly, in a way that the overlying field can evolve through a piecewise configurations. When the poles are in the interaction distance, the null point form and a vertical current sheet forms that is extended to a certain height, shown by "h" in the third panel of Fig. 1.4. At this point when the free energy stored in the magnetic

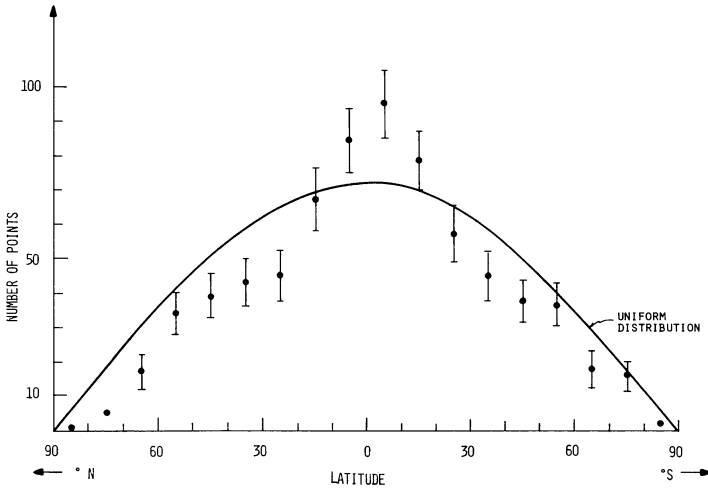


Figure 1.2: Latitude distribution of BPs, (from (Golub et al., 1974)).

field lines passes the purely potential limit the excess energy is released via magnetic reconnection and converted to heat by producing an X-ray BP.

This two dimensional model was extended by Parnell et al., 1994 to a three dimensional case at which the strength of the magnetic fragments were also different. The other scenario was suggested by Longcope 1998, at which BP was powered by reconnection along separator field lines rather than an X-point, Fig. 1.5.

Brown et al., 2001 studied the complete lifetime of a BP in more details using the high resolution observations. They could associate different stages of the evolution of this BP with different patterns of motion of the positive and negative fragments of a bipole. These motions include fragmentation and coalescence of the fragments in the early stage of formation of BP. The correspond the sigmoid phase and twisting of BP at its half life time to the rotation and translation of the magnetic fragments in the photosphere. The sigmoid can become unstable when the twist passes a critical degree, and the π -phase of BP starts then. In the π -phase the structure is converted to smaller loops that fades quickly and by a large drop of the fluxes associated to the magnetic bipole, the lifetime of the BP is over. Although this study was done for a sample BP only, the more complicated patterns of motions of the magnetic fragments for this case can imply the generation of currents that the usual Joule heating cannot explain them. The energy dissipation in this case takes place in smaller scales where microphysical considerations are needed to explain the high values of dissipation.

A numerical study of the cancelling magnetic features (CMEs) was performed using a two dimensional magnetohydrodynamics (MHD) simulation model by Von Rekowski B., Parnell C. E., Prist E. R., 2006a, where starting from partly connected bipolar sources they could follow the process until the cancellation was completed. In Von Rekowski B.,

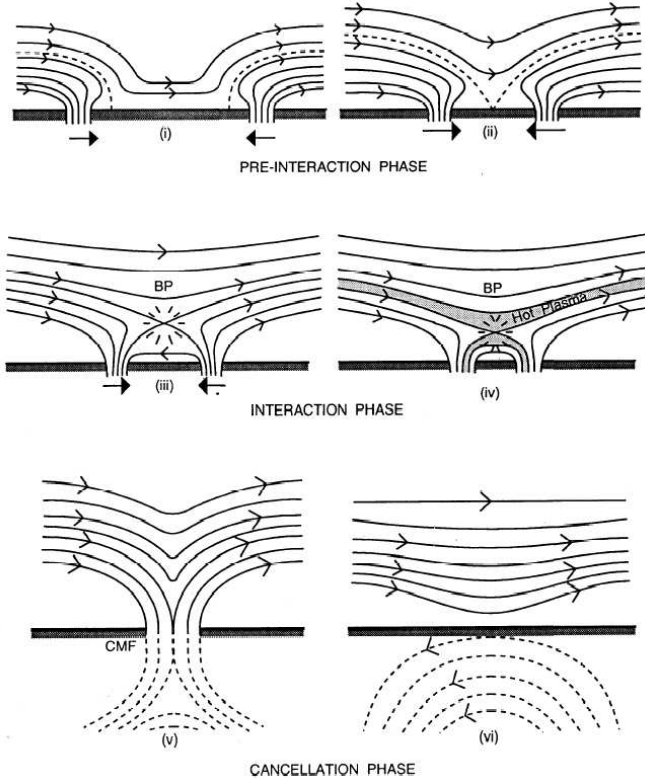


Figure 1.3: Three stages of the approach and interaction of the two equal opposite magnetic fragments, taken from Priest et al., 1994

Parnell C. E., Priest E. R., 2006b their simulation setup start for two initially disconnected bipoles, following the theoretical model of Priest et al., 1994, and they consider the case of unequal sources. A comparison is made there between the dynamically computed magnetic fields from the numerical model with the potential field from the converging bipole sources. A horizontal flow at the base of their simulation can move the inner opposite polarity magnetic bipolar sources that are footpoints of two coronal loops. This convergence of bipoles drives the system by triggering the cancellation of bipole and coronal reconnection and leads to coronal heating in the form of an X-ray BP, accompanied by loop brightening. However, the movement of the magnetic features in their simulation only includes the a simple pattern, either emerging or cancelling.

The role of the plasma motion to energize the BP in the regions of strongly diverging magnetic fields was first addressed by (Büchner et al. 2004a,b). Unlike the existing

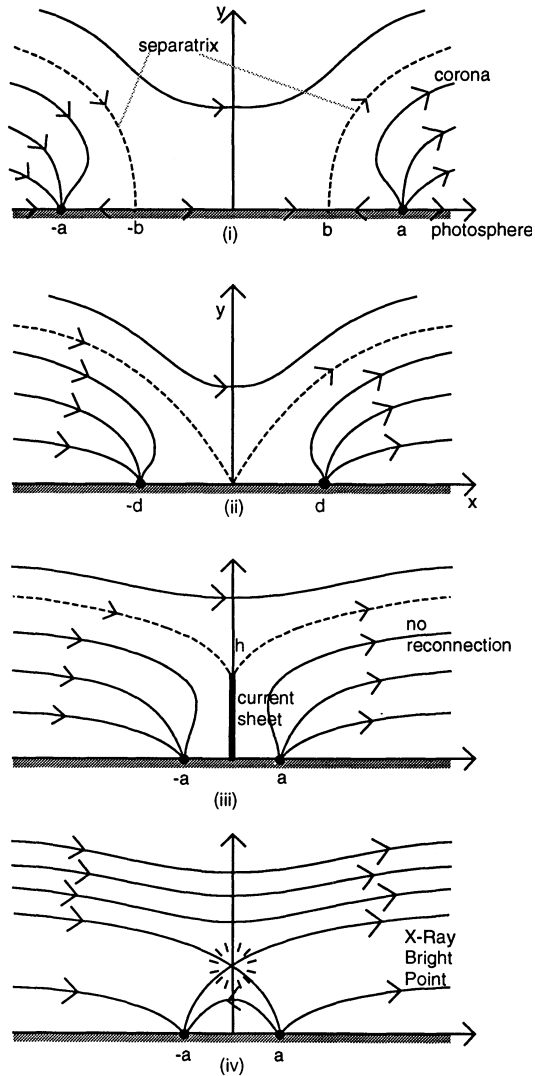


Figure 1.4: A model for pre-interaction and interaction phases of two equal poles located at $\pm a$ along the x-axis. The height of current sheet is shown by h in third panel, where topology is still preserved and no reconnection has taken place, from Priest et al., 1994

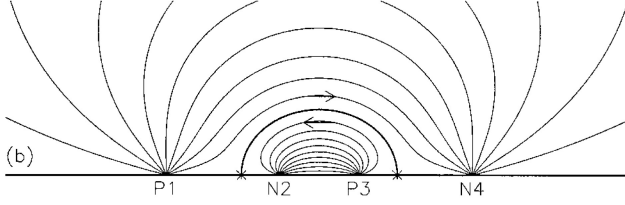


Figure 1.5: Reconnection along the separator field lines, suggested by Longcope 1998

model of the solar atmosphere at that time which were either static, fitting temporally and spatially averaged continua and line densities Vernazza et al., 1981 or dynamic but dynamic but limited to acoustic effects Carlsson & Stein 2002, they could include and investigate the rotational motions of the opposite polarities for the case which was observed and discussed in Brown et al., 2001. In a series of 3D MHD numerical simulations that was followed by (Büchner 2006, Santos & Büchner 2007, 2008) for different BP cases, they could investigated the role of the horizontal plasma motion in photosphere and chromosphere and found it essential for magnetic coupling between photosphere and corona. Using the observational photospheric magnetic field and the plasma motion in their resistive MHD model (LINMOD3D) they could obtain the electric currents at the same position as the EUV BP. In order to derive the horizontal velocity field due to plasma motion, local-correlation-tracking (LCT) method (November & Simon 1988) was applied to the line-of-sight (LOS) component of the photospheric magnetic field. The idea of the LCT method is to find the displacement that maximizes the spatially localized cross-correlation between two subsequently obtained magnetograms separated by a sampling time delay τ that is smaller than the lifetime of tracers in the scene. For this sake the spatially localized cross correlation function $C(\delta, r)$ can be defined as follows to be integrated over the full area of the images:

$$C(\delta, r) = \int_{\mathcal{S}} J_t(\epsilon - \frac{\delta}{2}) J_{t+\tau}(\epsilon + \frac{\delta}{2}) W(r - \epsilon) d\epsilon \quad (1.1)$$

It includes the intensity images $J_t(\epsilon)$ and $J_{t+\tau}(\epsilon)$ at two instances of time and a window function $W(r)$ that defines the spatial resolution of the vector displacement determination, with r representing the center of the function and δ for the two-dimensional displacement between the images. The spatially localized cross correlation function $C(\delta, r)$ is higher for the motions that lead to evolutionary changes between the images. Calculating $C(\delta, r)$ for different displacement δ , one can find the displacement that maximizes the cross correlation:

$$\frac{\partial C(\delta, r)}{\partial \delta} \Big|_{\delta=\Delta(r)} = 0 \quad (1.2)$$

By dividing the displacement $\Delta(r)$ by the time interval τ the velocity can be derived. It should be noted that the proper results of LCT requires significant contrast between the patterns. Further details can be found in Santos et al., 2006 and also, where different methods of deriving the horizontal velocities have been compared.

Another aspect that was taken into account in the numerical model of Büchner et al. 2004a,b was the inclusion of anomalous resistivity, which is essential for moving toward a more realistic modelings. This way one can couple the microphysical effect of the enhanced localized resistivity into a more global, large-scale MHD model. Before going into more details of their model which is the base of the present work, let us have a brief look at the different models of treating solar corona.

1.2 Modelings of the coronal heating

There are two main categories of theoretical models of the extra ordinary strong coronal heating trying to explain the very high temperature of the outer atmosphere by orders of magnitude than the solar surface temperature. In both classes of models energy is transported from below the surface via the photospheric motions of the magnetic fields footpoints into the corona. Classification of the relevant models are according to the way the photospheric driver and the corona are coupled or, more precisely, according to the timescales of the electromagnetical response of the corona to the photospheric driver. Magnetic tension propagates along the magnetic field lines with the Alfvén speed v_A . If the motions at the coronal footpoints of the photospheric magnetic field moves at time scales (much) faster than the Alfvén transit time along a coronal loop then the coronal loops do not have enough time to adjust, they will see an alternating current, which is the characteristic of an AC (alternating current) heating by propagating magnetohydrodynamic waves. In the opposite case, when the changes due to the photospheric driver are slow, the loop can adjust to the changing boundary condition in a quasi-static way, leading to DC (direct current) models with quasi-static currents in the corona, (Aschwanden 2001). An image of the topological dissipation of twisted magnetic flux tubes is shown in Fig. 1.6, (from Parker 1972, 1983). In Parker's model the braiding of field lines due random motions of the photospheric footpoints causes the formation of topological discontinuities through which dissipation by magnetic reconnection is expected.

The challenge for both classes of models is mainly to describe properly the energy and current dissipation, (see e.g., Aschwanden 2001, De Moortel et al., 2008). Obviously, the scales at which energy dissipation should happen are beyond the MHD scales. Kinetic effects that are significant at these scales should be taken into account in the framework of a global MHD picture. In this regard one can refer to Parker 1972, where incapability of the classical Joule dissipation of the quasi-static current in the DC model was figured out. In this case the dissipation requires the inclusion of the anomalous resistivity, i.e., a feature of the locally small scale physics, see (Birn & Priest 2007, Büchner & Elkina 2006a,b).

In DC models various ways of dissipation including, e.g., Joule dissipation of currents, magnetic reconnection, current cascading and viscous turbulence. In AC models heating can be due to e.g., Alfvénic resonances, resonance absorption, phases mixing, current layer thinning and plasma turbulence. Acoustic heating models suggest heating by compressional waves, and velocity filtration models are based on the influence of the gravitational potential field in the corona on a postulated non-Maxwellian chromospheric velocity distribution. A list of different models with variant way of current dissipation is shown in Fig. 1.8, (from Aschwanden 2001).

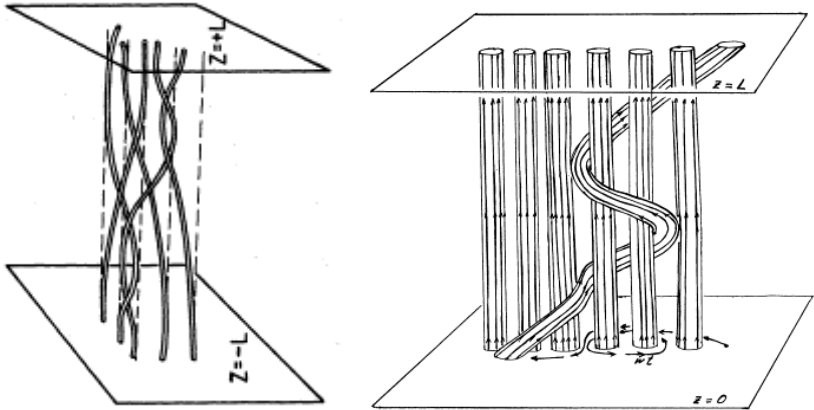


Figure 1.6: Illustration of the twisting of the magnetic flux tubes due to the random motions of the footpoints in the left panel Parker (1972) and a later stage at which the flux tubes are wound among its neighbours Parker (1983).

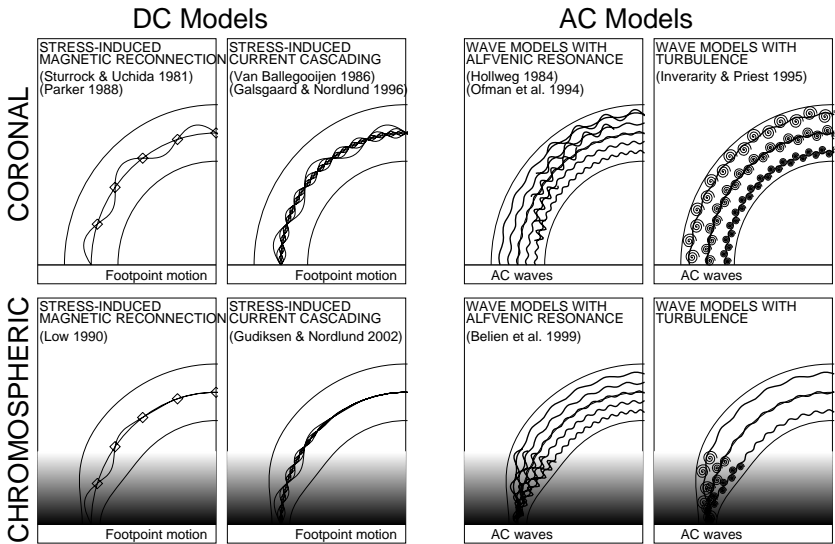


Figure 1.7: Main categories of DC and AC models (left and right panels, respectively). The top row refers to corona while the bottom row corresponds to chromosphere with darker regions at the base indicating the higher densities, (taken from Aschwanden 2002).

Progress in the theoretical and numerical models of coronal heating has been made by moving towards more realistic modelling of solar transition region and chromosphere. Considering more realistic scale heights, density and temperature profiles in the lower layers of the solar atmosphere lead to a heating which is more concentrated around the footpoints and in the vicinity of the large density and temperature gradients in the transition region, (see lower panel of Fig. 1.7 in comparison to the upper panel).

Fig. 1.9 from Schrijver et al., 2000 illustrates how our picture from different layers of the solar atmosphere has changed from the gravitationally stratified layers in 1950s (left panel), moving to 1980s with some more details from the chromosphere (middle panel) and fully inhomogeneous current picture at which considering more dynamical processes has mixed up the boundaries of these layers. The dynamic processes involved are, e.g., heated upflows, cooling downflows, intermittent heating (ϵ), nonthermal electron beams (e), field line motions and reconnections, emission from hot plasma, absorption and scattering in cool plasma, acoustic waves and shocks. Deviation from the gravitational

Parameter	Photosphere	Cool corona	Hot corona	Outer corona
Electron density n_e (cm^{-3})	2×10^{17}	1×10^9	1×10^9	1×10^7
Temperature T (K)	5×10^3	1×10^6	3×10^6	1×10^6
Pressure p (dyne cm^{-2})	1.4×10^5	0.3	0.9	0.02
Magnetic field B (G)	500	10	10	0.1
Plasma- β parameter	14	0.07	0.2	7

Table 1.1: Plasma- β in the solar atmosphere, Aschwanden (2001)

stratification and the radial density profile is a result of magnetical structuring of the solar atmosphere. A useful factor to measure the magnetic confinement of a region is plasma- β , the ratio between the thermal pressure and the magnetic pressure. At regions with high values of plasma- β , the particles are energetic enough to cross magnetic field lines. Typical values of plasma- β as well as electron density, temperature, etc., are given for four layers of the solar atmosphere from photosphere to the outer corona, in Table. 1.1, (from Aschwanden 2001). The averaged value of β versus height is illustrated in Fig. 1.10 based on a model by Gary, G. A., 1974. The Figure shows that in the inner corona ($R \lesssim 0.2R_\odot$) magnetic pressure generally dominates the plasma pressure. The small value of β the solar corona implies that this region is highly magnetically structured. This lead to the idea modelling the corona by subdividing it into separate magnetic flux tubes isolated from each other at 1980s, (middle panel on Fig. 1.9). This picture was modified after the high resolution images were available from observations showing that the by the various dynamic processes that are going on, including the chromospheric heated upflows and the downward coolings, the corona is quite dynamic. An observational evidence in this regard was given by Solanki et al., 2003, showing the coexistence of the cool and hot material in the chromosphere. Therefore for using EUV and X-ray fluxes for modelling of the corona, one should impose some statistical distribution of flux tubes along any line-of-sight. One challenging aspect for a proper modelling of the corona in connection with the transition region and chromosphere is their deviation from the Local Thermodynamic Equilibrium (LTE). Consequently, one would need to consider the full statistical equilibrium equations. Hydro-radiation simulations was carried out

Physical process	References
<i>1. DC stressing and reconnection models:</i>	
– Stress-induced reconnection	Sturrock & Uchida (1981) Parker (1983, 1988); Berger (1991, 1993) Galsgaard & Nordlund (1997)
– Stress-induced current cascade	Van Ballegoijen (1986) Hendrix et al. (1996) Galsgaard & Nordlund (1996) Gudiksen & Nordlund (2002)
– Stress-induced turbulence	Heyvaerts & Priest (1992) Einaudi et al. (1996a,b) Inverarity & Priest (1995a) Dmitruk & Gomez (1997) Milano et al. (1997, 1999); Aly & Amari (1997)
<i>2. AC wave heating models:</i>	
– Alfvénic resonance	Hollweg (1985, 1991) Ionson (1978, 1982, 1983), Mok (1987)) Davila (1987), Poedts et al. (1989) Goossens et al. (1992, 1995) Steinolfson & Davila (1993) Ofman & Davila (1994); Ofman et al. (1994, 1995) Erdélyi & Goossens (1994, 1995, 1996) Halberstadt & Goedbloed (1995a,b) Ruderman et al. (1997) Bélien et al. (1999)
– Phase mixing	Heyvaerts & Priest (1983) Parker (1991); Poedts et al. (1997) De Moortel et al. (1999, 2000a) Galsgaard & Nordlund (1996)
– Current layers	Inverarity & Priest (1995b)
– MHD turbulence	Matthaeus et al. (1999) Dmitruk et al. (2001, 2002)
– Cyclotron resonance	Hollweg (1986), Hollweg & Johnson (1988) Isenberg (1990), Cranmer et al. (1999a) Tu & Marsch (1997, 2001a,b) Marsch & Tu (1997a,b,2001)
<i>3. Acoustic heating:</i>	
– Acoustic waves	Schatzman (1949) Kuperus, Ionson, & Spicer (1981)
<i>4. Chromospheric reconnection:</i>	
	Litvinenko (1999a) Longcope & Kankelborg (1999) Furusawa & Sakai (2000) Sakai et al. (2000a,b, 2001a,b) Brown et al. (2000) Tarbell et al. (1999) Ryutova et al. (2001) Sturrock (1999)
<i>5. Velocity filtration:</i>	
	Scudder (1992a,b; 1994)

Figure 1.8: list of different models with variant way of current dissipation is shown in Fig. 1.8, Aschwanden (2001).

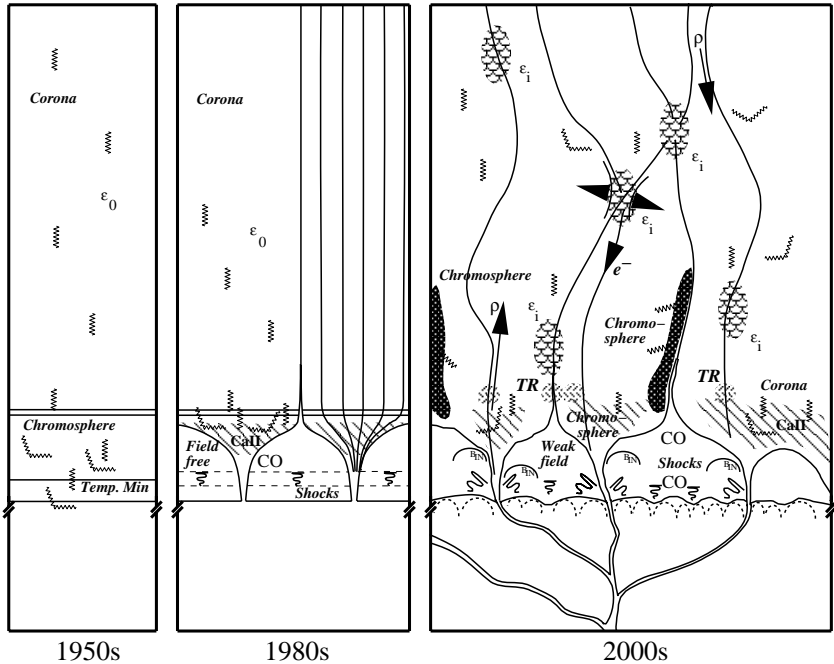


Figure 1.9: Evolution of solar corona models: Gravitationally stratified layers in the 1950s (left), vertical flux tubes from the chromosphere in the 1980s (middle) and a mixing of photospheric, chromospheric and corona zones due to different dynamical processes, (Aschwanden 2001, Schrijver et al., 2000)

for instance by Carlsson & Stein 1992 in 1D self-consistent radiation hydrodynamic model which was later extended to 3D Carlsson & Stein 2002, as is necessary for a proper description of processes like mode conversion, reflection and refraction of waves. A critical quantity for mode conversion is the angle between the magnetic field and the velocity polarization, which determines the transition of the photospheric acoustic, fast modes to acoustic, slow mode wave propagating along the magnetic field. However, the Non-LTE 3D radiative MHD simulations and a detailed coupling of the radiation field and matter in the chromosphere are too complex to be solved in general. Therefore, some problem dependent approximations are needed to bring the complexity to tractable levels, (see Carlsson & Stein 2003). The computational domain in this case should be optically thin for all frequencies at the top boundary and optically thick at the bottom boundary. The main steps to get a consistent solution in 1D are to start from LTE radiative in the hydrostatic equilibrium and move gradually from LTE to non-LTE by switching collisional radiation. Gradually, the radiation in the energy equation can be turned on and then incoming radiation fields can be considered.

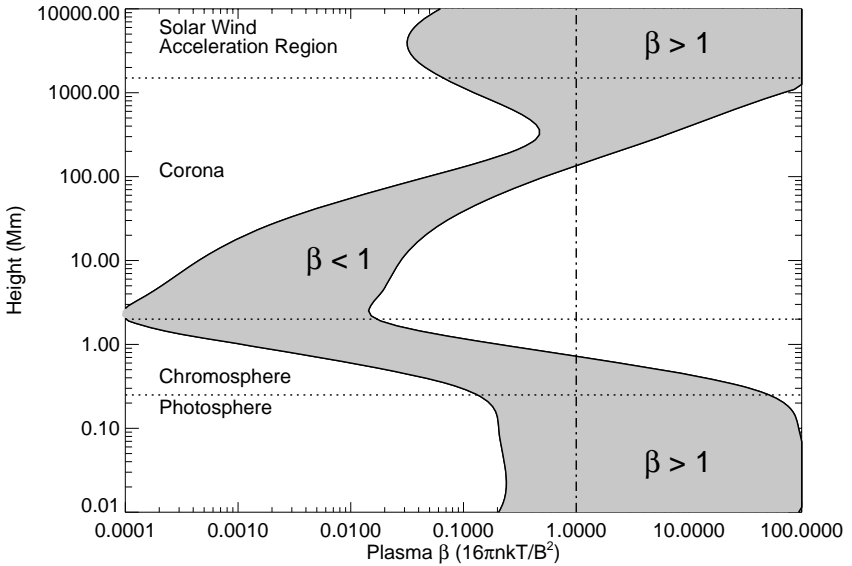


Figure 1.10: The values of plasma- β at different heights is shown based on a model by Gary, G. A., 1974 for two different magnetic field strengths of 100G and 2500G. It shows the regions with $\beta > 1$ can occur even in the coronal heights

The linking between observations and the theoretical modelling is indeed crucial for both sides. It helps to give sights for further designment of the observational instruments as well as to examine the capability of the theoretical models in reproducing observations. However, The physical parameters provided by theoretical models are often different from the quantities that are provided from observations. In using the inversion of the observed data for deducing the usual parameters of theoretical models one has to deal with the problem of non-unique solutions. The direct interpretation of the observations is also challenging because of e.g., the unknown filling factor (the ratio between volume radiating in certain emission line to the total volume). A more reliable approach is to calculate observable parameters like intensities or Doppler shifts from theoretical models and compare them directly to the observations. De Moortel et al., 2008 have reviewed the role of this so called 'forward modelling' approach on the development of the coronal heating problem. It has been stated there that strong correlation between the brightness of corona emission and the strength of the magnetic field has been indeed justified with a wide ranges of evidences. Regarding the proper modelling of solar corona, since the conduction and radiation energy losses has been estimated to of the order of 10^4 Wm^{-2} in active regions, the adequate model for this problem would need to supply this energy. There are observational evidences for both of the two main classification of the coronal heating problem, namely AC and Dc models. For the AC model, there are recent ground

and space-based observations that can detect coronal waves but the corresponding energy fluxes re far below the required values for corona, Tomczyk S et al., 2007. Neither the transverse displacements of spicules observed by Hinode/SOT (De Pontieu B et al., 2007) nor the transverse oscillations of filamentary structures in prominences (Okamoto et al., 2007) were sufficient to heat the corona. Although the wave heating can be an strong candidate for open field regions, it is probably less viable for closed regions with shorter Alfvén times (De Moortel et al., 2008). In contrary In the DC model the Poynting flux of energy:

$$F = \frac{1}{\mu} B_v B_h V_{ph} \quad (1.3)$$

with B_v and B_h the vertical and horizontal components of the magnetic field, respectively, is sufficient for heating when the typical values of coronal magnetic field $B_v = 0.01$ T and the photospheric footpoints velocity $V_{ph} = 1 \text{ km s}^{-1}$ are used, providing that $B_{horizontal}$ is least 10 percent of the $B_{vertical}$. This constraint for switching on the dissipation has to be considered in the modelling to provide the sufficient localized energy dissipation by reconnection, (see, e.g., Priest & Forbes 2000). One approach toward deducing the right parameters for a heating model that reproduce the observations is to create the coronal magnetic extrapolation based on the photospheric magnetic field (obtained from Zeeman splitting of spectral lines - since the coronal magnetic fields can not be measured directly, unless in low temporal and spatial resolution using for example Hanle effect, Faraday rotation, Stokes polarimetry in infrared, etc.,). Using different heating scales in terms of field strength and loop lengths, $\varepsilon_h B^\alpha L^\beta$, Warren & Winebarger, 2006 tested various heating models to find the α and β with which the volumetric heating result in images that matches the actual images best. Fig. 1.11 shows the images of one of the active regions that they used for this study (AR 7997 on 1996 November 26th) taken from Solar and Heliospheric Observatory (SOHO) / EUV Imaging Telescope (EIT) and SOHO / Yohkoh Soft X-ray Telescope (SXT). The result of Potential field extrapolation is used for simulations with different volumetric heating models $\alpha = 1, \beta = 0, 1, 2$. The comparison shows that the best agreement between the observations and simulations suggest a heating model that scales a $\varepsilon_h \bar{B}/L$, where \bar{B} is the magnetic field strength along a field line with the length of L, and they found this heating model consistent with the field-braiding reconnection model suggested by Parker 1983 illustrated in Fig. 1.6.

Another approach in the framework of the advanced 3D MHD simulation was made by Gudiksen & Nordlund 2006, carrying on ab initio model of coronal heating at which the heating of corona is provided through the slow braiding of the magnetic field lines by photospheric footpoint motions. The idea was followed by Peter et al., 2004, 2006 where they calculate intensity and Doppler shifts and provide diagnostics which can be compare to the both imaging and spectroscopic observations and this comparison has shown a remarkable agreement. In a further step in the PhD thesis of S. Bingert using a randomly distributed heating function they could reproduce a Nanoflare distribution result in a hot corona. In the Nanoflare heating model which was proposed by Parker 1988, many small scale heating events are assumed to produce the adequate heat for the corona. The less frequent large-scale heating events like solar flares for coronal mass injections can indeed release much more energy ones they happen, but even then with the thermal conduction restricted mainly along the magnetic field lines due to small coronal plasma- β ,

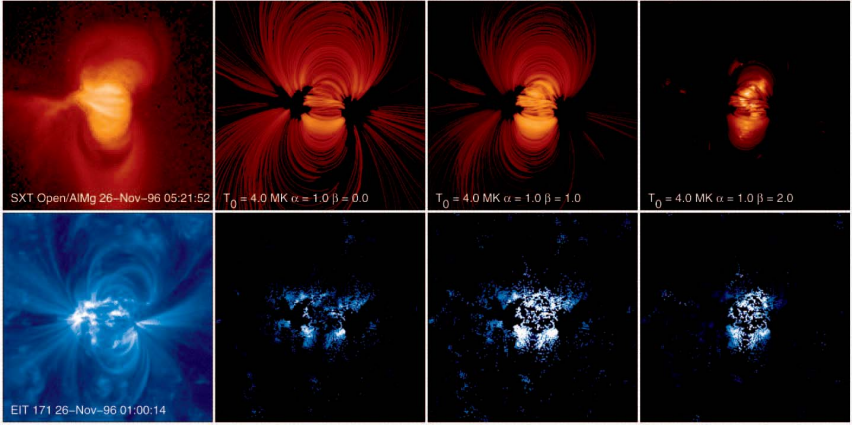


Figure 1.11: Synthetic SXT AIMg and EIT 171 A images for AR 7997 on 1996 November 26th are shown, as well as the images for the cases with $\alpha = 1, \beta = 0, 1$ and 2 . The case with $\alpha = \beta = 1$ fits the real images best, Taken from Warren & Winebarger, (2006).

they are unlikely to be sufficient to maintain coronal temperature. The sufficiency of the heat provided by small scale event would depend on the steepness of the spectrum of the frequency of their occurrence versus energy, Hudson 1991. There are some observational evidences for some small-scale events at the energy ranges of the nanoflares, which are found at the bottom of the energy and temperature scales, (see, e.g., Aschwanden 2001). These observed tiny nanoflares coincide with the relevant theoretical DC models (for example Parker 1988) if the magnetic dissipation happen in the height of the transition region. About 95 percent of photospheric magnetic fluxes are estimated to close at this height, which give a high chance for occurrence of EUV Nanoflares.

1.3 The scope of this work

We performed a 3D MHD simulation model to investigate the physical processes involved in the dynamical evolution of the solar atmosphere plasma in the region of a X-ray coronal bright point (BP), observed by Hinode/XRT telescope on 19 December 2006. The velocities of the photospheric driver are deduced by applying the Local-Correlation-Tracking(LCT) method to the photospheric line-of sight (LOS) components of the magnetic field, provided by SOHO/MDI magnetograms. The simulation box is extended from photosphere to corona, so that it includes the motions of the footpoints of magnetic field lines as well as the resulting braiding of field lines as they arrive in the coronal heights or more likely, when the close in some lower altitudes. Therefore the theoretical DC model suggested by Parker 1972 has been followed, where the complex magnetic structures that is the hosting the different geometries for current dissipation have been ruled out by magnetic field photospheric footpoint motions. These motions pump up the adequate

heating energy for heating the corona through the Poynting flux at the base. The coupling of the neutral gas and the plasma is being adjusted though a collision profile, so that it is efficient only in the regions with higher values of plasma- β , or the regions below the transition region heights. More details about the model can be found in the next Chapter. In the third Chapter, we are addressing the importance of Joule heating as heating mechanism for the corona, as is used in a similar 3D model by for example Peter et al., 2004, 2006 and PhD thesis of S. Bingert. We used resistivity values that were by many order of magnitudes higher than the classical values of Spitzer resistivity. This makes sense as far as this re-scaling compensate the lower values of currents, concerning the large scales of MHD simulation. However even these very high resistivity values were found to be adequate for increasing the temperature. The resulting Joule dissipation was even less efficient than the adiabatic compression in heating the plasma. Therefore, in using unrealistic high values of resistivity to get a hot corona that maintain the temperature one should have in mind that it an artificial way to cover the contribution of the heating mechanism that we are not considering in such a models properly.

It should be added here that the a certain switch for turning on an additionally high resistivity was used in the model to provide microphysics involve in dissipation in small scales. This way we could couple kinetic effects in a global MHD model, Although, it did not change the fact that the Joule dissipation had a minor effect to heat the plasma comparing to the adiabatic heating for example. The other issue was considering two heating mechanism in the model. In the energy equation the classical heat conduction in parallel to magnetic field lines was included, which is a reasonable assumption for a highly ionized plasma that can move freely only along the magnetic field lines. The heat conduction coefficient is taken as it is obtained by Spitzer 1962. Another loss mechanism added to the model is the radiative cooling. There are a number of atomic processes involved in coronal emission in X-ray and EUV, namely induced absorption, stimulated and spontaneous emission, photo-ionization, 2-body and 3-body recombination, auto-ionization, Thomson scattering, free-free emission (Bremsstrahlung) and absorption, collisional excitation, de-excitation and ionization. For a review of the contribution of these processes in different temperature and line emissions see for example Aschwanden 2001. It is more practical to use a radiative function that sums up all the line intensities in different temperature ranges. The radiative loss function that we used for this sake was calculated by Rosner et al., 1978. There are more recent version of this calculation, given for example by Cook et al., 1989, where the difference is mainly due to different assumptions in the elemental abundances. A comprehensive code that contains all the known line transition is CHIANTI code, (see for example, Landi et al., 2006). CHIANTI atomic database for spectroscopic diagnostics of astrophysical plasmas and can be use for calculation of more precise versions of radiative loss function. Although this would not change the dynamic evolution of the system that we study here.

In a series of 2D MHD simulations for the case of coronal BP, Von Rekowski B., Parnell C. E., Prist E. R., 2006a,b, Rekowski et al., 2008 investigated the physical consequences of different thermodynamical models, For example comparison of an isothermal model with a model that let the temperature evolve in time. The test the effect of inclusion of different combination of the following mechanism: adiabatic heating/cooling, viscous and Joule heating, radiation and thermal conduction along the magnetic field lines. Considering different boundary conditions, they emphasis that the inclusion of the

heat conduction can avoid unrealistic high values of coronal temperatures. They specify there the inclusion of an additional term to mimic the background coronal heating which is not properly understood yet. It should be noted here that have not included any unknown source of background heating in the model, aiming at investigation of the physical processes that are certainly acting in the dynamical evolution of the system, rather than creating a hot corona with heating terms which are not well justified. Hence the only heating source in this case would be the Joule dissipation of the electrical currents that are created due to the footpoint motions of the magnetic bipoles of opposite polarities correspond to this BP. The chosen BP is magnetically rather weak however, and therefore would not create a Poynting flux that is sufficient for a hot corona and to keep it at high temperatures. In the absence of any other heating source in the simulation box and while the two loss terms, radiative cooling and heat conduction- are acting, one can expect a drop in temperature profile which is the case in Chapter 4. Let us summarize our approach by listing the required steps for performing the simulation:

- Choosing a specific bright point
 - Taking magnetogram (MDI image) of this BP
 - Filtering the data using Fourier Filter with 8 modes
 - Extrapolation of the magnetic field to obtain the full components of magnetic vector
- Set of the MHD equations
 - Normalization of equations and the transport coefficients (e.g., for resistivity, heat conduction and radiative loss)
 - Setting the initial conditions and profile (e.g., for collision frequency, density, etc.)
 - Applying the boundary condition
- Inserting the result of LCT method through a number of vortices that reproduce the same motion
- Deducing the physical parameters using the result of MHD simulation

Depending on the case, one can choose to switch on or off any of the heating and loss terms, namely Joule dissipation, radiative losses and heat conduction. The same is valid for different choices of resistivity model and coefficient, consequently.

2 The MHD model

Magnetohydrodynamic (MHD) is a fluid model of plasma derived from the Vlosov-Maxwell system. The current form of the MHD equations has been derived by Lundquist 1952, while the invention of MHD is attributed to Alfven, 1947, who performed a linearized analysis of coupled hydrodynamic and non-relativistic Maxwell's equations. The following assumptions has been made in the framework of MHD: non-relativistic fluid with $v \ll c$; validity of the charge neutrality $\omega_{pe}\tau \gg 1$, (which implies that the oscillations in plasma density are slow so that the electron motion can maintain the charge neutrality); length scales greater than the ion gyroradius $L \gg v/\Omega_i$; and mean free path between the collisions smaller than the length scale of system L .

2.1 MHD equations

The set of MHD equations that are used in the MHD code are as follows:

$$\frac{\partial \rho}{\partial t} = -\nabla \cdot \rho \mathbf{u} \quad (2.1)$$

$$\begin{aligned} \frac{\partial \rho \mathbf{u}}{\partial t} &= -\nabla \cdot \rho \mathbf{u} \mathbf{u} - \nabla p + \mathbf{j} \times \mathbf{B} - \nu \rho (\mathbf{u} - \mathbf{u}_0) \\ &= -\nabla \cdot \left[\rho \mathbf{u} \mathbf{u} + \left(p + \frac{B^2}{2\mu_0} \right) \mathbf{I} - \frac{\mathbf{B} \mathbf{B}}{\mu_0} \right] - \nu \rho (\mathbf{u} - \mathbf{u}_0) \end{aligned} \quad (2.2)$$

$$\frac{\partial \mathbf{B}}{\partial t} = \nabla \times (\mathbf{u} \times \mathbf{B} - \eta \mathbf{j}) \quad (2.3)$$

$$\frac{\partial p}{\partial t} = -\nabla \cdot p \mathbf{u} - (\gamma - 1) p \nabla \cdot \mathbf{u} + (\gamma - 1) S \quad (2.4)$$

together with Ohm's and Ampère's laws:

$$\mathbf{E} = -\mathbf{u} \times \mathbf{B} + \eta \mathbf{j} \quad (2.5)$$

$$\nabla \times \mathbf{B} = \mu_0 \mathbf{j} \quad (2.6)$$

Here ρ , \mathbf{u} , \mathbf{B} are plasma density, velocity and magnetic field, respectively. Plasma temperature (T) is related to plasma pressure (p) via the ideal gas law for a fully ionized plasma:

$$p = 2n\kappa_B T$$

Neutral gas density and velocity are denoted by ρ_0 and \mathbf{u}_0 . The ions and electrons are assumed to have the same temperature, which explains the factor 2 in the equation of state. The neutral gas is coupled to plasma via the collision term in momentum equation,

$\nu\rho(\mathbf{u} - \mathbf{u}_0)$, where ν represents the collision frequency. The vertical profile of the collision frequency is chosen in a way that the plasma-neutral gas coupling has the maximum value in photosphere and vanishes in the solar coronal, as shown in Fig. 2.1. So for the height below z_{tr} , which is the location of the transition region, i.e., boundary between solar chromosphere and corona, we have:

$$\mu(z) = \mu_0 \left(1 - \frac{z}{z_{tr}}\right)$$

where μ_0 is the collision frequency at photosphere. Above the transition region it decays quickly with height:

$$\mu(z) = e^{-\frac{z}{4z_{tr}}}$$

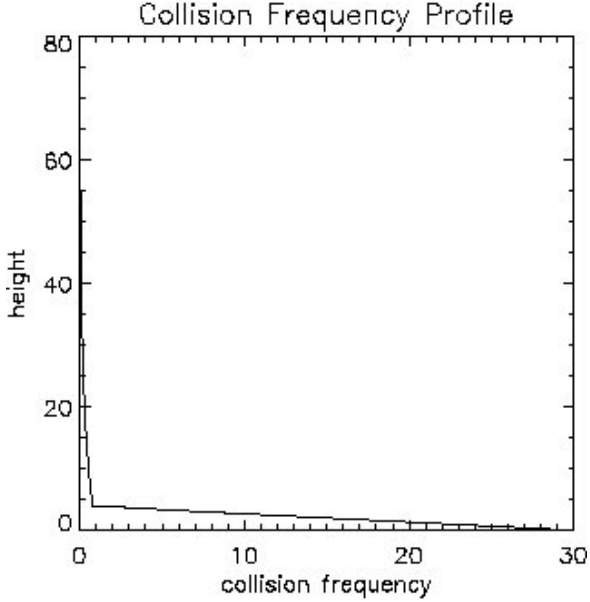


Figure 2.1: The vertical profile of collision frequency that was used as initial condition in our simulation model.

The source term, S , in the energy equation includes:

$$S = \eta j^2 - \nabla \cdot \mathbf{q} - L_r \quad (2.7)$$

where η is the resistivity coefficient, (see next subsection). Heat conduction is considered only for electrons and along the magnetic field:

$$\nabla \cdot \mathbf{q} = \nabla_{\parallel} \cdot (\kappa_{\parallel} \nabla_{\parallel} T) \quad (2.8)$$

with the classical Spitzer-value for κ_{\parallel} :

$$\kappa_{\parallel} = 1.8 \cdot 10^{-10} \frac{T^{5/2}}{\ln \Lambda} \text{ W m}^{-1} \text{ K}^{-1} \quad (2.9)$$

which gives the typical values of $\kappa_{\parallel} \approx 10^{-11} T^{5/2}$ with a Coulomb logarithm of $\ln \Lambda \approx 20$. Across the magnetic field the conduction is mainly due to ions and by some order of magnitudes lower.

The radiative loss function for the optically thin layers of solar atmosphere (chromosphere and corona) has the form:

$$L_r = n_e n_n Q(T) \quad (2.10)$$

$$\text{with } Q(T) = \chi T^{\alpha} \text{ W/m}^3 \quad (2.11)$$

where n_e is the electron density and n_n the density of protons, Priest 1982. For the case of fully ionized plasma $n_n = n_e$. Note that the given $Q(T)$ is an analytical approximation for temperature evaluation of radiative loss function, which sums up all the line contribution radiations in different temperature intervals. The coefficients χ & α have been calculated by many authors, while here they are taken from Rosner et al., 1978. There the approximation is made by a powerlaw parameterization for certain temperature intervals, as listed in table. 2.1. The Analytic fit of Rosner et al., 1978 is shown in Fig. 2.2 with solid line, which has a maximum around 10^5 K. Note that the difference in the various calculations of this function is mainly a result of different assumptions in the elemental abundances.

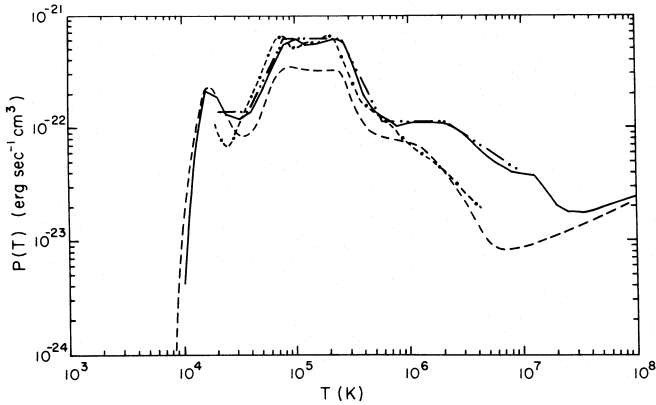


Figure 2.2: radiative loss function $Q(T)$ derived by different authors. The analytic fit of Rosner et al., (1978) is shown with the solid line. The plot is taken from Priest 1982.

2.2 Resistivity models

The magnetic resistivity (η) used in the model is composed of a constant background resistivity (η_0) and current dependent anomalous resistivity (η_{eff}). The classical Spitzer

Table 2.1: Temperature variation of χ & α , (Rosner et al., (1978))

Rang of T	α	χ
$4.4 \cdot 10^3 - 8.0 \cdot 10^3 K$	11.7	$1.26 \cdot 10^{-83}$
$8 \cdot 10^3 - 1.2 \cdot 10^4 K$	6.15	$4.93 \cdot 10^{-62}$
$10^{4.3} - 10^{4.6} K$	0	$10^{-34.85}$
$10^{4.6} - 10^{4.9} K$	2	10^{-44}
$10^{4.9} - 10^{5.4} K$	0	$10^{-34.2}$
$10^{5.4} - 10^{5.75} K$	-2	$10^{-23.4}$
$10^{5.75} - 10^{6.3} K$	0	$10^{-34.94}$
$10^{6.3} - 10^7 K$	-2/3	$10^{-30.73}$

(1962) resistivity due to binary collisions is used as a background resistivity and has density and temperature dependence:

$$\eta_0 = \frac{v_0}{\epsilon_0 \omega_{pe}^2} \quad (2.12)$$

$$(2.13)$$

where the collision frequency can be obtained from:

$$v_0 = \frac{ne^4 Ln\Lambda T^{-\frac{3}{2}}}{16\pi\epsilon_0^2 m_e^{\frac{1}{2}} K_B^{\frac{3}{2}}} \quad (2.14)$$

$$(2.15)$$

and the plasma frequency is given by:

$$\omega_{pe} = \sqrt{\frac{ne^2}{\epsilon_0 m_e}} \quad (2.16)$$

However, There is a possibility in the model for taking into account an additional resistivity term, which switches on locally when a certain criteria is satisfied. The resistivity models we have used are as follows.

In order to involve microphysical effects, (e.g., magnetic reconnection), in a MHD model, one can use an anomalous resistivity at the locations where current carrier velocity exceeds electron thermal velocity, (Roussev et al., 2002, Büchner & Elkina 2006a). This resistivity then can be added to the uniform resistivity, η_0 , in this way:

$$\eta = \eta_0 + \begin{cases} 0, & \text{if } |u_{cvi}| < u_{crit} \\ \eta_{eff} \left(\frac{|u_{cvi}|}{u_{crit}} - 1 \right) & \text{if } |u_{cvi}| \geq u_{crit} \end{cases} \quad (2.17)$$

So that when the current carrier velocity, u_{cvi} , (which is current density over charge density), exceeds a certain limit, u_{crit} , there will be an additional term for resistivity. Here η_{eff} is the normalized value of this resistivity that in terms of an effective collision rate can be written as, (Büchner & Elkina 2006a):

$$\eta_{eff} = \frac{v_{eff}}{\epsilon_0 \omega_{pe}^2} \quad (2.18)$$

where the effective collision frequency is calculated using ion plasma frequency:

$$\nu_{eff} = \frac{\omega_{pi}^2}{2\pi} \quad (2.19)$$

In the other resistivity model by Neukrich et al. 1997, a certain value of current density was directly used to switch on an additional resistivity as follows:

$$\eta = \eta_0 + \begin{cases} 0, & |j| < j_{crit} \\ \eta_0 \left(\frac{|j|}{j_{crit}} - 1 \right)^2 & |j| \geq j_{crit} \end{cases} \quad (2.20)$$

So for the current densities above j_{crit} , there will be a quadratic increase in resistivity with the excess current density. This model however, has not been successful in predicting the right locations of the finite resistivity, Büchner 2006. Therefore, we used current density dependent resistivity only to study the effect of choosing different threshold for switching on resistivity and to compare the consequent changes in the dynamics of the system. Another possibility is of course to use only the collisional Spitzer-type resistivity.

2.3 Normalization values

In order to reduce the numerical errors that normally appear when large numbers are involved in the calculation, a set of normalization values were chosen based on the typical values of these quantities in solar atmosphere.

A list of the chosen normalization values and the resulting plasma quantities are collected in table. 3.1. It can be seen from the table that magnetic field is normalized to $B_0 = 1G = 10^{-4}T$, plasma density to $n_0 = 2.10^{15}$, which is the density of protons in the corona just above the transition region, mass density to $\rho_0 = m_p n_0$, and length scale to $L_0 = 500km$. Using this values, one can obtain $v_{A0} = B_0 / \sqrt{\mu_0 m_i N_0} = 50 km/s$ for Alfvén speed and $\tau_{A0} = L_0 / v_{A0} = 10 s$ for Alfvén time. The inverse of the Alfvén time $1/\tau_{A0}$ is then used to normalize collision frequency. Magnetic pressure $P_0 = B_0^2 / 2\mu_0 = 4.10^{-3} J/m^2$ was chosen to normalize plasma pressure. Assuming same temperature for electrons and ions, we have $p = n\kappa_B(T_e + T_i) = 2n\kappa_B T$ and $T_0 = P_0 / 2n_0\kappa_B = 7.2.10^4 K$.

2.3.1 Transport coefficients

The proper normalization values for the transport coefficients that appear in the source term of the energy equation need to be derived as well. The energy equation that we used, (as it was mentioned already), has the form:

$$\frac{\partial p}{\partial t} = -\nabla \cdot p\mathbf{u} - (\gamma - 1)p\nabla \cdot \mathbf{u} + (\gamma - 1)S$$

With the source term:

$$S = \eta j^2 - \nabla_{\parallel} (\kappa_{\parallel} \nabla_{\parallel} T) - nn_e \chi T^{\alpha}$$

Using the $\hat{\cdot}$ symbol for showing normalized values, we have:

$$\frac{\partial \hat{p}}{\partial \hat{t}} = -\hat{\nabla} \cdot \hat{p}\hat{\mathbf{u}} - (\gamma - 1)\hat{p}\hat{\nabla} \cdot \hat{\mathbf{u}} + (\gamma - 1)\frac{\tau_{A0}}{p_0}S \quad (2.21)$$

Table 2.2: Normalization values.

Variable	Normalization value
magnetic field	$B_0 = 1G = 10^{-4} T$
density	$N_0 = 2.10^{15} m^{-3}$
length	$L_0 = 500 km$
.....
pressure	$P_0 = \frac{B_0^2}{2\mu_0} = 4.10^{-3} J/m^2$
temperature	$T_0 = \frac{P_0}{2 n_0 \kappa_B} = 7.2.10^4 K$
Alfven speed	$v_{A0} = \frac{B_0}{\sqrt{\mu_0 m_i N_0}} = 50 km/s$
Alfven time	$\tau_{A0} = L_0 / v_{A0} = 10 s$
thermal velocity	$v_{th0} = v_{A0} / \sqrt{2} = 35.36 km/s$
current density	$j_0 = \frac{B_0}{\mu_0 L_0}$
electric field	$\bar{E}_0 = v_{A0} B_0$
resistivity	$\eta_0 = \mu_0 L_0 v_{A0}$

So that the source term will be:

$$\hat{S} = \frac{2\mu_0 L_0}{B_0^2 v_{A0}} (\eta j^2 - \nabla_{\parallel} \cdot (\kappa_{\parallel} \nabla_{\parallel} T) - n n_n \chi T^\alpha) \quad (2.22)$$

Now the individual terms can be normalized:

$$\frac{2\mu_0 L_0}{B_0^2 v_{A0}} \eta j^2 = \frac{2\mu_0 L_0}{B_0^2 v_{A0}} \cdot \frac{\mu_0 L_0 B_0^2 v_{A0}}{(\mu_0 L_0^2)} \hat{\eta} \hat{j}^2 = 2\hat{\eta} \hat{j}^2 \quad (2.23)$$

$$\frac{2\mu_0 L_0}{B_0^2 v_{A0}} \nabla_{\parallel} \cdot (\kappa_{\parallel} \nabla_{\parallel} T) = \frac{2\mu_0 L_0}{B_0^2 v_{A0}} \frac{p_0}{2n_0 \kappa_B L_0^2} \hat{\nabla}_{\parallel} \cdot (\kappa_{\parallel} \hat{\nabla}_{\parallel} \hat{T}) = \frac{1}{2v_{A0} n_0 \kappa_B L_0} \hat{\nabla}_{\parallel} \cdot (\kappa_{\parallel} \hat{\nabla}_{\parallel} \hat{T}) \quad (2.24)$$

$$\frac{2\mu_0 L_0}{B_0^2 v_{A0}} n n_n \chi T^\alpha = \frac{2\mu_0 L_0}{B_0^2 v_{A0}} n_0^2 \hat{n} \hat{n}_n \chi (T_0 \hat{T})^\alpha = \frac{2n_0 L_0}{m_p v_{A0}^3} \hat{n} \hat{n}_n \chi (T_0 \hat{T})^\alpha \quad (2.25)$$

which implies the following normalization for the transport coefficients, (so that the en-

ergy equation stays invariant):

$$\hat{\kappa}_{\parallel} = \frac{10^{-11} T_0^{\frac{5}{2}}}{2v_{A0} n_0 \kappa_B L_0} \hat{T}^{\frac{5}{2}} = \frac{10^{-11} \cdot (7.2 \cdot 10^4)^{5/2}}{50 \cdot 10^3 \cdot 4 \cdot 10^{-3} \cdot 500 \cdot 10^3} \hat{T}^{\frac{5}{2}} = 0.01 \hat{T}^{\frac{5}{2}} \quad (2.26)$$

$$\hat{\chi} = \frac{2n_0 L_0}{m_p v_{A0}^3} T_0^\alpha \chi = \frac{2.2 \cdot 10^{15} \cdot 500 \cdot 10^3}{1.67 \cdot 10^{-27} \cdot 50^3 \cdot 10^9} T_0^\alpha \chi = 9.6 \cdot 10^{33} T_0^\alpha \chi \quad (2.27)$$

Note that the value of χ_0 depends on the range of temperature and the value of α , consequently.

2.3.2 Normalized equations

The normalized set of MHD equation using the specified normalization values are as follows:

$$\frac{\partial \rho}{\partial t} = -\nabla \cdot \rho \mathbf{u} - \mu(\rho - \rho_0) \quad (2.28)$$

$$\frac{\partial \rho \mathbf{u}}{\partial t} = -\nabla \cdot \rho \mathbf{u} \mathbf{u} - \frac{1}{2} \nabla p + \mathbf{j} \times \mathbf{B} - \mu \rho (\mathbf{u} - \mathbf{u}_0) \quad (2.29)$$

$$= -\nabla \cdot [\rho \mathbf{u} \mathbf{u} + \frac{1}{2} (p + \mathbf{B}^2) - \mathbf{B} \mathbf{B}] - \mu \rho (\mathbf{u} - \mathbf{u}_0)$$

$$\frac{\partial \mathbf{B}}{\partial t} = \nabla \times (\mathbf{u} \times \mathbf{B} - \eta \mathbf{j}) \quad (2.30)$$

$$\frac{\partial p}{\partial t} = -\nabla \cdot p \mathbf{u} - (\gamma - 1) p \nabla \cdot \mathbf{u}$$

$$+ (\gamma - 1) \{ 2\eta \mathbf{j}^2 - 0.01 \nabla_{\parallel} (\kappa_{\parallel} \nabla_{\parallel} T) - 10^{34} n n_n \chi (T_0 T)^\alpha \}$$

$$(2.31)$$

Note that below the transition region the ionization/recombination and friction frequencies are large in comparison with the typical Alfvén times. Therefore as far as these frequencies are chosen large enough below corona to keep the plasma density, velocity close to equilibrium or neutral values, the details of their choice in evolution of the solar magnetic structure is not significant.

In the energy equation one can replace pressure by the variable $h = (p/2)^{1/\gamma}$ to obtain a continuity equation for the internal energy in the absence of the source terms:

$$\frac{\partial h}{\partial t} = -\nabla \cdot h \mathbf{u} - \frac{(\gamma - 1)}{\gamma} h^{1-\gamma} \{ 2\eta \mathbf{j}^2 - 0.01 \nabla_{\parallel} (\kappa_{\parallel} \nabla_{\parallel} T) - 10^{34} n n_n \chi (T_0 T)^\alpha \} \quad (2.32)$$

2.4 Initial conditions

The initial mass density profile would need to mimics the height stratification observed in the solar atmosphere. Here we have used a profile according to the observational VAL model, Vernazza et al., 1981. The plasma density in solar photosphere was chosen to be a 100 times larger than the coronal density. The density profile in the model has been formulated as follows,

$$\rho(z) = \frac{1}{2}\rho_{ph}\left(\frac{\tanh(z + z_{tr} - 1) - \tanh(z + z_{tr} + 1)}{\tanh(z_{tr} - 1)}\right) + \rho_c \quad (2.33)$$

where ρ_{ph} and ρ_c are photospheric and coronal density, (and $\rho_{ph} = 100\rho_c$). The height of the transition region is given by z_{tr} . The initial density profile is shown in Fig. 2.3.

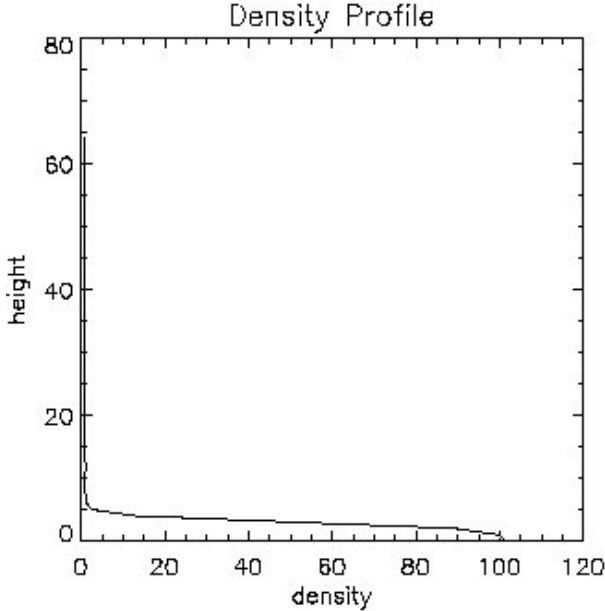


Figure 2.3: The vertical profile of density that was used as initial condition in our simulation model.

The plasma is assumed to be initially in a hydrostatic equilibrium, which gives an initially constant pressure. This constant value for the initial pressure here is $P_0 = 1$, which was chosen to be equal to the plasma beta in the model. From the definition for plasma beta we have,

$$\beta = \frac{\text{plasma pressure}}{\text{magnetic pressure}} \rightarrow \frac{\mu_0 n_0 k T}{B_0^2} \quad (2.34)$$

that is the initial magnetic pressure for the model as well. Using the equation of state, the initial temperature profile can then be obtained from the density profile, which is shown in Fig. 2.4. Gravity was not included in the model. Therefore the rate at which mass density drops at later times is much slower than in reality. The profile of the collision frequency below and above the height of the transition region was already shown in Fig. 2.1. This frequency couples plasma and neutral gas below the transition region. The neutral velocity is chosen to satisfy $\nabla \cdot \mathbf{u}_n = 0$. For the plasma coupled to neutral gas this

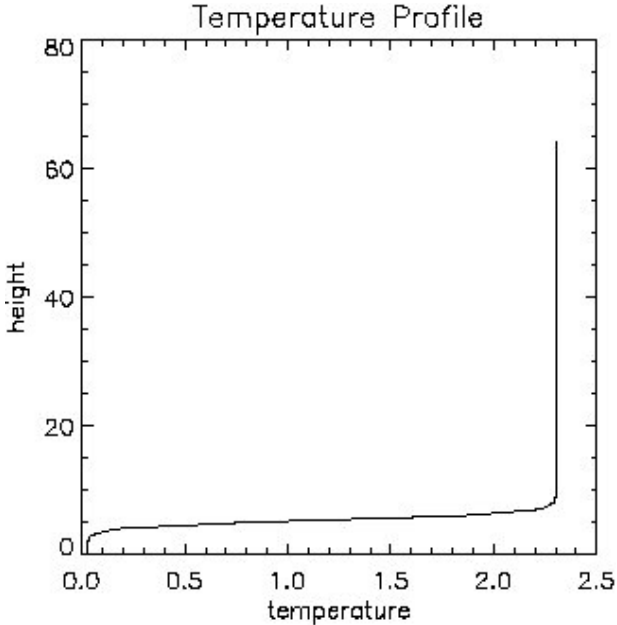


Figure 2.4: The vertical profile of initial temperature in our simulation model.

implies $d\rho/dt = 0$ which avoids unrealistic density perturbations. The neutral velocity \mathbf{u}_n is dependent in x and y , and is constant along z . It is derived from a potential using $\mathbf{u}_n = \nabla \times (U\mathbf{e}_z)$ with

$$U = u_0 / \cosh\left(\frac{x-y+c_0}{L_0}\right) / \cosh\left(\frac{x+y+c_1}{L_1}\right) \quad (2.35)$$

Magnitudes of the velocity scale with u_0/L_0 and u_1/L_1 . In the model up to 3 vortices are used to mimic approximately the observed motion of different polarity regions. The neutral motion is effective only below the transition region, where neutral density and collision frequency are large.

For the initial magnetic field the potential field extrapolation is applied to the Fourier decomposed normal field component of the magnetic field taken from the MDI-observation. The 3D magnetic configuration can be obtained by extrapolation that is needed as the initial condition of the simulation code. The normal field component is related to (B_x, B_y) through $\nabla \cdot \mathbf{B} = 0$ and $\nabla \times \mathbf{B} = 0$, and the required full symmetry boundary condition for MHD simulation is satisfied.

2.5 Boundary conditions

The simulation box has 6 boundaries: 4 lateral, 1 top and 1 bottom boundaries. In the $(x-y)$ plane the system boundaries are at $x = [0, L_x]$ and $y = [-L_y/2, L_y/2]$. At the lower boundary the normal velocity is set to be zero, while the tangential velocity is taken from the neutral motion. The normal magnetic field fulfilled the $\nabla \cdot \mathbf{B} = 0$ and the horizontal components, B_x and B_y are computed from B_z via $\nabla \times \mathbf{B} = 0$. For the upper boundary the normal derivatives are set to zero, (symmetric condition). For a plane with constant z symmetric boundary condition is used at $x = 0$. For MHD simulation the transformation

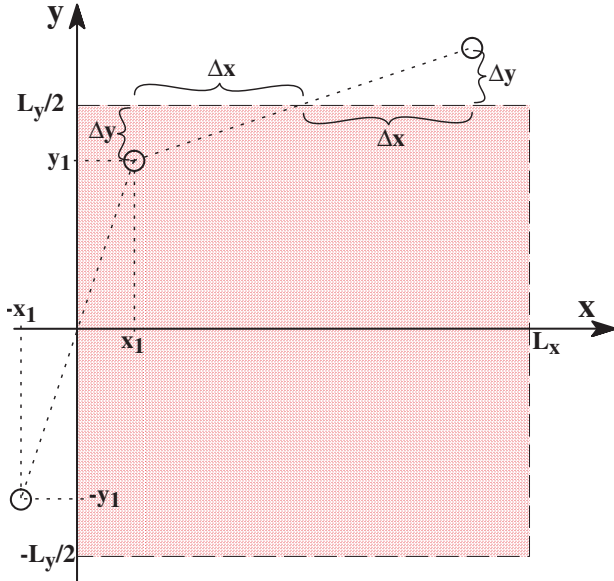


Figure 2.5: Illustration of the geometry of line symmetry, (Otto et al., 2007)

of the MHD variables need to be in a way that the MHD equations can remain invariant. There are two ways of transforming each variable, symmetric $f(-x, y, z) = f(x, y, z)$ or antisymmetric $g(-x, y, z) = -g(x, y, z)$. Positive define variables must transform symmetric, e.g., density, pressure and resistivity. Our chosen boundary condition has the following characteristics:

$$\begin{aligned} x &\rightarrow -x, y \rightarrow -y, z \rightarrow -z \\ \partial_x &\rightarrow \partial_{-x}, \partial_y \rightarrow \partial_{-y}, \partial_z \rightarrow \partial_{-z} \end{aligned}$$

Which implies a line symmetry along $x = L_x/2$ and $y = 0$, Fig. 2.5. A proper set of transformations that maintain the invariance of the equations can be as follows:

- Symmetric transformation for:

$$\rho, p, \eta, u_z, B_z, j_z$$

- Antisymmetric transformation for:

$$u_x, u_y, B_x, B_y, j_x, j_y$$

A comprehensive description of the proper boundary condition can be found in Otto et al., 2007.

2.6 Simulation properties

The set of MHD equations are solved using the second order Leapfrog scheme, which has very low numerical dissipation. A small dissipation is switched on if oscillations develop on the grid scale. Second order derivatives are treated using the Dufort-Frankel method which allows very small resistivity. A divergence cleaning procedure is applied to the

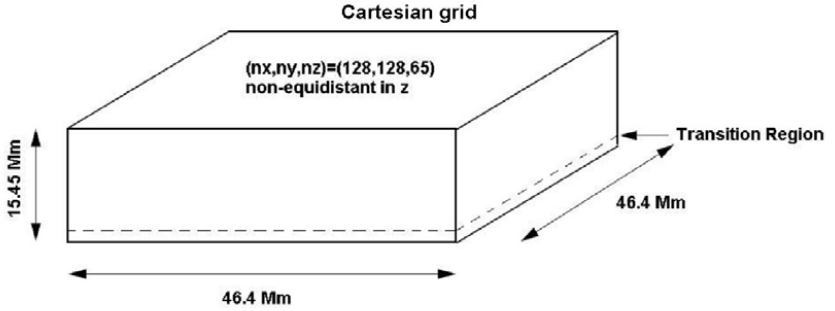


Figure 2.6: Our simulation box.

magnetic field. In this way the $\nabla \cdot \mathbf{B} = 0$ condition is satisfied for the initial magnetic field, which avoids the appearance of the related non-physical forces. The simulation box is shown in Fig. 2.6. In (x-y) plane it covers the horizontal square area of $46.4 \times 46.4 \text{ Mm}^2$. In vertical direction it extends to 15.45 Mm, towards the corona. The grids are equidistant in x and y, but non-equidistant in the z direction. In this way the nonuniform grid in z direction was chosen to have the highest resolution at the height of transition region, which corresponds to $\Delta z = 160 \text{ km}$, Fig. 2.7.

2.7 Diagnostic methods

Most of the physical parameters can be diagnosed at any cut through the 3D simulation box. These parameters are including plasma density, pressure and temperature, current densities parallel and perpendicular to the magnetic field lines, 3 components of electric and magnetic fields, resistivity, etc. They can also be integrated in z direction (vertically)

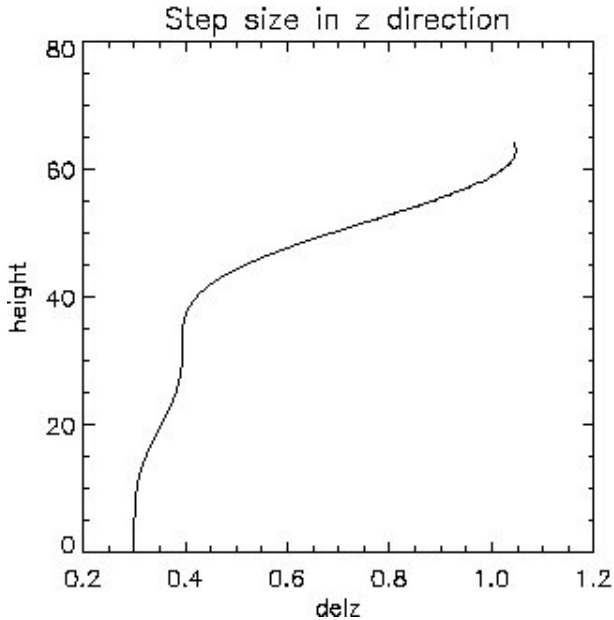


Figure 2.7: The height profile of the step size dz is shown with the lowest values at the base of the box.

in the box. Temporal of the theses parameters can be investigated as well. This way for example one can follow how energies are developing over time.

Another way to have better understanding of the dynamic evolution of the system is to trace the physical parameters along the magnetic field lines. For this sake, starting from a chosen horizontal plane, one can perform volume integral of the quantities along the magnetic field lines. The cross-section of theses differential flux tubes volumes are changing proportional to the inverse magnetic fields, $V = \int B^{-1} ds$, where ds indicates the step size along the field line). This way the flux conservation in a flux tube is guaranteed with the large values of correspond to field line rising high into the corona or hitting regions of vanishing magnetic field.

3 About the relative importance of compressional heating and current dissipation for the formation of coronal X-ray Bright Points

The mechanisms of coronal heating are not well understood. A particular object for studying heating processes are coronal bright points (further abbreviated BPs). Due to the increasing accuracy of observations our knowledge about BP has greatly advanced from the time of their discovery in soft X-ray images (Vaiana et al., 1970). According to X-ray and EUV observations the linear size of BPs is on average about 30-40 arcsec with, typically, an embedded bright core of about 5-10 arcsec (Madjarska et al., 2003). The average lifetime of X-ray BPs is about 8 hours (Golub et al., 1974) and 20 hours for EUV BPs (Zhang et al., 2001).

For a long time it has been known that BPs are associated with small bipolar magnetic features in the photosphere (e.g., Krieger et al., 1971, Brown et al., 2001). About one third of BPs lie over emerging regions of magnetic flux, while the rest of them lie above moving magnetic features. This was a base for the "cancelling magnetic feature" (CMF) model Priest et al., (1994). Lifetime and energy release of BPs are known to be closely related to the different phases of the motion of this photospheric magnetic feature (Brown et al., 2001).

First theories were mainly addressing the topology of the magnetic field below BPs (e.g., Parnell et al., 1994, Longcope 1998). Using higher resolution and cadence observations of BP's intensity and taking into account a more comprehensive patterns of motion in particular in regions with highly divergent magnetic field, (Brown et al., 2001) could associate different patterns of motion of the solar photospheric magnetic features to different stages of a BP evolution.

The plasma motion in the regions of strong magnetic field was first included by Büchner (2004a,b) in their three-dimensional numerical resistive MHD model using their 3D numerical simulation model, LINMOD3D. The latter considers dissipation of currents generated by plasma motion in photosphere on time scales longer than an Alfvén time as a one of the heating processes in the solar corona Parker (1972). In their model they took into account current dissipation due to anomalous resistivity (Büchner & Elkina 2006a,b) that causes Joule heating. Since LINMOD3D considers the compressibility of the plasma, the resulting heating could be due also to compressional effects. Later on two-dimensional MHD simulation studies were carried out by (von Rekowski B., Parnell

C. E., Prist E. R., 2006a,b, Rekowski et al., 2008). These authors used an analytical initial equilibrium and imposed a magnetic flux footpoint motion to model coronal bright point heating as being due to cancelling magnetic features. To obtain the desired heating rate they used an enhanced resistivity for which the values were above the theoretically justifiable resistivity. This raises the general question of the energy budget and energy conversion in solar flux tubes. Even with low resistivity, current simulations are unable to resolve the diffusion regions for reconnection and thus overestimate Joule heating. It is also unresolved how much heating is caused by pressure gradient forces.

To clarify this question we continued the work of Büchner et al. (2004a,b,c), Büchner (2006, 2007), Santos & Büchner (2007, 2008). These authors demonstrated the formation of localized current sheets in and above the transition region at the position of a EUV BPs as a result of photospheric plasma motion. This study is extending their results through a systematic study of the energy conversion and budget in magnetic flux tubes. The investigation uses the 3D simulation model LINMOD3d to simulate the solar atmosphere in the region of an X-ray BP observed by the Hinode spacecraft on 19 December 2006 between 22.17 UT and 22.22 UT.

In section 3.1 we briefly review the main features of the numerical simulation model LINMOD3d. In section 3.2 we describe the specific simulation setup used in our study and section 3.3 provides some simulation results for the chosen BP data. In section 3.4 we present results of energy budget analysis by investigating the role of different forces and in section 3.5 we summarize and discuss our results.

3.1 Simulation model

Our simulation model uses the approach of the LINMOD3d code (Büchner et al. 2004a,b,c). This means that the initial magnetic field is obtained by extrapolating the observed photospheric line-of sight (LOS) magnetic fields. The initial plasma distribution is non-uniform containing a dense and cool chromosphere as well as the transition to a rarefied and hot corona. The photospheric driving is switched on by coupling the chromospheric plasma with a moving background neutral gas. Some details of our code have been given briefly in the following subsection.

3.1.1 Equations

In our study we solve the following set of MHD equations:

$$\frac{\partial \rho}{\partial t} = -\vec{\nabla} \cdot \rho \vec{u} \quad (3.1)$$

$$\frac{\partial \rho \vec{u}}{\partial t} = -\vec{\nabla} \cdot \rho \vec{u} \vec{u} - \vec{\nabla} P + \vec{j} \times \vec{B} - \nu \rho (\vec{u} - \vec{u}_0) \quad (3.2)$$

$$\frac{\partial \vec{B}}{\partial t} = \vec{\nabla} \times (\vec{u} \times \vec{B} - \eta \vec{j}) \quad (3.3)$$

$$\frac{\partial P}{\partial t} = -\vec{\nabla} \cdot P \vec{u} - (\gamma - 1) \rho \vec{\nabla} \cdot \vec{u} + (\gamma - 1) \eta j^2 \quad (3.4)$$

where ρ and \vec{u} are plasma density and velocity, \vec{B} is the magnetic field and P is the

thermal pressure. A plasma-neutral gas coupling in photosphere and chromosphere is included through the collision term in the momentum equation, where \vec{u}_0 denotes the neutral gas velocity. The neutral gas serves as a frictional background to communication photospheric footpoint motion to the plasma and magnetic field through frictional interaction. It also leads to a reflection of coronal Alfvén waves back to the corona from the transition region, so that the influence of coronal Alfvén waves can be neglected at the photospheric boundary. In order to set the plasma in motion a number of incompressible flow eddies is used according to observed horizontal drifts in the photosphere $\nabla \cdot \mathbf{u}_0 = 0$ is imposed via the neutral gas, where \mathbf{u}_0 is dependent in x and y . It is constant along z and derived from a potential using $\mathbf{u}_0 = \nabla \times (U \mathbf{e}_z)$, with

$$U = u_{00} / \cosh\left(\frac{x - y + c_0}{L_0}\right) / \cosh\left(\frac{x + y + c_1}{L_1}\right) \quad (3.5)$$

Note that the contour lines of this function are streamlines of the flow. The magnitudes of velocity scale with u_{00}/L_0 and u_{00}/L_1 , chosen in accordance with the observed plasma motion in the photosphere. In our simulation we approximated the observed motion by three vortices with amplitudes of the velocity u_{00} equal to 5.5, 5 and 2 km/s, respectively. The values of c_0 , L_0 , c_1 and L_1 are 9, 6, 51 and 6 Mm for the first vortex 5, 6, 28 and 6 Mm for the second and 19, 7, 38 and 7 Mm for the third vortex. The height-dependent collision frequency ν is chosen to be sufficiently large only below the transition region. This way the plasma is forced to move, dragged by the neutral gas, in the model chromosphere but not above the transition region. This way the horizontal motion generates a Poynting flux into the corona. On the other hand the collision frequency is chosen in a way that coronal Alfvén waves are properly reflected while wave perturbations in the chromosphere are heavily damped by the frictional interaction with the neutral background. Our choice of equations means that in this study we do not consider energy losses due to radiation and heat conduction and we also excluded the action of the solar gravitation in this study. The system of equations is closed by Ohm's and Ampère's laws and the temperature is defined via the ideal gas law for a fully ionized plasma:

$$\vec{E} = -\vec{u} \times \vec{B} + \eta \vec{j} \quad (3.6)$$

$$\nabla \times \vec{B} = \mu_0 \vec{j} \quad (3.7)$$

$$p = 2n\kappa_B T \quad (3.8)$$

The value of the resistivity η is varied in accordance with three models described in subsection 3.1.3. The MHD equations are discretized by means of a second order weakly dissipative Leapfrog scheme. Due to stability reasons the induction equation is discretized using Dufort-Frankel scheme, Potter (1973).

3.1.2 Simulation box and normalization

The lower boundary of the simulation box is a horizontal square in the photosphere sized $46.4 \times 46.4 \text{ Mm}^2$. The simulation box extends 15.45 Mm toward the corona. A nonuniform grid in the z direction supplies the proper resolution of the transition layer, where the grid distance Δz corresponds to 160 km, Büchner et al. (2004a). This corresponds to 64 grid

points in z direction, while in the x, y plane a 128×128 grid are used. We solve for dimensionless variables that are normalized to natural scales as listed in table. 3.1. Note that the maximum imposed velocity of the neutral gas is smaller than 5 km/s while the typical (normalizing) electron thermal velocity is $v_{the} = 1470$ km/s and the Alfvén speed is $v_A = 50$ km/s. Hence, one can be certain that the inserted neutral gas motion is gentle, sub-Alfvénic and sub-slow velocities.

3.1.3 Resistivity models

In order to verify the influence of different resistivity models on the BP plasma heating we solved the equations for the same initial and boundary conditions but varying the resistivity model. The resistivity η can be expressed via an effective collision frequency μ as $\eta = \frac{\mu}{\epsilon_0 \omega_{pe}^2}$, where ω_{pe} is the electron plasma frequency ($\omega_{pe} = \sqrt{ne^2/\epsilon_0 m_e}$). In our model we always apply a constant physically justified background resistivity η_0 which exceeds exceeds the numerical resistivity. It is appropriate to chose for effective collision frequency of the background resistivity the Spitzer (1962) value $\mu = (ne^4 Ln\Lambda T^{-\frac{3}{2}}/16\pi\epsilon_0^2 m_e^{\frac{1}{2}} K_B^{\frac{3}{2}})$. Based on the typical plasma parameters of our model we chose for the collision-driven background resistivity $\eta_0 = 10^{-4}$ (in normalized units). In two models we switched on additional, anomalous, resistivity in places where either the current density of the current carrier velocity (u_{ccv} determined as the current density divided by the charge density) exceeds a physically justified thresholds of micro-instabilities.

In the first resistivity model anomalous resistivity is switched on when the current carrier velocity (u_{ccv} exceeds a critical velocity (Roussev et al., 2002, Büchner & Elkina 2006a,b)

$$\eta = \eta_0 + \begin{cases} 0, & \text{if } |u_{ccv}| < u_{crit} \\ \eta_{eff} \left(\frac{|u_{ccv}|}{u_{crit}} - 1 \right), & \text{if } |u_{ccv}| \geq u_{crit} \end{cases} \quad (3.9)$$

A natural choice for the threshold velocity is the electron thermal velocity v_{the} , in our for the normalizing quantities 1470 km/s or to $5.8 \cdot 10^{-4}$ in normalized units. In the first resistivity model we chose $5 \cdot 10^{-2}$ to follow the ideal evolution of the plasma as long as possible. The additional term for resistivity can be estimated e.g., for a nonlinear ion-acoustic instability (Büchner & Elkina 2006a) as

$$\eta_{eff} = \frac{\mu_{eff}}{\epsilon_0 \omega_{pe}^2} = \frac{\omega_{pi}}{\epsilon_0 \omega_{pe}^2} \quad (3.10)$$

Here ω_{pi} denotes plasma ion frequency ($\omega_{pi} = \sqrt{ne^2/\epsilon_0 m_i}$). For the typical parameters of our simulation this estimate would reveal $\eta = 2.5$, i.e. a magnetic Reynolds number of less than unity. In this case many current sheets would immediately diffuse away. On the the other hand, since the plasma β is relatively large for our simulation parameters obliquely propagating waves would be present in the spectrum of the micro-turbulence. In this case the estimate of the effective collision frequency has to take into account lower-hybrid waves (Silin & Büchner 2005). For our normalizing values this results in $\eta_{eff} = 0.03$.

In a second model calculation we considered a current density dependent resistivity used before, e.g., by Neukrich et al. (1997), in which the resistivity increases even stronger (quadratic dependence) after the current density exceeds a critical value j_{crit} :

Table 3.1: Normalization values.

Variable	Normalization value
density	$N_0 = 2.10^{15} m^{-3}$
length	$L_0 = 500 \text{ km}$
magnetic field	$B_0 = 1G = 10^{-4} \text{ T}$
.....
pressure	$P_0 = \frac{B_0^2}{2\mu_0} = 4 \times 10^{-3} \text{ J/m}^2$
temperature	$T_0 = \frac{P_0}{2 n_0 \kappa_B} = 7.2 \times 10^4 \text{ K}$
Alfvén velocity	$v_{A0} = \frac{B_0}{\sqrt{\mu_0 m_i N_0}} = 50 \text{ km/s}$
time	$\tau_0 = L_0 / v_{A0} = 10 \text{ s}$

$$\eta = \eta_0 + \begin{cases} 0, & if |j| < j_{crit} \\ \eta_{eff} \left(\frac{|j|}{j_{crit}} - 1 \right)^2 & if |j| \geq j_{crit} \end{cases} \quad (3.11)$$

The critical current density is related to critical velocity via $j_{crit} = e n_e u_{crit}$. Here we will report the results of our simulations obtained according to the second model for which we chose a threshold as low as $j_{crit} = 0.69$ in order to discuss the consequences of an early switch on of additional, anomalous resistivity. For comparison we solved the problem also by assuming for a third model a constant enhanced uniform resistivity as usually done in global MHD simulations.

Concerning the values of the chosen η_{eff} one should note that the width of the actual current sheets in which turbulence effectively operates is of the order of the ion inertial scale $d_i = \frac{c}{\omega_{pi}}$. This scale cannot be resolved in any realistic 3D MHD simulation of the solar corona. In order to introduce micro-turbulent anomalous resistivity the threshold velocity (- current density) has to up-scaled to the actual resolution of the simulation by a factor of $5 \cdot 10^4$. By the same reason the resistive electric field builds up in very (perhaps d_i -) thin current sheets. To consider the correct values of the electric field on the much coarser MHD-simulation grid anomalous resistivity used in the simulation has also to be scaled up by the above scaling factor. This approach allows to consider the correct amount of Joule heating.

3.1.4 Initial and boundary conditions

We first carried out a potential field extrapolation to the Fourier decomposed normal field component of the magnetic field taken from the MDI-observation. The resulting 3D mag-

netic configuration is used as the initial condition of the simulation code. In the potential field approximation the normal field component is related to (B_x, B_y) through $\nabla \cdot B = 0$ and $\nabla \times B = 0$. The initial density and temperature height profiles for the plasma is taken in accordance with the VAL model that assumes pressure being in a hydrostatic equilibrium. The simulation box has 6 boundaries: 4 lateral, 1 top and 1 bottom boundaries. For the side boundaries a line symmetric boundary condition is used with the line symmetry with respect to the centers of the sides of the simulation box. For the upper boundary the derivatives in the normal direction are put to zero. At the lower boundary the normal velocity is set to be zero, while the tangential velocity is taken from the neutral motion.

3.2 Simulation setup

Our study is based on an X-ray BP observed by the XRT X-ray telescope on board of the Hinode spacecraft on 19 December 2006. The corresponding X-ray image is shown in Fig. 3.1. For the initial magnetic field we used the observed *line-of-sight* (LOS) component of the photospheric magnetic field taken by the Michelson Doppler Interferometer MDI onboard the Soho spacecraft at 22:17 UT. For that sake data from a field of view with the horizontal size of $64 \times 64 \text{ arcsec}^2$ was chosen that properly covers the magnetic features associated to this BP (insert in Fig. 3.1). Note that we use the LOS component as the initial normal field component at the lower boundary of our simulation box, the photosphere, since the BP observation was made close to the center of the solar disc.

Fourier filtering was applied to the LOS component of the magnetic field. By taking into account only the first eight Fourier modes, details of magnetic field structure smaller than 6 Mm are neglected. The extension of structures arising from smaller scale magnetic features would not extend higher up into the corona, they are dissipated at an early stage of the evolution in the highly collisional chromospheric plasma.

Fig. 3.2 shows a three-dimensional view of the magnetic field extrapolated from the photospheric boundary for the magnetic field observed at 22:17 UT on December 19, 2006. The blue lines show the magnetic field lines. The color code depicts the LOS component of the photospheric magnetic field. Magnetic fields directed upward from the photosphere are colored in red, downward directed in blue.

With the chosen normalization length of $L_0 = 500 \text{ km}$, the box size in x and y direction correspond to $92.8 L_0$ and the z direction extend to $30.9 L_0$. The photospheric plasma velocities are obtained by applying the local-correlation-tracking (LCT) method Novem-ber & Simon (1988) to the Fourier filtered LOS magnetic component of the photospheric magnetic field observed between 22:17 UT and 22:22 UT. The left panel of Fig. 3.3 shows the velocity pattern obtained by the LCT method. For the simulation we used incompressible velocity vortices to mimic the observed velocity pattern, as shown in the right panel of Fig. 3.3. Note that the interval chosen for the simulation starts a few hours after the time the BP first appeared in the X-ray images and that the bright point continues to glow a few more hours afterwards. During the whole simulation time interval the relative shear motion of the two main magnetic flux concentrations of opposite polarity is negligible.

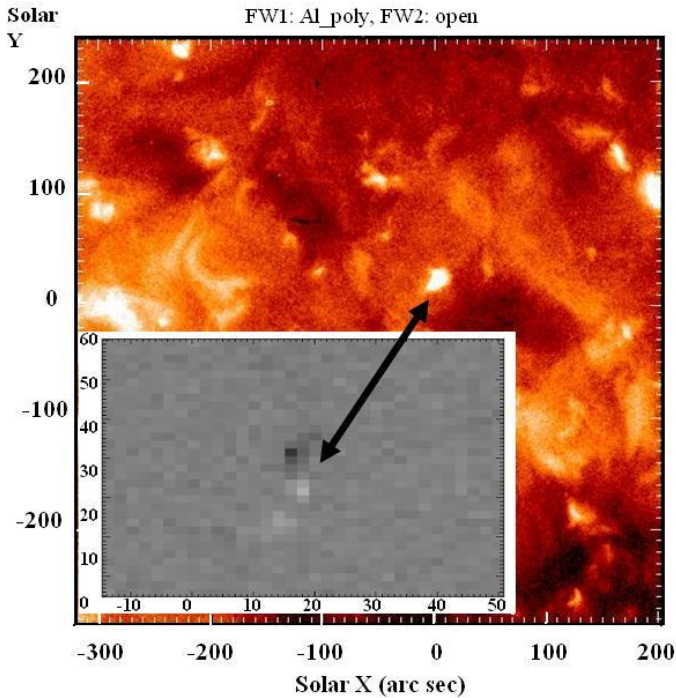


Figure 3.1: X-ray Image taken from XRT/Hinode on 19 December 2006 at 22:08 UT. Insert: the LOS component of the photospheric magnetic field in a $64 \times 64 \text{ arcsec}^2$ horizontal plane taken from MDI/Soho, where white (black) spots correspond to upward (downward) directed Line-of-sight components of the photospheric magnetic field. The BP and the related magnetic field feature are indicated in the images.

3.3 Simulation results

The simulation results are first shown in a plane at $x = 45.7$ (Fig. 3.2), which crossed through the center of the two main magnetic polarities. The vertical profile of the temperature is shown in Fig. 3.4 for $t = 0$ (top panel), 80 (middle panel) and 160 s (bottom panel). In $t = 0$ we have a height dependent temperature as defined by the initial condition. At $t = 80$ s the effects of plasma compression and expansion, together with Joule heating, shape the temperature profile. An arc of hot plasma is formed above the two opposite magnetic polarities. The increase in temperature in this layer is approximately 0.5 in normalized units, what corresponds to 36000 K. The region that is located just below it, however, experiences some drop in temperature. At $t = 160$ s the arc of hot plasma leaves the simulation box and we are left with a corona in which the differences in temperature can reach one orders of magnitudes.

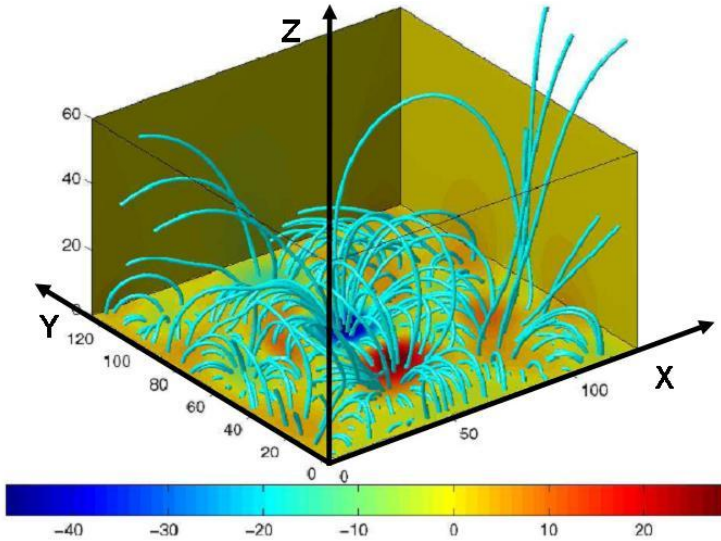


Figure 3.2: Potential magnetic field extrapolated from the filtered MDI magnetograms and used as initial configuration for the magnetic field in our simulation. The blue lines show the magnetic field lines. The color code depicts the LOS component of the magnetic field. Note that axes here are in terms of grid points, 64 in z direction and 128×128 in x,y plane. This corresponds to 15.45 Mm at z direction and 46.4 Mm at x and y directions.

Fig. 3.5 shows the parallel and perpendicular components of the current with respect to the magnetic field direction at $t = 80$ and $t = 160$ s. It can be seen that enhanced current flows coincide well with the temperature increase. This would lead to an interpretation of the heating as being due to current dissipation only. However, as shown later, adiabatic heating can have an important contribution to temperature increase.

3.4 Energy balance

Let us now diagnose the different contributions to plasma heating in the BP region. First, in subsection 3.4.1, we discuss the overall global heating. In subsection 3.4.2 the dependence on the resistivity model is presented. Finally, the flux-tube heating is analyzed in subsection 3.4.3.

3.4.1 Global effect of current dissipation and compression

In order to understand the relative contribution of current dissipation and plasma compression to the coronal plasma heating in the BP region it is appropriate to analyze the

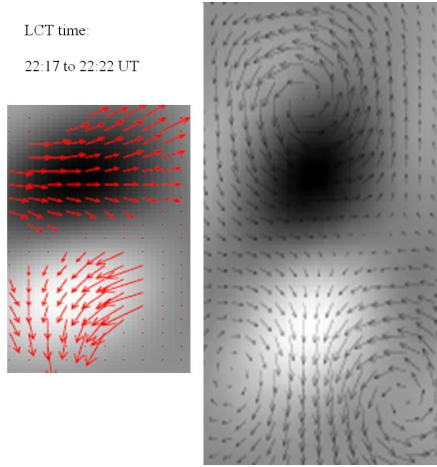


Figure 3.3: Horizontal plasma velocities in the photosphere. Left panel: velocities obtained by applying LCT technique to MDI magnetograms between 22:17 and 22:22 UT. The right panel shows the vortices that are used to approximate this motion in the simulation. The panels are showing the region that covers the two main magnetic flux concentrations with approximately 3.6 Mm width and 10.87 Mm height.

pressure changes rewriting the Eq. 3.4 in terms of a continuity equation for the Temperature evolution. This leaves two source terms on the right hand side of the equation:

$$\frac{\partial T}{\partial t} + \vec{\nabla} \cdot T\vec{u} = -(\gamma - 1) T \vec{\nabla} \cdot \vec{u} + (\gamma - 1) \eta j^2 / \rho \quad (3.12)$$

Let us first analyze the first case, where an anomalous resistivity is used when the current carrier velocity exceeds a critical value. Fig. 3.6 shows the resulting distribution of $-(\gamma - 1) T \vec{\nabla} \cdot \vec{u}$ in the vertical diagnostic plane. This way we have a proxy for temperature changes associated to pressure compression and expansion.

Adiabatic heating has an important role on the formation of the high temperature arc that propagates upward towards the top boundary. It is also due to expansion that temperature decreases below this hot arc.

The values of second term in the right hand side of the Eq. 3.12, $(\gamma - 1) \eta j^2 / \rho$, is shown in Fig. 3.7 in the plane $x = 45.7$ at $t = 80$ s and $t = 160$ s. By comparison with the compressional part the contribution of the Joule heating appears to be negligible. For a better comparison the contribution of the two terms in the right hand side of the Eq. 3.12 in the temperature evaluation, the horizontal view is shown at the height of transition region in two different instance of time, $t = 80$ s in left and $t = 160$ s in the right panel of Fig. 3.8.

In the following, we will analyze in some more detail to what degree compression and Joule heating contribute to the evolution of the temperature. For this sake and in order to study the role of the forces involved in the energy conversion process, we performed a

3 About the relative importance of compressional heating and current dissipation for the formation of coronal X-ray Bright Points

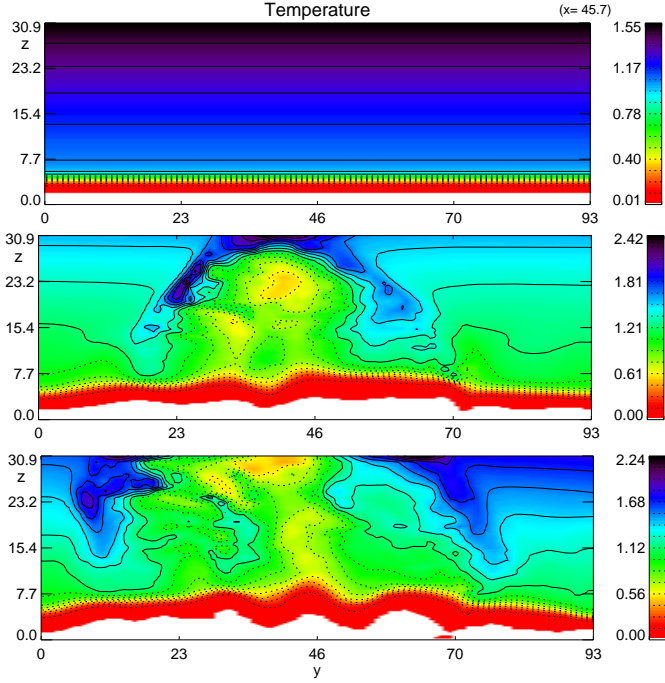


Figure 3.4: Temperature distribution in the vertical plane at $x = 45.7$ at the beginning (upper panel) and at $t = 80$ s and $t = 160$ s. Note the temperature in the color bar is presented in terms of the normalization value, $T_0 = 7.2 \times 10^4$ K. Spatial scale in units of $L_0 = 500$ km.

volume integration of the time rates of change of kinetic, magnetic and thermal energies in the simulation box above the chosen Bright Point region. Our approach is similar to Birm et al., (2009) when they used energy transport equations to analyze the properties of energy conversions associated with a reconnection process. The contribution of different terms in the energy transport process can be studied from the following equations:

$$\frac{d\epsilon_{kin}}{dt} = -\frac{1}{2} \int_{S_V} \rho u^2 \vec{u} \cdot d\vec{s} + \int_V (-\vec{u} \cdot \nabla p + \vec{u} \cdot \vec{j} \times \vec{B}) d^3v \quad (3.13)$$

$$\begin{aligned} \frac{d\epsilon_{mag}}{dt} = & -\frac{1}{\mu_0} \int_{S_V} (-\vec{u} \vec{B}^2 + (\vec{u} \cdot \vec{B}) \vec{B} - \eta \vec{j} \times \vec{B}) \cdot d\vec{s} \\ & + \int_V (-\vec{u} \cdot \vec{j} \times \vec{B} - \eta \vec{j}^2) d^3v \end{aligned} \quad (3.14)$$

$$\frac{d\epsilon_{th}}{dt} = -\frac{\gamma}{\gamma - 1} \int_{S_V} p \vec{u} \cdot d\vec{s} + \int_V (\vec{u} \cdot \nabla p + \eta \vec{j}^2) d^3v \quad (3.15)$$

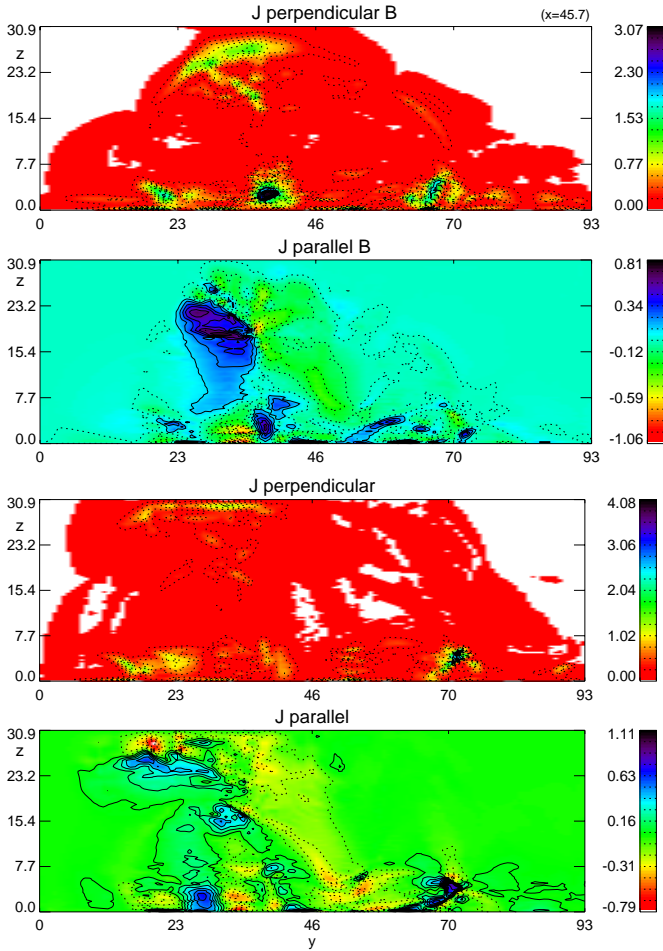


Figure 3.5: Parallel and perpendicular components of electrical current at $t = 80$ s (upper two panels) and $t = 160$ s (lower two panels) in the same diagnostic plane as in Fig.4. Note the enhancement in perpendicular current is located at the same place of the temperature maximum. Note the electrical current in the color bar is presented in units of $J_0 = 1.54 \times 10^{-4} A/m^2$. Spatial scale in units of $L_0 = 500$ km.

Where ε_{kin} , ε_{mag} and ε_{th} denote kinetic, $\rho u^2/2$, magnetic, $\vec{B}^2/2\mu_0$, and thermal, $P/(\gamma - 1)$, energies, respectively. The volume integrals (second term on the right-hand side) in these equations represent the energy conversion from one form into the another. This en-

3 About the relative importance of compressional heating and current dissipation for the formation of coronal X-ray Bright Points

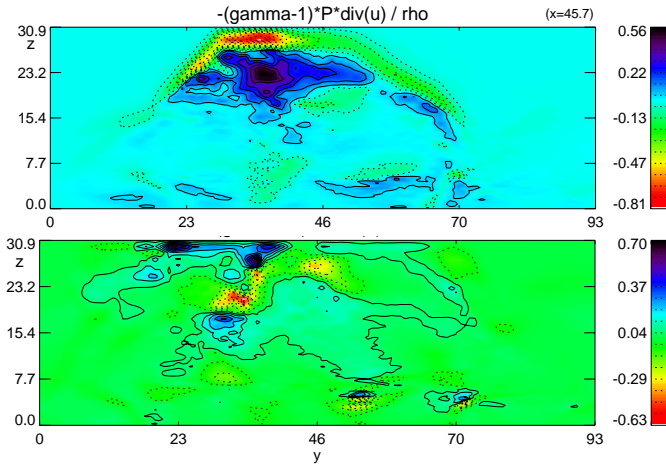


Figure 3.6: Adiabatic cooling/heating rate after 80 s and 160 s in the plane $x = 45.7$, according to the first term in the r.h.s of Eq. 3.12 over density, $(-\gamma - 1)T\nabla \cdot u < 0$). Color bar is normalized to $T_0/\tau_0 = 7.2 \times 10^3$ K/s. Spatial scale in units of $L_0 = 500$ km.

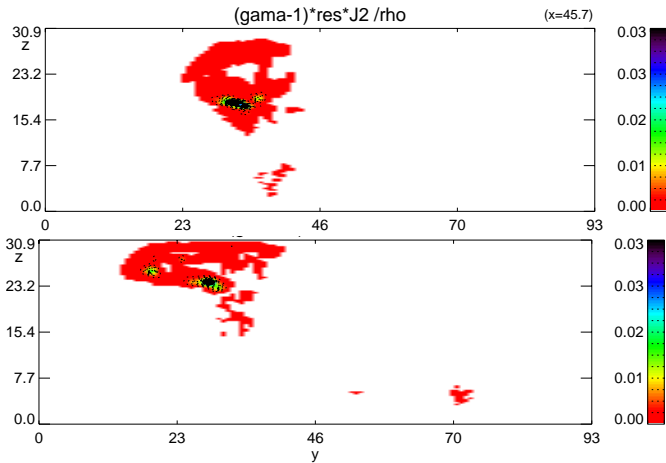


Figure 3.7: Joule heating rate, (second term in the r.h.s of Eq. 3.12, divided by density), after 80 s and 160 s in the plane $x = 45.7$. Physical units are the same as Fig. 3.6 with the same normalization for the color bar. Spatial scale in units of $L_0 = 500$ km.

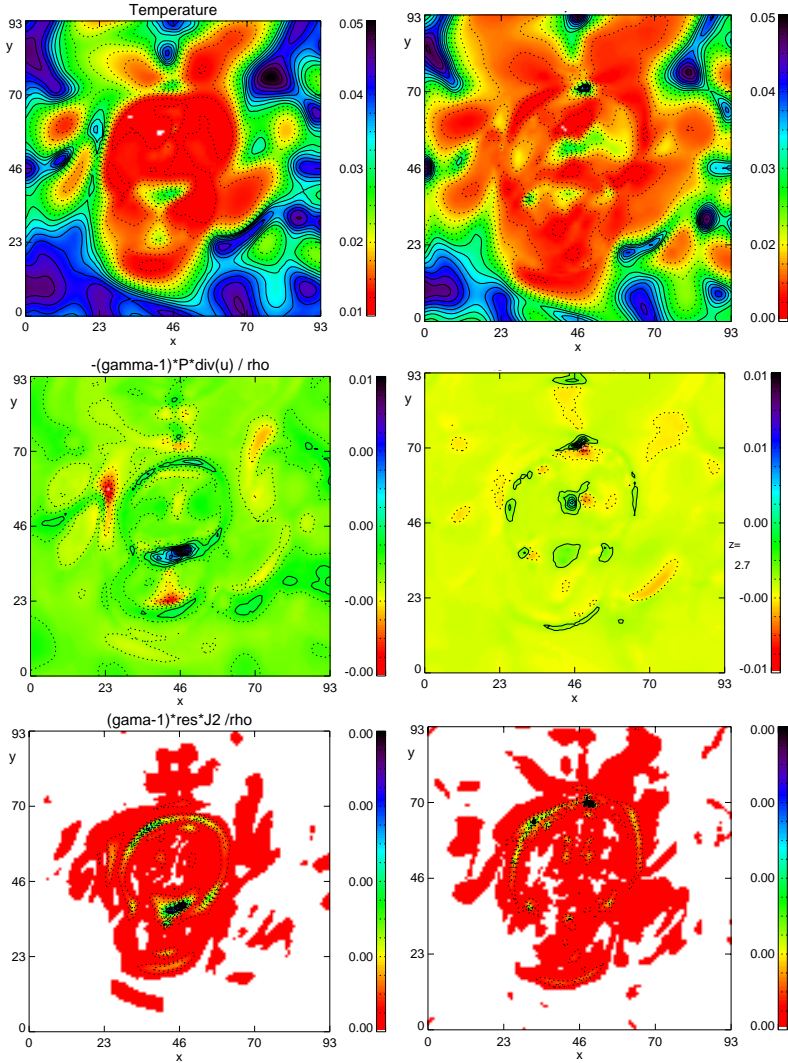


Figure 3.8: Temperature, first and second terms of Eq. 3.12 over density, in the top, middle and bottom panels, respectively. The result is shown at a horizontal plane in transition region at two instance of time, $t = 80$ s in left and $t = 160$ s in the right panels. Temperature is normalized to $T_0 = 7.2 \times 10^4$ K. The two other panels are normalized to $T_0/\tau_0 = 7.2 \times 10^3$ K/s. Spatial scale in units of $L_0 = 500$ km.

ergy conversion are explicitly written in terms of the work done by Lorentz force, pressure gradient force and Joule dissipation, (left panel of Fig. 3.9). Note that the initial spike in the Lorentz force is in part caused by numerical discretization errors and in part by the onset of photospheric footpoint motion. The initial oscillations are damped substantially during, approximately, two Alfvén times, followed by a state of an approximate force balance. This effect was found to be smaller in a run where footpoint motion was not included. The initial perturbation has a minor effect on the initial extrapolated magnetic field, it does not affect the currents and Lorentz forces at a later times.

The surface integrals are also needed to obtain the energy rates, when they indicate the transport of each of the three form of energies. With the chosen boundary condition however, the values of these surface integrals are zero at the lower boundary. They compensate each other through the side boundaries of the simulation box as well. At the upper boundary however, one needs to consider the contribution of this surface integrals in the rate of energy transfer. This means $\mathbf{E} \times \mathbf{B}$, $\mathbf{P}\mathbf{u}$ and $\rho\mathbf{u}^2\mathbf{u}$ for the transport of magnetic, kinetic and thermal energies, respectively. The values of these terms at the upper boundary are shown in Fig. 3.10. One can see that the contribution due to these terms is insignificant, so it would be a good approximation to consider only the volume integrals for the change in the energy rates.

The changes in energy rates are shown in the right panel of Fig. 3.9, the forces responsible for these changes are depicted in the left panel of the Figure. As one can see by comparing the two panels the magnetic energy is transferred to kinetic energy almost completely via the work done by the Lorentz force that accelerates the plasma. It is an intermediate step however, followed by the work done by pressure gradient force that converts kinetic energy into thermal energy. This decelerates the plasma motion until, finally, the Lorentz force is balanced. The direct transformation of magnetic energy to thermal energy (Joule heating) is via Ohmic current dissipation, ηJ^2 . A comparison of the energy conversions rates (see Fig. 3.9, right panel) however shows that Joule dissipation plays a minor role in the energy exchange process while the other contributions are orders of magnitudes larger. The minor role of Joule heating in comparison to adiabatic process in the increase of thermal energy was also found for the case of a solar flare by Birn et al., (2009), where they explained the compressional heating in two almost simultaneously steps: acceleration by Lorentz force and deceleration by pressure gradients.

3.4.2 Influence of different resistivity models

The previous calculation was based on an anomalous resistivity model with the current carrier velocity as a critical value for a local switch-on of additional resistivity. In order to better understand the influence of the resistivity we performed the simulation also with two other resistivity models, one that uses a current density dependent resistivity and another with constant resistivity respectively.

Fig. 3.11 depicts the resulting energy conversion rates and the work done by the involved forces $\mathbf{v} \cdot \mathbf{J} \times \mathbf{B}$, $\mathbf{v} \cdot \nabla P$ and by ηJ^2 , for all the three resistivity models by using different line styles for the results obtained by using the different resistivity model. The results obtained for the three cases show that the resistivity model influences the dynamics of the system and the thermal energy rate mainly through the pressure gradient force. While magnetic and kinetic energy rates of change depend only weakly on the resistivity

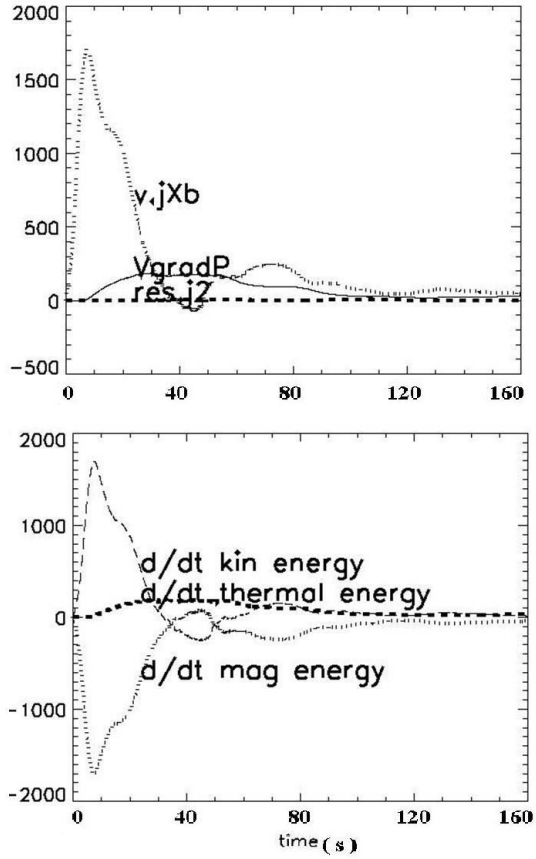


Figure 3.9: The work done by the Lorentz force, pressure gradient force and the Joule heating power, (top panel). The change of magnetic, thermal and kinetic energy rates, (bottom panel). Note that the values are measured in units of power, $\rho_0 V_{A0}^2 L_0^3 / \tau_0 = 1.04 \times 10^{14}$ W.

3 About the relative importance of compressional heating and current dissipation for the formation of coronal X-ray Bright Points

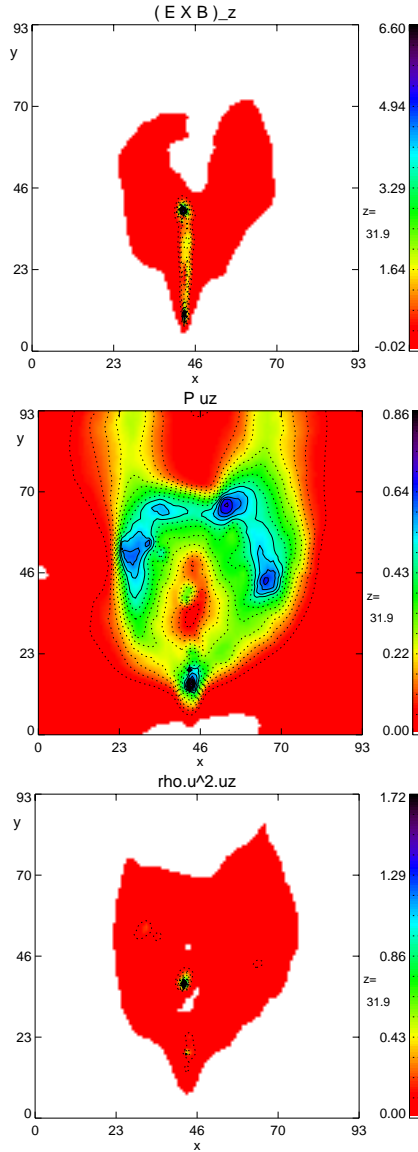


Figure 3.10: First term in the right hand side of the Eqs.13-15, (surface integrals) is shown in the upper boundary of the simulation box after 160 s. Note that the color bars are measured in units of energy densities over normalized time, $\rho_0 V_{A0}^2 L_0 / \tau_0 = 4.17 \times 10^2 \text{ W/m}^2$. Spatial scale in units of $L_0 = 500 \text{ km}$.

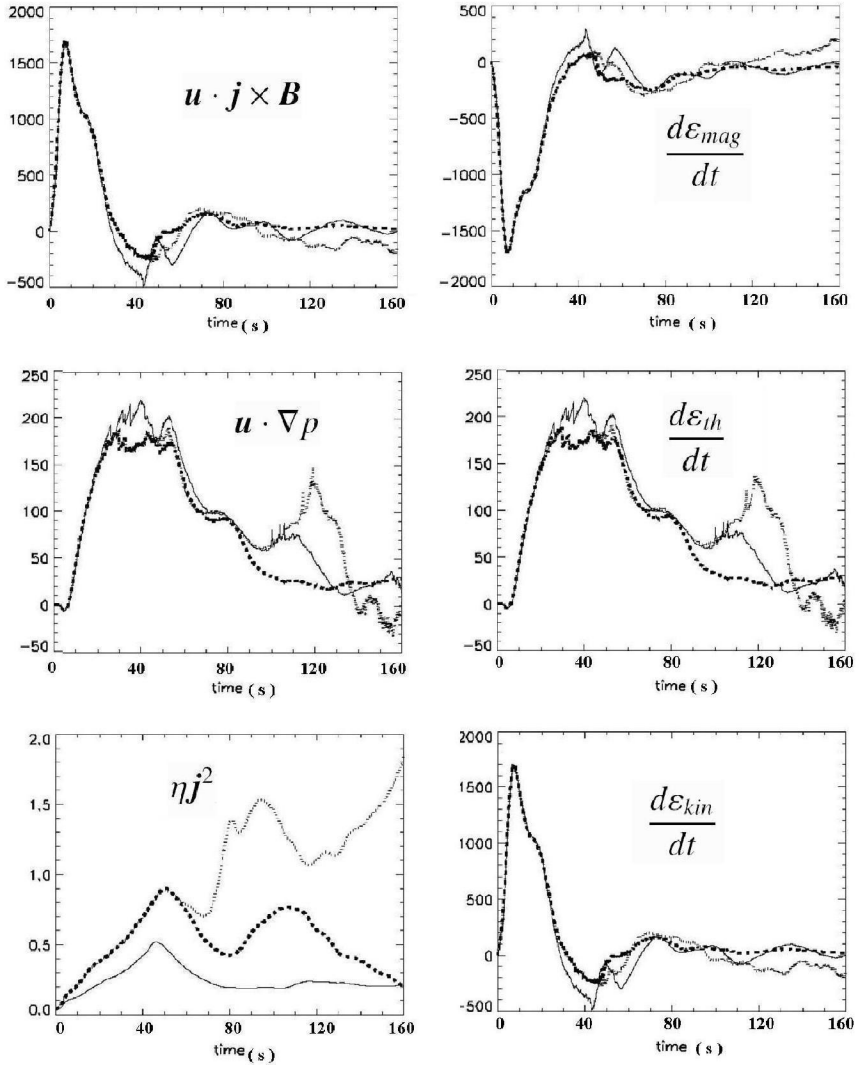


Figure 3.11: The left panels show the work done by the Lorentz force, pressure gradient force and the Joule heating power. Energy change rates for three different resistivity models are shown in right panels. Different lines correspond to anomalous current carrier dependent (dashed), anomalous current dependent (dotted) and constant (solid line) resistivity models. Note that the values are measured in units of power, $\rho_0 V_{A0}^2 L_0^3 / \tau_0 = 1.04 \times 10^{14}$ W.

model, the rate of temperature change is significantly influenced. Nevertheless, independent on the used resistivity model the heating is due mainly to the work done by the pressure gradient force. At the same time the contribution of the Joule heating is about two orders of magnitude smaller (Note the scale of the plots in the top row.) We conclude that the adiabatic compression is the dominant effect in increasing temperature in the BP region in all three cases.

3.4.3 Flux tube heating

In order to locate the heating effect better it is appropriate to determine it for individual flux tubes, integrating along the magnetic field lines instead of taking values averaged over the whole simulation box as reported in the previous sections. In this integration one has to take into account the changing cross-section of flux tubes. This can be done by applying the concept of the differential flux tube volume $V = \int B^{-1} ds$, where ds indicates the step size along the field line. This way the flux conservation in a flux tube ($\Phi = A \times B = const.$) is taken into account by the proportionality of the cross-section to B^{-1} . Note that large flux tube volumes correspond to field line rising high into the corona or hitting regions of vanishing magnetic field. The energy is transported in accordance with the upward directed Poynting flux $E \times B$, enhanced magnetic tension is carried away by wave propagation.

For the quantities described in section 3.4.1 the resulting flux tube integrated values are shown in Fig. 3.12 in the horizontal reference plane just above the transition region. The values reached indicate once more the negligible role of Joule heating by current dissipation for the thermal energy change in the bright point region compared to the dominant role of the pressure gradient force. Please note the different range of the plots in Figure 12 as indicated by the color bar. It also can be seen that the locations at which this force and also maximum rates of energy changes appear coincide. Furthermore, the same pattern has formed in the integration result of $v \cdot \nabla P$, $v \cdot J \times B$ and the rate of change of the different kinds of energy. This pattern can clearly be seen in the integration of total energy along the field lines (Fig. 3.13), which is the sum of the kinetic, magnetic and thermal energies:

$$\varepsilon = \varepsilon_{kin} + \varepsilon_{mag} + \varepsilon_{th} = \int_V \left\{ \frac{1}{2} \rho v^2 + \frac{1}{2\mu_0} B^2 + \frac{p}{\gamma - 1} \right\} d^3v$$

The left panel of Fig. 3.14 shows the result of this integration for temperature and flux tube volume. The coincidence of the temperature enhancement with the maxima obtained in the flux tube integrated energy change rates and forces shows that the heat is provided by the plasma compression due to the Lorentz force.

Enhanced flux tube integrated values follow the same pattern as the BP. This indicates that the regions of enhanced temperatures correspond to the foot points of field lines leading to higher altitudes or to regions where the magnetic field vanishes. The plasma motion across these regions supplies the magnetic energy that is converted to thermal energy.

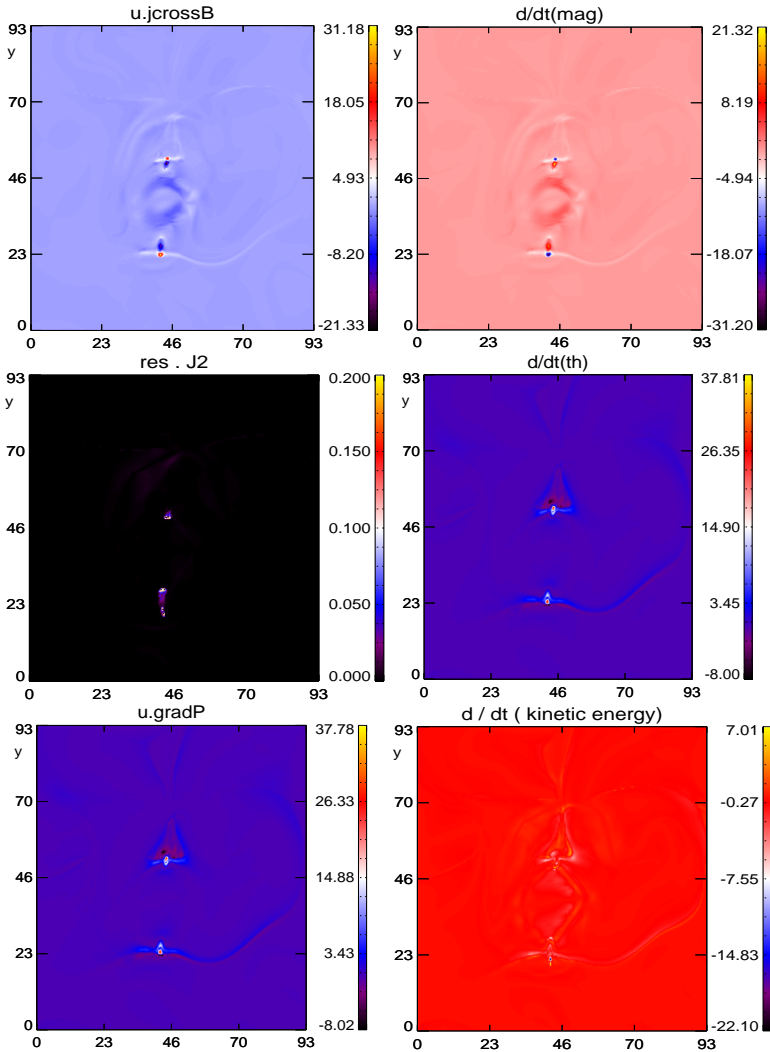


Figure 3.12: Integration along the field lines using the differential flux tube volume concept for the work done by Lorentz force, pressure gradient force and Joule heating, (right panel, from top to bottom), and the changes in rates of magnetic field change, the thermal and the kinetic energy, (left panel, from top to bottom) at $t = 160s$. Note that the color bars are normalized by power, $\rho_0 V_{A0}^2 / \tau_0 = 8.35 \times 10^{-4}$ W. Spatial scale in units of $L_0 = 500$ km.

3 About the relative importance of compressional heating and current dissipation for the formation of coronal X-ray Bright Points

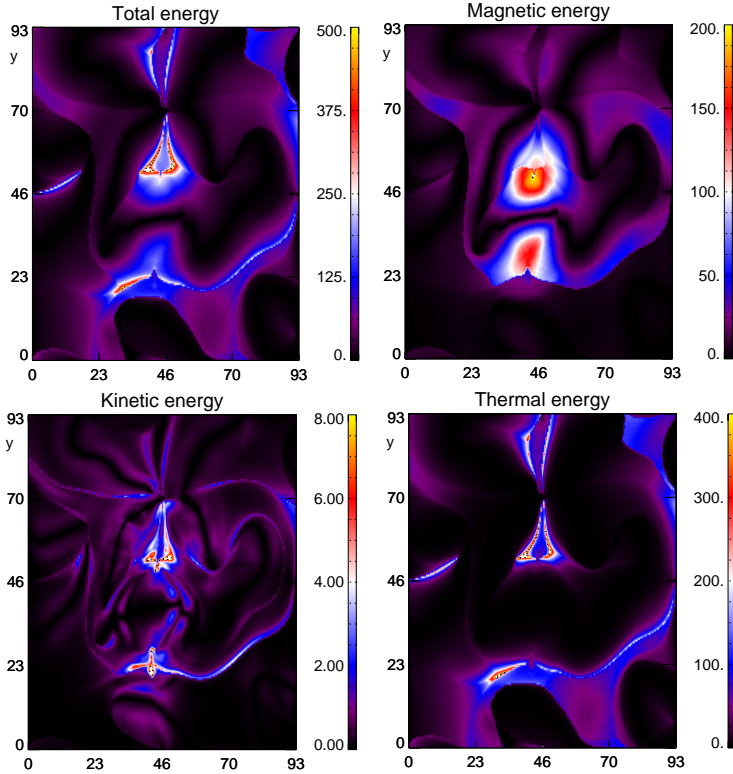


Figure 3.13: Results of integration along the magnetic field lines using the differential flux tube volume concept for the normalized total energy(top, left panel) and magnetic(top, right panel), kinetic(bottom, left panel) and thermal energies(bottom, right panel), at $t = 160s$. Note that the energies are normalized to $\rho_0 V_{A0}^2 = 8.35 \times 10^{-3} J$. Spatial scale in units of $L_0 = 500$ km.

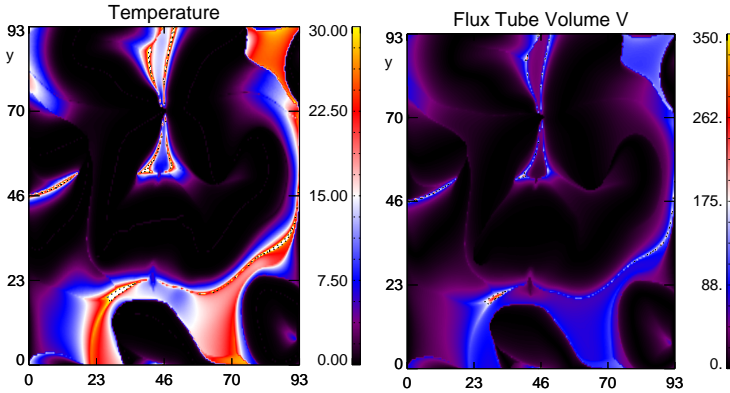


Figure 3.14: Temperature (normalized to 7.2×10^4 K) and flux tube volume (normalized to $L_0^3 = 1.25 \times 10^8 \text{ km}^3$), integrated along the magnetic field lines, at $t = 160s$. Spatial scale in units of $L_0 = 500 \text{ km}$.

3.5 Summary and discussion

We have presented the results of heating processes in the region of an observed X-ray coronal bright point. In particular we have investigated the importance of the work done by adiabatic compression in comparison with Joule heating in the course of the dynamic evolution and heat production near the bright point.

The simulation shows that an arc-shaped structure of enhanced temperature forms that is 2-4 times hotter than the background plasma. This structure is located above the two main opposite photospheric magnetic flux concentration. It coincides with the location where the electrical current densities are maximum. The structures of temperature and current density enhancements, indeed, coincide.

We further examined the contribution of the Lorentz force, pressure gradient force and Joule heating performing volume integrals in the simulation box that determine the magnetic, kinetic and thermal energy change rates for three different resistivity models. We found that independent on the resistivity model magnetic energy was transformed to kinetic energy through the work done by Lorentz force. Kinetic energy in turn is converted to thermal energy due to pressure gradients that balance the Lorentz force.

A comparison of the effect of the three energy conversion through $\mathbf{v} \cdot \mathbf{J} \times \mathbf{B}$, $\mathbf{v} \cdot \nabla P$ and ηJ^2 show that adiabatic compression has an important role in temperature increase in the upper corona. This is not dependent on the resistivity model used in the simulation.

For a better understanding of the heating processes we utilized the concept of differential flux tube integration of the different contributions along the magnetic field lines. A quantitative comparison in the horizontal plane, from where the integration starts, shows that energy conversion rate, total energies and work done by Lorentz and pressure gradient forces are located in the same flux tubes, also temperature and flux tube volume are maximum at the same place.

We conclude that the conversion of magnetic energy to kinetic energy via the work done by the Lorentz force and from kinetic to thermal energy due to the work done against the pressure gradient force determine the heating of this bright point. We could show that plasma compression dominates the heating of the bright point. In contrast, the role of Joule dissipation appeared to be negligibly small. The temperature enhancement follows the same pattern. The fact that the pattern obtained by calculating flux volume integrals coincides with the one of temperature and energy change rates bring us to the conclusion that plasma motion at the footpoints of the flux tubes carries the energy upward and makes the flux tubes rise to the higher corona. The magnetic energy is converted to thermal energy until the plasma compression is balanced by the Lorentz force. In the local, flux-tube oriented consideration we also could see that the role of the Joule heating in these energy conversion processes was negligible and the heating of plasma in the bright point region is basically due to pressure gradient force.

First, the fact that Joule heating is weak in the corona was not entirely unexpected but it is quantitatively confirmed here. It is worth to remember that the necessary up-scaling of the resistivity and of the onset condition of micro-turbulent anomalous resistivity to the resolved by the MHD simulation grid scales does even overestimate the actual Joule heating. As a result Joule heating cannot be considered a viable process unless there is a convincing argument that the dissipation regions are volume filling to a much larger extend than the already large one used in the present model.

Second, the results demonstrate very clearly that compression is an important processes in the energy budget. It is not clear in how far compression can contribute to the overall coronal heating but it is certainly important for the local heating of BPs.

Third, in this context the nature and the consequences of plasma compression are worth some consideration. In ideal MHD adiabatic compression is reversible. But the consequent flux tube heating is, however, irreversible due to magnetic reconnection and other mixing processes. Magnetic reconnection, in particular, changes flux tube identities (magnetic connectivity) while flux tube entropy conservation requires ideal MHD in addition to appropriate boundary conditions. Local adiabatic compression becomes irreversible also due to other plasma transport processes like heat conduction and radiative cooling. These aspects will be separately investigated in a subsequent paper. Meanwhile the results presented here clearly demonstrate that in the overall energy budget plasma compression (and expansion) can play an important role in the heating of the corona.

4 The consequences of the consideration of heat conduction and radiative loss in the formation of a coronal X-ray Bright Point

Our goal was to advance the modelling of the solar atmosphere by developing a more realistic simulation model. This requires the inclusion of additional physical processes involved in the energy balance of the system in order to give a reasonable picture of the thermal properties of the solar atmosphere. In comparison to a former work where the compressional heating and the Joule dissipation were the only heating sources for creating and maintaining a hot corona, here we add unisotropic heat conduction and the radiative losses for the optically thin atmosphere into the energy equation. In the upper solar atmosphere the coronal plasma is highly magnetically confined (low plasma- β). Hence the plasma motion across the magnetic field lines is strongly suppressed, and it is a reasonable assumption to consider heat conduction only along the magnetic field lines. In a simple 1D model for heat balance in the solar atmosphere, Priest 1982 proposed a hydrostatic heat balance between a heating function and the losses through heat conduction and radiative cooling. To address the importance of a heating mechanism one can mention that if there were no heat supply the thermal conduction and the losses can cool down the corona in a few hours or days, (see for example Aschwanden 2001). Using different assumptions this unknown heat source is entered in some simulation models in order to get a hot corona which can maintain the heat as well. For example, the 2D simulation model of (Von Rekowski B., Parnell C. E., Priest E. R., 2006a,b, Rekowski et al., 2008) explicitly considers an 'unknown' background heating term for this sake. In their 3D MHD simulation Peter et al., 2004, 2006 use high values of resistivity to obtain high Joule dissipation that provides adequate heat to balance the energy losses through conduction and radiation. In our model so far, however, we did not consider any artificial heating term. Therefore, with inclusion of the two energy loss mechanism we could expect a drop of the temperature, when no heating compensates the energy losses. However, this does not matter since we rather aim at an investigation of the role of individual source terms, rather than creating a hot corona. In the following, we explain how the parallel heat conduction and radiative losses were implemented, the way they are predicted to act and finally we show the changes in the simulation results after inclusion of these terms.

As in Chapter 3 we use the example of a BP observed on 19 December 2006 from a recent work as a reference case. Now the energy equation is however modified to include

4 The consequences of the consideration of heat conduction and radiative loss in the formation of a coronal X-ray Bright Point

the radiative losses for the optically thin atmosphere in the temperature range from 10^3 to 10^6 K. The classical Spitzer 1962 heat conduction is also included, that conducts back heat from the upper corona into the lower half of the atmosphere and the contrary for the upper half. Our simulation box covers the solar atmosphere for the lower boundary at the photosphere and extends to 15.45 Mm into the corona. Losses through the upper boundary are not included. As it will be shown in this case of a rather weak BP ($|B| < 40$ Gauss) the Poynting flux and the other energy fluxes through the upper boundary are negligible small, (see Chapter 3, 3.4.1).

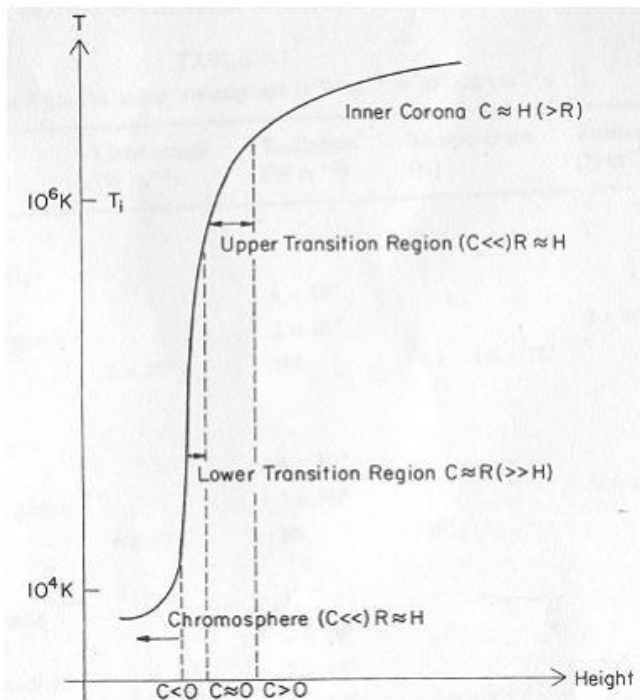


Figure 4.1: The temperature profile in the solar atmosphere is shown versus height, with relative roles of conduction (c), radiation (R) and heating (H). Note that the heat conduction is positive above the reflexion point of the heat flux function (T_i) and negative below it. Taken from Priest 1982.

Before presenting the model and the results of simulation, let us review an atmospheric model proposed by Priest 1982. In this model a thermal equilibrium is assumed at any location between heating (H), radiative losses ($-R$) and the divergence of a downwards conductive flux (C), so that $H = C + R$. The maximum temperature gradient is located at the base of the transition region where $T \approx 2 \times 10^4$ K. This is due to the high values of radiation losses (R) at temperatures $10^4 - 10^5$ K and causes strong temperature gradients

in the lower transition region. Hence heat is conducted from upper layers downward to balance the radiative cooling. The maximum heat flux maximum occurs at the inflexion point of the profile $T^{7/2}$, as shown in Fig. 4.1 at T_i , typically about 10^6 . Above this point however the deposited heating can not be radiated and needs to be transported away by e.g., solar wind.

In the following section 4.1 first properties of the numerical simulation model LINMOD3D are briefly reviewed. In section 4.2 simulation setup for the chosen case of a BP data is described. The simulation results can be found in section 4.3 and the consequences of heat conduction and radiative losses are discussed in 4.4. An analysis of the energy flows is provided in section 4.5. A flux tube related analysis is given and squashing factors are calculated in 4.6 and 4.7, respectively. Conclusions are drawn in 4.8.

4.1 The model

For the simulation we used the LINMO3D code (Büchner et al. 2004a,b,c), with line symmetric side boundary conditions (Otto et al., 2007). There the observed line-of sight (LOS) component of photospheric magnetic fields was used to perform a potential field extrapolation and provide the full vector of initial magnetic field for the simulation. The extrapolation is done in accordance with the requirement of MHD-consistent boundary condition, Otto et al., (2007). Plasma is assumed to be initially in hydrostatic equilibrium, which implies a constant initial pressure. The initial mass density profile is chosen based on the VAL model, Vernazza et al., 1981. The simulation box covers a horizontal square of $46.4 \times 46.4 Mm^2$ and extends 15.45 Mm toward the corona. The nonuniform grid in the z goes to $\Delta z = 160 km$ to resolve the transition layer. The set of MHD equations used in the model is given by Eqs.(2.1) - (2.6), (cf., Section 2.1). As described in section 2.1, neutral gas is coupled to plasma below the height of transition region via collisions. The source term, S , in the energy equation includes:

$$S = \eta j^2 - \nabla \cdot \mathbf{q} - L_r \quad (4.1)$$

where η is the resistivity coefficient. In addition to a uniform background resistivity η_0 due to binary collisions (Spitzer 1962), an anomalous resistivity can be switched on when the current carrier velocity (u_{cgv} determined as the current density divided by the charge density) exceeds the electron thermal velocity (Roussev et al., 2002, Büchner & Elkina 2006a,b):

$$\eta = \eta_0 + \begin{cases} 0, & \text{if } |u_{cgv}| < u_{crit} \\ \eta_{eff} \left(\frac{|u_{cgv}|}{u_{crit}} - 1 \right), & \text{if } |u_{cgv}| \geq u_{crit} \end{cases} \quad (4.2)$$

and η_{eff} can be expressed in terms of an effective collision rate as $\eta_{eff} = \frac{\nu_{eff}}{\epsilon_0 \omega_{pe}^2}$. Heat conduction, the second term in Eq.4.7, which is considered only for electrons and along the magnetic field:

$$\nabla \cdot \mathbf{q} = \nabla_{\parallel} \cdot (\kappa_{\parallel} \nabla_{\parallel} T) \quad (4.3)$$

with the classical Spitzer-value for κ_{\parallel} :

$$\kappa_{\parallel} = 1.8 \cdot 10^{-10} \frac{T^{5/2}}{\ln \Lambda} Wm^{-1} K^{-1} \quad (4.4)$$

that gives the typical values of $\kappa_{||} \approx 10^{-11} T^{5/2}$ with a Coulomb logarithm of $\ln\Lambda \approx 20$. Across the magnetic field the conduction is mainly due to ions and by some order of magnitudes lower. The last term in Eq.4.1 is the radiative loss function. For the optically thin layers of solar atmosphere (chromosphere and corona) it can be expressed as, Priest 1982:

$$L_r = n_e n_n Q(T) \quad (4.5)$$

$$\text{with } Q(T) = \chi T^\alpha \text{ W/m}^3 \quad (4.6)$$

where n_e is the electron density and n_n the density of protons. In the case of fully ionized plasma $n_n = n_e$. The coefficients χ and α are taken from Rosner et al., 1978. There a approximation by a powerlaw parameterization is given for the relevant temperature intervals. The analytic fit of Rosner et al., 1978 shows a maximum around 10^5 K for the radiative loss function.

4.2 Initial state

As in Chapter 3 we used for this study the X-ray Bright Point observed by XRT/Hinode spacecraft on 19 December 2006. We applied Fourier filtering to LOS component of magnetic field, taken from MDI-image of this BP at 22:17 UT, (Fig. 4.2, top panel). Then a potential field extrapolation was performed to have the full vector of magnetic field in the domain, (Fig. 4.2, bottom panel). The Bp is located close to the solar disc center and therefore we could take the LOS magnetic field as the normal component at the lower boundary of the simulation box. For the side boundaries a line symmetry with respect to the centers of the sides of the simulation box is used and at the upper boundary the normal derivatives are put to zero.

The photospheric plasma velocities are obtained by applying the local-correlation-tracking (LCT) method November & Simon 1988 to the Fourier filtered observed LOS magnetic components of the photospheric magnetic field, (see Fig. 3.3). The left panel of Fig. 3.3 shows the velocity arrows obtained by the LCT method. For the simulation we used incompressible velocity vortices as shown in the right panel of Fig. 3.3. Note that the interval chosen for the simulation starts a few hours after the time the BP first appeared in the X-ray images and that the bright point continues to glow a few more hours afterwards. During the whole simulation time interval the relative shear motion of the two main magnetic flux concentrations of opposite polarity continued.

4.3 Simulation results

The simulation results presented here are related to two cases: First the effect of heat conduction and radiative losses is studied and then it is compared to a reference case where they are not included. For the reference case that does not include the losses through conduction and radiation, Fig. 4.3 shows the temperature profile in a vertical cutting plane through the 3D simulation box which crosses the two main magnetic polarities. From top to bottom panel the temperature is shown 40, 80 and 120 s after the simulation was started. As one can see an arc of plasma with enhanced temperature is formed above the

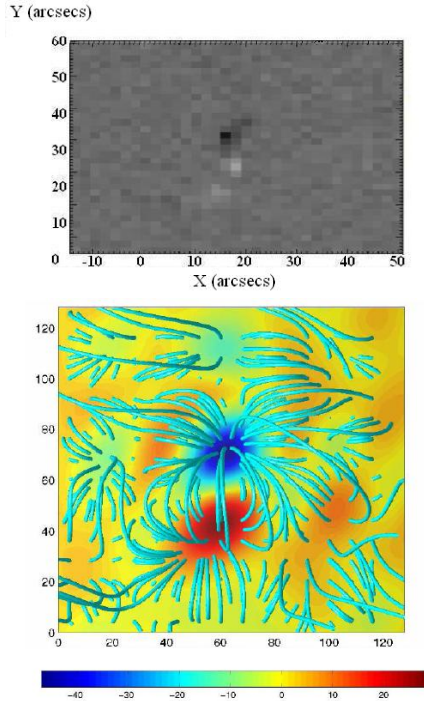


Figure 4.2: The Los component of the photospheric magnetic field of the BP observed on 19 December 2006 is shown in a $64 \times 64 \text{ arcsec}^2$ horizontal plane taken from MDI/Soho (top panel). White (black) spots correspond to upward (downward) directed Line-of-sight components of the photospheric magnetic field. Bottom panel is showing the top view of the 3D potential magnetic field extrapolated from the filtered MDI magnetograms and used as initial configuration for the magnetic field in our simulation. The color code depicts the LOS component of the magnetic field. Note that axes here are in terms of grid points, 64 in z direction and 128×128 in x,y plane. This corresponds to 15.45 Mm at z direction and 46.4 Mm at x and y directions.

two opposite magnetic polarities. For the same moments of time, the temperature profile is shown in Fig. 4.4 for the case that considers heat conduction and radiative losses. Despite the similar structure of the temperature enhancements in both cases, one can see a drop in temperature between 0.1–0.5 in normalized units, corresponding to $7.2 \times 10^3 - 10^4$ K. In a similar approach as described in Chapter 3, the continuity equation for the pres-

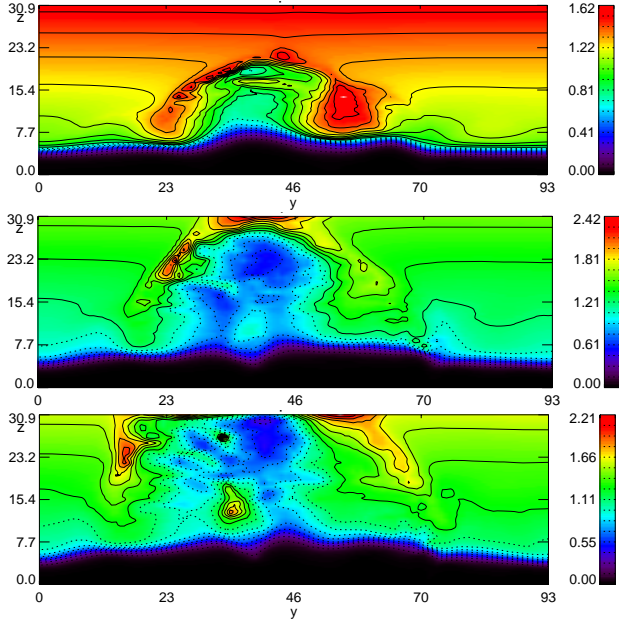


Figure 4.3: Temperature distribution is shown for the case without heat conduction and radiative losses in a vertical cutting plane through the simulation box, at $t=40, 80$ and 120 s. Note the temperature in the color bar is presented in terms of the normalization value, $T_0 = 7.2 \times 10^4$ K. Spatial scale in units of $L_0 = 500$ km.

sure evolution can be used to investigate the relative role of the different terms in the temperature evolution in the two cases. These terms are current dissipation and plasma compression, as can be see in the right hand of the equation:

$$\frac{\partial p}{\partial t} + \vec{\nabla} \cdot p\vec{u} = -(\gamma - 1)p\vec{\nabla} \cdot \vec{u} + (\gamma - 1)\eta j^2 \quad (4.7)$$

Using the equation of state for the fully ionized plasma $P = 2nkT$, and dividing $-(\gamma - 1)p\vec{\nabla} \cdot \vec{u}$ and $(\gamma - 1)\eta j^2$ by density, we have the right parameter to study the relative role of each term in temperature evolution. Fig. 4.5 is showing plasma compression over density in the same cutting plane used for the previous figures at $t=40, 80$ and 120 s for the case that does not include heat conduction and radiative losses. In Fig. 4.6 the temperatures are shown that are obtained when these two effects are involved. The structure of the regions

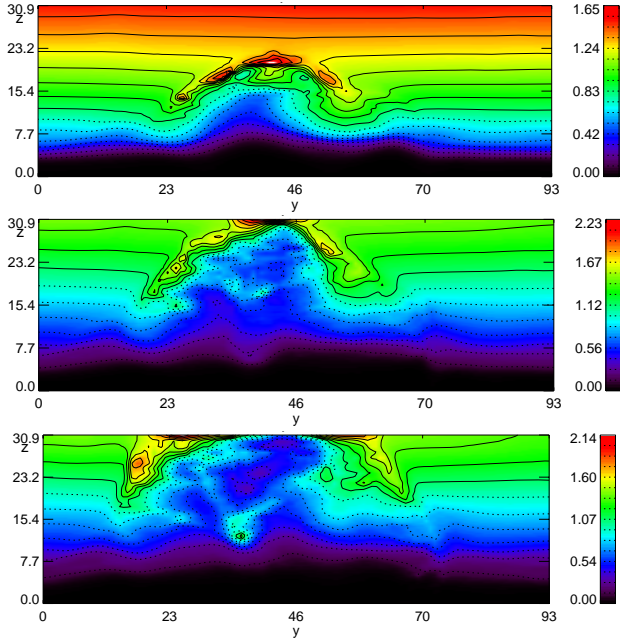


Figure 4.4: Temperature distribution in the case that heat conduction and radiative losses are included at $t=40, 80$ and 120 s, same cutting plane as in Fig. 4.4. Note the temperature in the color bar is presented in terms of the normalization value, $T_0 = 7.2 \times 10^4$ K. Spatial scale in units of $L_0 = 500$ km.

where adiabatic cooling and heating takes place coincide with regions of higher and lower temperatures, respectively. In the case of inclusion of heat conduction and radiative losses the compression term is less strong, as expected with the lower temperature maximum than in case where heat loss mechanisms are not considered. The current dissipation term over density is shown for the cases, without and with inclusion of heat conduction and radiative losses in Fig. 4.7 and Fig. 4.8, respectively. In both cases the contribution of the current dissipation is by an order of magnitude smaller than the compressional contribution to the heating.

4.4 Effect of the heat conduction and radiative loss

The radiative loss function $Q(T)$ and the inverse of the cooling time-scale due to radiation $1/dt_{cool}$ are shown in Fig. 4.9 and Fig. 4.10 respectively, at 40, 80 and 120 s of the simulation time. In order to estimate of the time rates of radiative loss one way is to use a

4 The consequences of the consideration of heat conduction and radiative loss in the formation of a coronal X-ray Bright Point

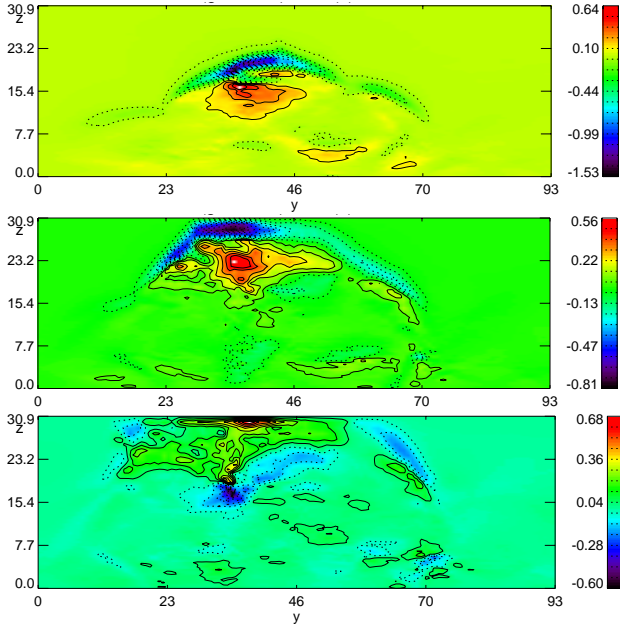


Figure 4.5: Temperature distribution in the case without heat conduction and radiative losses. Adiabatic cooling/heating rate according to the first term in the r.h.s of Eq. 4.7 over density, $(-\gamma - 1)p\nabla \cdot u/\rho < 0)$ is shown after 40, 80 and 120 s in the same vertical plane as temperature. Color bar is normalized to $T_0/\tau_0 = 7.2 \times 10^3$ K/s. Spatial scale in units of $L_0 = 500$ km.

reduced version of the energy equation:

$$\frac{\partial p}{\partial t} = -(\gamma - 1)n_e n_n Q(T)$$

where $Q(T) = \chi T^\alpha$ W/m³. Using the equation of state of a fully ionized plasma we get:

$$1/dt_{cool} = (\gamma - 1)n_e Q(T)/T \quad (4.8)$$

Therefore the rate at which radiation can cool down the plasma depends on the temperature ranges, as $Q(T)$ changes according to Rosner et al., 1978. The fastest rates of cooling ranges from 1-3 units in simulation time for the upper atmosphere in the regions of the loop connecting the two main magnetic polarities. For the lower transition region or region of the atmosphere where the temperature is lower than the minimum temperature at which radiative loss is efficient, the $1/dt_{cool}$ goes to zero which corresponds to infinite cooling time. When radiative cooling and heat conduction are taken into account in addition to Joule dissipation, the temperature profile is smoothed out as can be seen

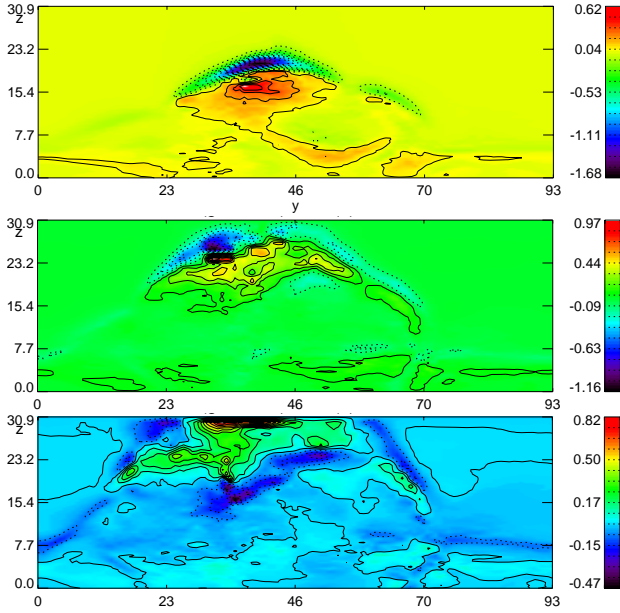


Figure 4.6: Adiabatic cooling / heating rates (first term in the r.h.s of Eq. 4.7 over density), if heat conduction and radiative losses are taken into account. Physical units are the same as Fig. 4.5 with the same normalization for the color bar. Spatial scale in units of $L_0 = 500$ km.

in Fig. 4.11. The pressure is related to temperature via the equation of state. For the current model calculations that not include gravity, the initially constant pressure drops at the height of the transition region. This results from radiative and conductive loss of the thermal energy. For a better understanding of the changes in the temperature profile we compared it with the result of the case that does not include these loss terms. For this sake in the upper and lower panel of Fig. 4.12 the temperature profiles are shown after $12\tau_{Alfven}$ for the cases without / with radiative loss and heat conduction, respectively. The parallel and perpendicular components of the electrical currents with respect to the main magnetic field direction are shown versus height in Fig. 4.13, similar to the temperature profile after $13\tau_{Alfven}$ for the cases without / with radiative loss and heat conduction in the upper /lower panels, respectively. As one can see comparing Figs the difference between the two cases is almost negligible, although the values that are being compare here have been averaged over $(x-y)$ plane for each height. The difference appears in the resistivity values so that the profile of ηJ^2 , shown by dashed lines in Fig. 4.13 differs for the two cases.

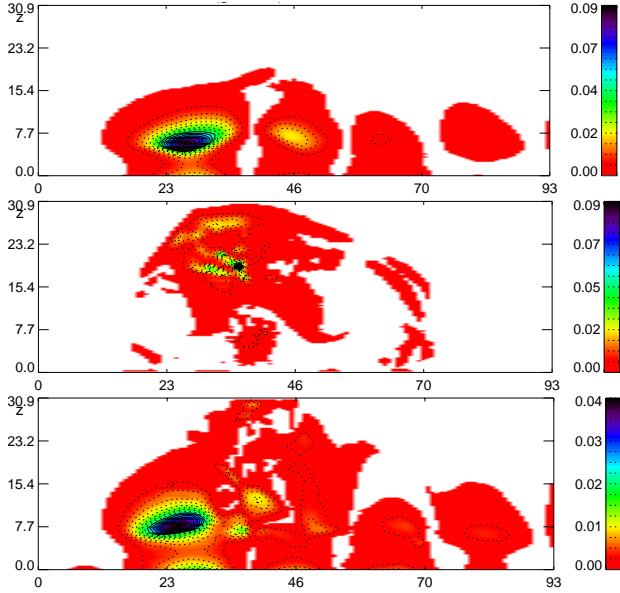


Figure 4.7: For the case without heat conduction and radiative losses, adiabatic cooling/heating rates are shown according to the second term in the r.h.s of Eq. 4.7 over density, $(-\gamma - 1)\rho \nabla \cdot u / \rho < 0$) after 40, 80 and 120 s in the plane $x = 45.7$. Physical units are the same as Fig. 4.5 with the same normalization for the color bar, $(T_0/\tau_0 = 7.2 \times 10^3$ K/s). Spatial scale in units of $L_0 = 500$ km.

4.5 Analysis of the energy transport

In order to understand better the redistribution of energy due to radiative losses and thermal conduction it is appropriate to analyze their time variation. The time variations of magnetic, kinetic and thermal energies can be obtained, performing the volume integrals of the energy densities in the simulation box. Fig. 4.14 is showing the integrated energies versus time for the cases without / with inclusion of heat conduction and radiative losses in the upper / lower panel. The drop in the thermal energy for the latter case indicates the strength of the radiative and conductive energy loss. When the existing sources (Joule dissipation and compressional heating) do not provide adequate heat to compensate the loss total energy is lost:

$$\varepsilon = \varepsilon_{kin} + \varepsilon_{mag} + \varepsilon_{th} = \int_V \frac{1}{2} \rho u^2 d^3v + \int_V \frac{1}{2\mu_0} B^2 d^3v + \int_V \frac{P}{\gamma - 1} d^3v$$

where ε_{kin} , ε_{mag} and ε_{th} denote kinetic, magnetic and thermal energies, respectively. A direct consequence of the dropping thermal energy due to the two heat loss terms is a drop

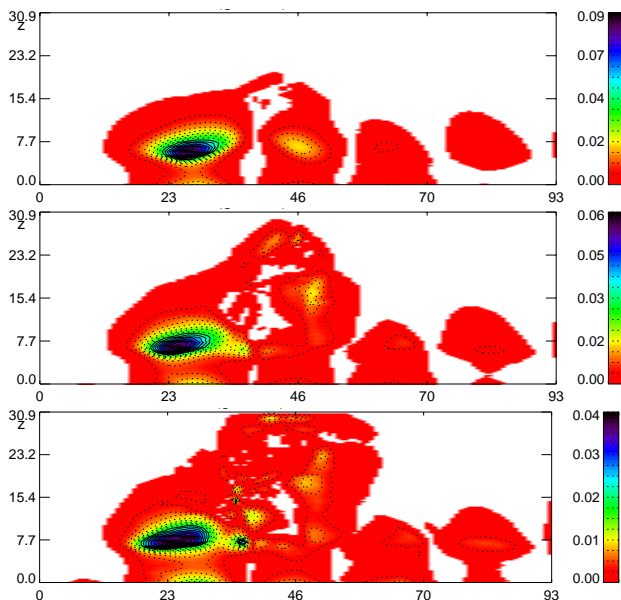


Figure 4.8: Adiabatic cooling / heating rate according to the second term in the r.h.s of Eq. 4.7 over density, for the case that includes heat conduction and radiative losses. Physical units are the same as Fig. 4.7 with the same normalization for the color bar. Spatial scale in units of $L_0 = 500$ km.

in coronal temperature, (lower panel of Fig. 4.12). Since we focus on the investigation of the consequences of radiative loss and heat conduction, we did not include any ad-hoc background heating source to compensate heat losses and to maintain the coronal temperature. As it was shown in Chapter 3, 3.4 the energy conversion rates depend mainly on the work done by the Lorentz force, the pressure gradient force and Joule dissipation. Similar to an approach used by Birn et al., 2009 for the case of a solar flare, we calculate each of the terms $\mathbf{v} \cdot \nabla P$, $\mathbf{v} \cdot \mathbf{J} \times \mathbf{B}$ and ηJ^2 in the simulation box, depicted in left panel of Fig. 4.15. The profiles depicted in this Figure show some differences between the top and bottom panels which correspond (cases without and with inclusion of heat conduction and radiative losses, respectively). For both cases the model starts with already existing electrical currents that explains the appearance of the initial large Lorentz forces as soon as velocity vortices are inserted. Inclusion of the two heat loss mechanism does not change the dominance of the contribution of the work done by the pressure gradient force over the effect of Joule dissipation. The influence of resistivity values and consequently, different values of Joule dissipation, is illustrated by Fig. 4.16. Despite higher values of Joule dissipation (ηJ^2) for the case that include heat conduction and radiative losses (lower panel) in comparison to the case that does not include these two heat loss effects (upper panel), in both cases Joule dissipation is many order of magnitudes smaller than the work

4 The consequences of the consideration of heat conduction and radiative loss in the formation of a coronal X-ray Bright Point

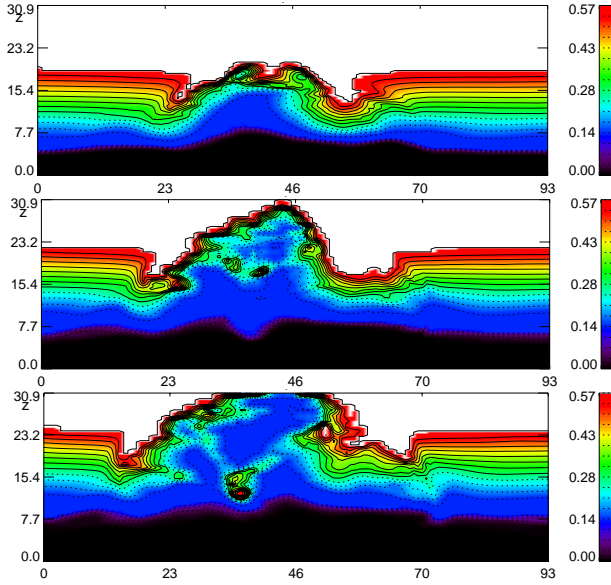


Figure 4.9: Radiative losses function after 40, 80 and 120 s in the same vertical plane as Fig. 4.8.

done by the pressure gradient force. The energy conversion rates are related to the volume integrals of the following combinations of $\mathbf{v} \cdot \nabla P$, $\mathbf{v} \cdot \mathbf{J} \times \mathbf{B}$ and by ηJ^2 :

$$\frac{d\mathcal{E}_{kin}}{dt} \longrightarrow \int_V (-\vec{u} \cdot \nabla p + \vec{u} \cdot \vec{j} \times \vec{B}) d^3v \quad (4.9)$$

$$\frac{d\mathcal{E}_{mag}}{dt} \longrightarrow \int_V (-\vec{u} \cdot \vec{j} \times \vec{B} - \eta \vec{j}^2) d^3v \quad (4.10)$$

$$\frac{d\mathcal{E}_{th}}{dt} \longrightarrow \int_V (\vec{u} \cdot \nabla p + \eta \vec{j}^2 + S) d^3v \quad (4.11)$$

The source term S in the thermal energy change rate ($d\mathcal{E}_{th}/dt$) is either in the case without heat loss terms just due to Joule dissipation $S = \eta J^2$ or in the case including heat conduction and radiative losses $S = \eta \vec{j}^2 - \nabla_{\parallel} \cdot (\kappa_{\parallel} \nabla_{\parallel} T) - 0.83 \rho^2 \chi T^{\alpha}$. The energy rates are shown in the upper and lower rows of the right panel of Fig. 4.15, respectively. In both cases thermal energy can increase in two ways, first via a direct exchange with magnetic energy through the Joule dissipation and at second indirectly from the kinetic energy due to work done against the pressure gradient force that balances the Lorentz force. In fact, in both cases the Joule heating is much less powerful than the pressure gradient force $\mathbf{v} \cdot \nabla P$, (left panel of Fig. 4.15). In the case without radiative and conductive heat losses one would expect that the thermal energy follows a similar pattern as $\mathbf{v} \cdot \nabla P$. This is indeed the case (upper row of this Figure). Lower panel illustrates the strong drop in thermal energy

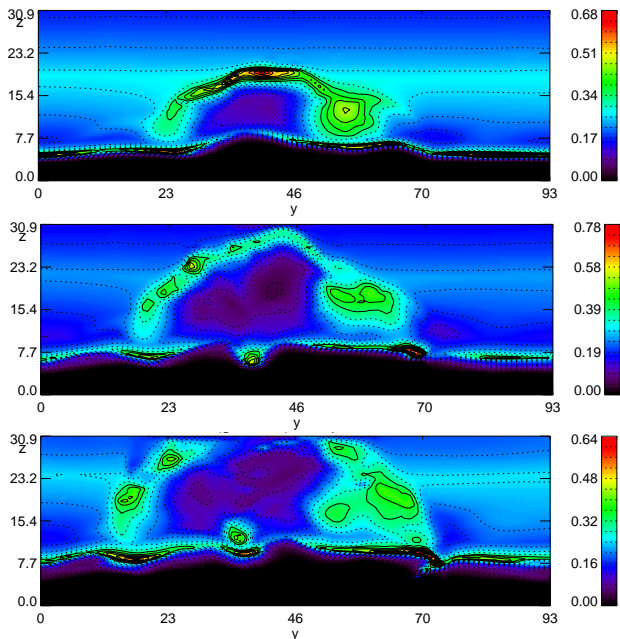


Figure 4.10: The inverse of the radiative cooling time-scale $1/dt_{cool}$ after 40, 80 and 120 s in the same vertical plane as in Fig. 4.9.

due to the heat loss terms. The contribution of heat conduction is depicted versus time in Fig. 4.17. The heat conduction considerably increases with anomalous resistivity rises, (see lower panel of Fig. 4.16). At the other moments of time its contribution is on average less than Joule heating. The radiative cooling $Q(T)$ is defined to be less than 1 ($Q(T) < 1$). In the temperature range of our simulation this value does not exceed 0.57, (see Fig. 4.9). Since the contribution of radiative losses is proportional to the electron density $n^2 Q(T)$, an efficient heat loss takes place at high density regions. The energy balance in this case would require additional heating to compensate the heat loss.

4.6 Analysis of the thermal balance along magnetic flux tubes

Since the magnetic field determines the spatial structure of the heat distribution it is appropriate to analyse the results by means of an integration along magnetic flux tubes. For this sake integration of physical quantities along the magnetic field lines using differential flux tube volume, ($V = \int B^{-1} ds$, with ds indicating the step size along the field line) has

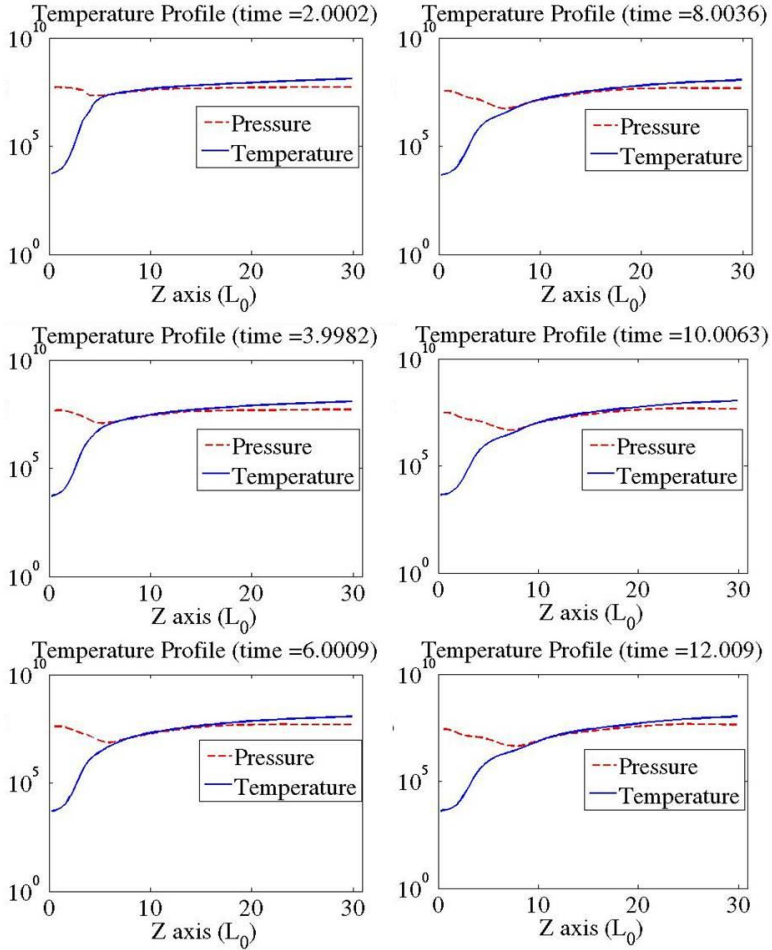


Figure 4.11: Horizontally averaged temperature versus the height shown for every 20 s interval of the simulation time.

to be carried out, (see Chapter 3, 3.4.3). Large flux tube volumes correspond to field line rising high into the corona or hitting regions of vanishing magnetic field. We analyze the Lorentz force, pressure gradient force and Joule dissipation. In Fig. 4.18 the corresponding rates of energy change in the flux tube are depicted by color coding their flux tube integrated values at the corresponding photospheric footpoints. The plots in the upper row of the Figure correspond to the case that does not include the heat loss terms and the lower panels refer to the case with heat conduction and radiative losses. The results are

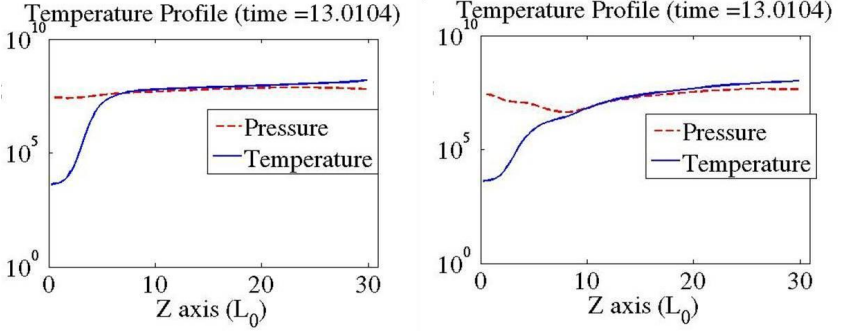


Figure 4.12: The averaged temperature profiles are shown versus the normalized height is shown after 130 s for the cases without / with radiative loss and heat conduction in the left / right panel, respectively.

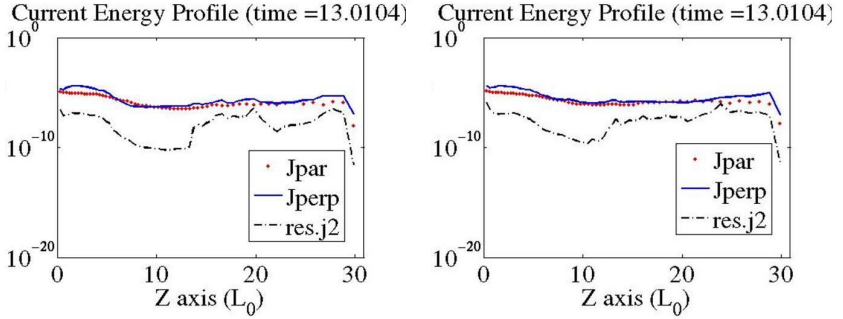


Figure 4.13: Parallel (dotted line) and perpendicular (solid line) components of the electrical current with respect to the main magnetic field averaged over the horizontal (x - y) plane and depicted versus height. The dash-dotted line depicted the Joule heating power, ηJ^2 . The result is shown after 130 s for the cases without / with radiative loss and heat conduction in the left / right panel, respectively.

projected in a horizontal plane located just above the transition region height, where the flux tube integration starts. A comparison of the effect of Joule heating with the work done by pressure gradient force in this way again confirms the minor role of Joule dissipation for changing the thermal energy in the BP region. The major difference between the two cases appears in the thermal energy rate of change. With heat conduction and radiative losses (depicted in lower right panel of Fig. 4.18) the thermal energy experiences a much stronger change than the case without these two heat loss terms (see upper right panel of the same Figure). Apart from the qualitative differences, also the location of the enhanced flux tube integrated $\mathbf{v} \cdot \nabla P$, $\mathbf{v} \cdot \mathbf{J} \times \mathbf{B}$ and ηJ^2 as well as the rate of the magnetic, kinetic and thermal energy changes coincide. The results of the integration for the total energies are depicted in Fig. 4.20 after 60 and 120 s with upper/lower rows referring to the

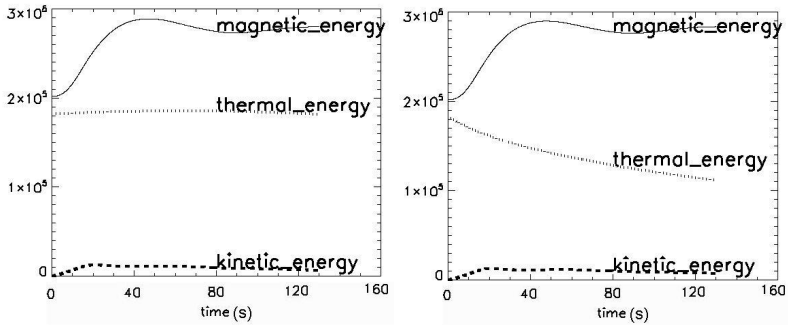


Figure 4.14: The profile of magnetic, kinetic and thermal energies are depicted versus time for the cases without / with inclusion of heat conduction and radiative losses in the left / right panels.

cases without/with heat conduction and radiative losses. In the case in which these two heat loss effects have been considered obviously the total energy is smaller and decreases over time, (compare the left and right panels of the lower row in Fig. 4.20). The result of the flux tube integration of the different kinds of energy is depicted in Fig. 4.21 (again with upper/lower rows referring to the cases without/with heat conduction and radiative losses). It shows that the drop in total energy is mainly due to the smaller thermal energy compared to the case that includes the two heat loss terms. The magnetic and kinetic energies on the other hand, are enhanced compared to the case without the heat loss terms, (upper panel of this Figure). One can notice a very similar pattern in flux tube integrated forces, energies and energy rate of changes. In particular, thermal energy and the pressure gradient force are following the very same pattern as the temperature and flux tube volume in Fig. 4.22. There again the upper/lower rows are referring to the cases without/with heat conduction and radiative losses. Although inclusion of the two heat loss effects results in a lower temperature (thermal energy), it does not change the dynamics of the system which is rather determined by magnetic configuration and plasma velocities. The regions with enhanced flux tube volume appear at the foot points of flux tubes that have received enough energy through the Lorentz force to expand into higher altitudes and / or are connected to regions with Separatrix-Like magnetic structures. The plasma compression acts to balance the enhanced Lorentz force and to increase the temperature (thermal energy) of the plasma.

4.7 Squashing factor calculations

Let us look at the magnetic geometry of the BP region in some more details. A proper way to measure the change of the magnetic connectivity is to calculate the squashing factors, introduced by Titov et al., 2002. Connectivity of the magnetic field lines is a geometrical property of magnetic configuration. It is not expected to change much due to the additional heat loss terms in the model. The result of the calculation of the squashing factor

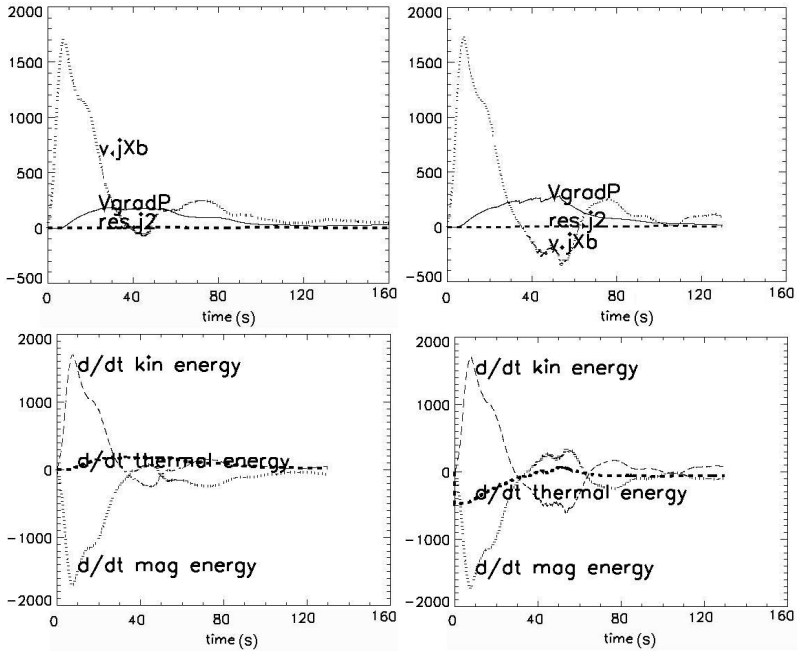


Figure 4.15: The work done by pressure gradient force ($v \cdot \text{grad}P$), Lorentz force ($v \cdot J \times B$) and the contribution of Joule dissipation ($\text{res.}J^2$), left panels. Upper / lower panels are correspond to the cases without / with heat conduction and radiative losses. Right panels: Magnetic, kinetic and thermal energy rates of change. Note that the values are measured in units of power, $\rho_0 V_{A0}^2 L_0^3 / \tau_0 = 1.04 \times 10^{14}$ W.

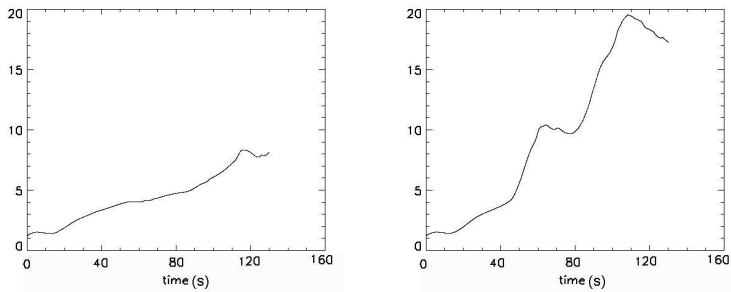


Figure 4.16: Joule heating function (ηJ^2). Left / right panels refer to the cases without / with heat conduction and radiative loss. The simulation time is given in terms of Alfvén times (here $\tau_{\text{Alfvén}} = 10$ s).

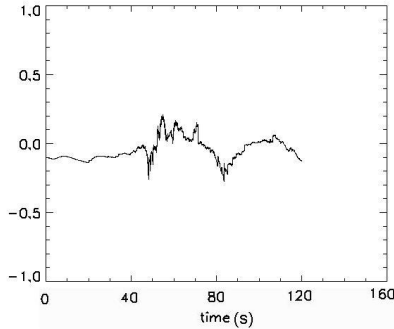


Figure 4.17: Time evolution of the heat conduction function, according to Eq. 4.3, $\nabla_{\parallel} \cdot (\kappa_{\parallel} \nabla_{\parallel} T)$.

for the cases without / with inclusion of heat conduction and radiative loss is depicted in the upper / lower panels of Fig. 4.23, respectively. Despite some qualitative differences in the values, the locations with the enhanced squashing factors coincides for two cases very well. In comparison with result of the flux tube volume integrations (see right panel of Fig. 4.22), one can see part of the regions with higher change of magnetic connectivity (colorbar is shown in logarithmic units) coincide with the regions with higher flux tube volume and temperature. Therefore regions of enhanced flux volume that experience strong changes of the magnetic connectivity are more likely to be associated with stronger Poynting fluxes and enhanced temperatures.

4.8 Conclusions

We studied the consequences of a more realistic modelling of an observed X-ray coronal bright point and compared it to a former work. For this sake we include heat conduction and radiative losses and studied the changes in the energy balance in the BP region due to these two additional heat loss effects.

Similar to a case where both heat loss effects were neglected (Chapter 3), the source of heating were mainly adiabatic compression and only to a small amount Joule dissipation. An arc-shaped structure of enhanced temperature forms hotter than the background plasma and connecting the two main opposite photospheric magnetic flux concentration. The heat losses due to conduction and radiation change the temperature profile in two ways. First they decrease the maximum values of temperature. This is due to mainly, radiative loss below the chromospheric heights. There due to higher plasma density radiative cooling $n^2 Q(T)$ can act more effectively. At second the heat loss decreases temperature gradient in the transition region by conducting heat from upper hot atmosphere to the lower region where they can be radiated away. This result in a less steep temperature gradient. The changes in the temperature of the layered solar atmosphere are smoothed accordingly.

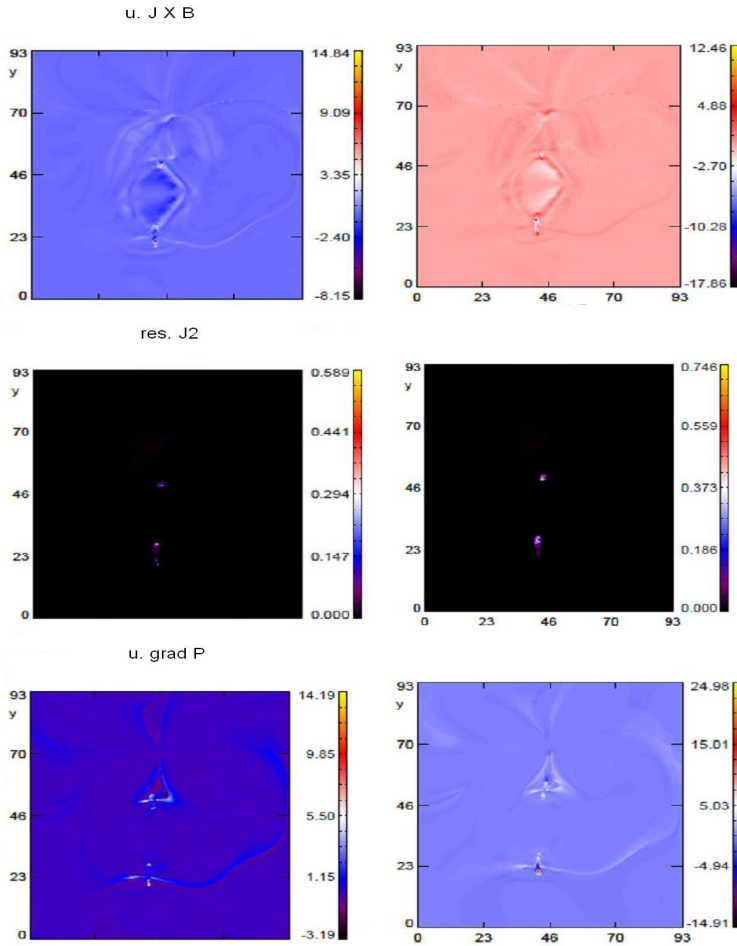


Figure 4.18: Flux tube integrated work done by the Lorentz force, pressure gradient force and Joule heating are depicted in the top, bottom and middle panels, respectively. The left/right rows are referring to the cases without/with heat conduction and radiative losses.

4 The consequences of the consideration of heat conduction and radiative loss in the formation of a coronal X-ray Bright Point

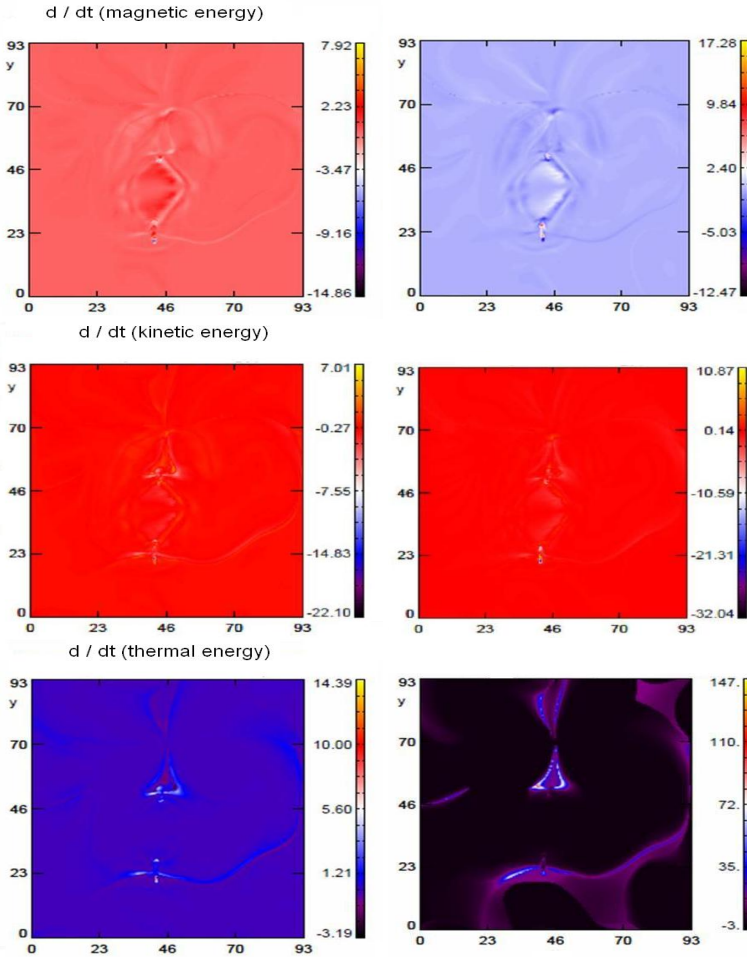


Figure 4.19: Rates of the magnetic, kinetic and thermal energy changes, integrated along the magnetic field lines are depicted at $t = 120$ s in the top, middle and bottom panels, respectively. The left/right rows are referring to the cases without/with heat conduction and radiative losses.

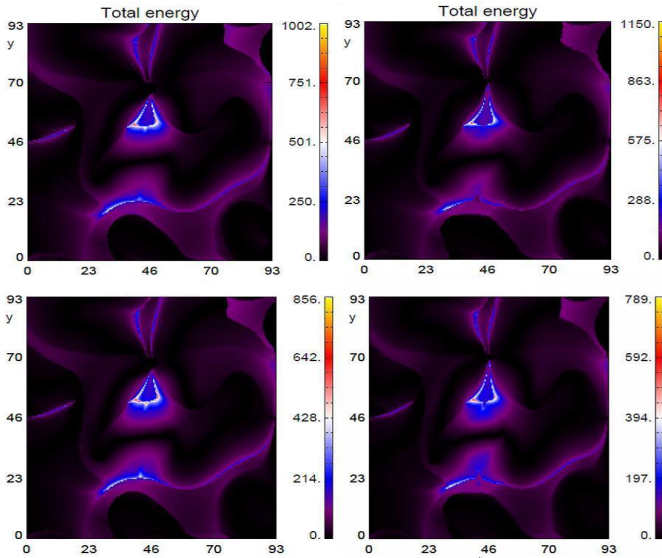


Figure 4.20: The total energy integrated along the magnetic field lines using the differential flux tube volume concept, (cases without/with heat conduction and radiative loss in upper/lower rows respectively, at 60 s (left panels) and 120 s (right panels) of the simulation time).

The inclusion of the heat loss terms does not change however, the coincidence of the locations of the enhanced current densities and temperature. The current density profiles also do not change significantly. We also compared the relative role of the Lorentz force, pressure gradient force and Joule heating in the energy change rates for the two cases with and without heat conduction and radiative losses involve. After inclusion of the two heat loss terms the plasma compression is still much more effectively enhancing the thermal energy and temperature in the BP region.

Using the concept of differential flux tubes, we performed the integration of different contribution along the magnetic field lines. The integration results are compared in a horizontal plane, from where the integration along the field lines starts. In both cases these integrations show that the increase in thermal energy is provided mainly by the work against the pressure gradient force rather than directly from magnetic energy via the Joule dissipation. The major effect of the inclusion of the heat loss effects is a significant drop in thermal energy and temperature. This shows that the energy balance in presence of these heat loss effect requires an additional heat source to balance the energy losses. Despite the quantitative difference, the structure of the heating sites is very similar. In particular, temperature and flux volume integrated quantities follow the same pattern. This indicates that regions of enhanced temperature are connected to the footpoint motion of the flux tube that are carrying upward Poynting flux. This makes the flux tube rise into the higher

4 The consequences of the consideration of heat conduction and radiative loss in the formation of a coronal X-ray Bright Point

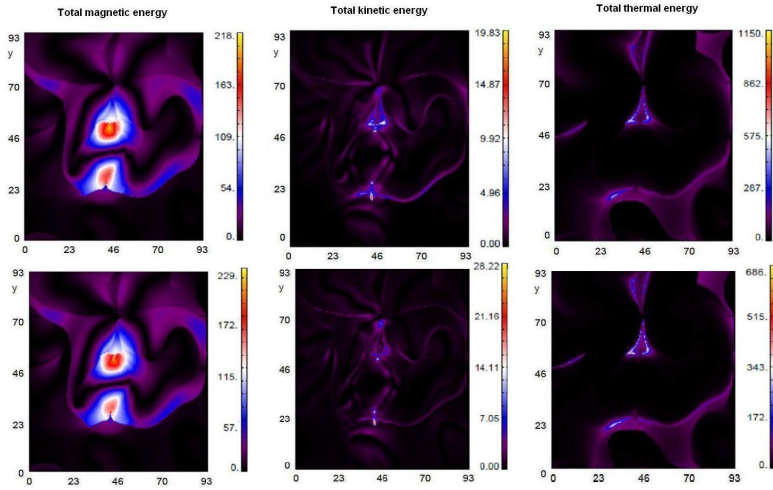


Figure 4.21: Magnetic, kinetic and thermal energies integrated along the magnetic field lines are depicted after 120 s of the simulation time. The upper/lower rows refer to the cases without/with heat conduction and radiative losses.

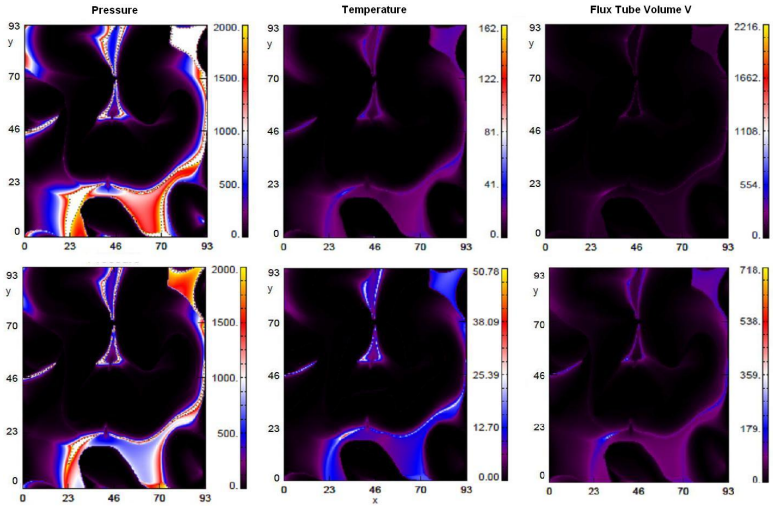


Figure 4.22: Pressure, temperature and flux tube volume, integrated along the magnetic field lines, at $t=120$ s. The upper/lower rows are referring to the cases without/with heat conduction and radiative losses.

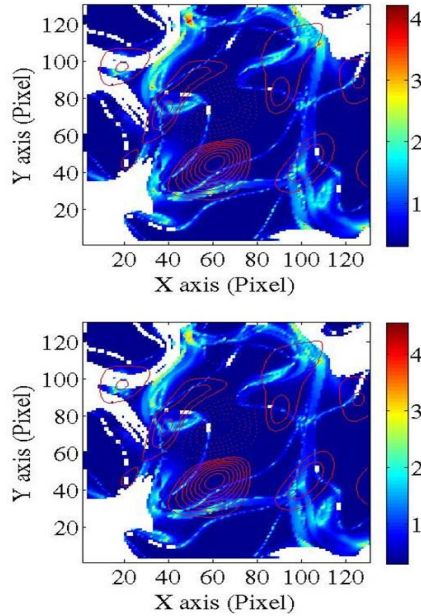


Figure 4.23: The result of the calculation of the squashing factor is shown (using a logarithmic colorbar), when upper/lower rows are referring to the cases without/with heat conduction and radiative losses.

corona in regions with strong changes of the magnetic connectivity. The measure of the change of the magnetic connectivity in this region the squashing factor indeed shows the region with high squashing factor coincide with the regions of enhanced flux tube volume and temperature enhancement.

5 Discussion and outlook

In this dissertation the simulation results of the heating of X-ray Bright Points (BPs) in the solar corona are presented. To estimate the evolution of plasma and magnetic field on the BP region we used a three-dimensional resistive magnetohydrodynamics (MHD) model, LINMOD3D. The model uses the line-of-sight (LOS) component of magnetic field data from SOHO/MDI magnetograms associated with a BP observed on 19 December 2006 by Hinode. A local-correlation-tracking (LCT) algorithm is applied to derive the velocity patterns responsible for the evolution of the magnetic structures associated to the BP.

The simulation shows that an arc-shaped structure of enhanced temperature forms that is 2-4 times hotter than the background plasma. This structure is located above the two main opposite photospheric magnetic flux concentration. It coincides with the location where the electrical current densities are maximum.

We further examined the contribution of the Lorentz force, pressure gradient force and Joule heating by performing volume integrals in the simulation box that determine the magnetic, kinetic and thermal energy change rates for three different resistivity models. We found that independent on the resistivity model magnetic energy was transformed to kinetic energy through the work done by Lorentz force. Kinetic energy in turn is converted to thermal energy due to pressure gradients that balance the Lorentz force. A comparison of the effect of the three energy conversion through $v \cdot J \times B$, $v \cdot \nabla P$ and ηJ^2 show that adiabatic compression has an important role in temperature increase in the upper corona. This is not dependent on the resistivity model used in the simulation.

Utilizing the concept of differential flux tube integration of the different contributions along the magnetic field lines, a quantitative comparison shows that energy conversion rate, total energies and work done by Lorentz and pressure gradient forces are located in the same flux tubes, also temperature and flux tube volume are maximum at the same place. The results demonstrate the importance of the adiabatic compression in the energy budget of the BP. In comparison, the role of Joule heating was confirmed to be quantitatively small. Therefore, unless there is a convincing argument for using higher values of diffusivity than the already large one used here, Joule heating cannot be considered a viable process for heating.

As a further step toward a more realistic modelling, we studied the changes in the energy budget of this BP after considering two heat loss processes: Heat conduction along the magnetic field lines and radiative loss for the optically thin atmosphere. Including these two plasma transport processes, the local adiabatic compression is not anymore reversible. Furthermore, the heat loss processes result in a significant drop in temperature

(thermal energy).

The heating sites have a similar structure, indicating the dominance of magnetic structure in the dynamic evolution of coronal plasma. Regions of enhanced temperature coincide with the one of enhanced flux tube volume, which are connected to the footpoint motion of the flux tubes that are carrying maximum upward Poynting flux. The strong changes in magnetic connectivity also appears mainly in this regions.

Nevertheless, in the presence of the heat loss effects, one would need to consider some additional heating sources to maintain energy balance and coronal temperature. One way is to consider reflection of Alfvén waves from the transition region, where the angle between the direction of the magnetic field and vertical determines the reflection coefficients. Another possibility is taking into account the heating due to dissipation of Pedersen currents. Applying the model in the regions with stronger magnetic field and, consequently, strong Poynting vector could help to acquire higher values of upward heat flux. Beside the heating sources one could modify the numerical scheme for a longer simulation time, as well as testing application of some artificial viscosity models. It would be also desirable to calculate observable parameters, moving toward a forward modelling.

A Normalization of the energy equation

Energy equation:

$$\frac{\partial p}{\partial t} = -\nabla \cdot p\mathbf{u} - (\gamma - 1)p\nabla \cdot \mathbf{u} + (\gamma - 1)S \quad (\text{A.1})$$

$$\frac{P_0}{\tau_0} \frac{\partial \hat{p}}{\partial \hat{t}} = -\frac{P_0 u_0}{L_0} \nabla \cdot \hat{p}\hat{\mathbf{u}} - (\gamma - 1) \frac{P_0 u_0}{L_0} \hat{p}\nabla \cdot \hat{\mathbf{u}} + (\gamma - 1)S \quad (\text{A.2})$$

$$\frac{\partial \hat{p}}{\partial \hat{t}} = -\nabla \cdot \hat{p}\hat{\mathbf{u}} - (\gamma - 1)\hat{p}\nabla \cdot \hat{\mathbf{u}} + (\gamma - 1)\left(\frac{\tau_0}{P_0}\right)S \quad (\text{A.3})$$

Normalization of the source term:

$$\hat{S} = \left(\frac{\tau_0}{P_0}\right)S = \frac{2 L_0 \mu_0}{v_{A0} B_0^2} (\eta j^2 - \nabla \cdot \mathbf{q} - L_r) \quad (\text{A.4})$$

$$\frac{2 L_0 \mu_0}{v_{A0} B_0^2} \eta j^2 = \frac{2 L_0 \mu_0}{v_{A0} B_0^2} (\mu_0 L_0 v_{A0}) \hat{\eta} \left(\frac{B_0^2}{\eta_0^2 L_0^2}\right) \hat{j}^2 = 2 \hat{\eta} \hat{j}^2 \quad (\text{A.5})$$

$$\frac{2 L_0 \mu_0}{v_{A0} B_0^2} n^2 \chi T^\alpha = \frac{2 L_0 \mu_0}{v_{A0} B_0^2} n_0^2 \hat{n}^2 \chi (T_0 \hat{T})^\alpha = \frac{2 n_0 L_0}{m_p v_{A0}^3} \hat{n}^2 \chi (T_0 \hat{T})^\alpha \quad (\text{A.6})$$

$$\begin{aligned} \frac{2 L_0 \mu_0}{v_{A0} B_0^2} \nabla_{\parallel} \cdot (\kappa_{\parallel} \nabla_{\parallel} T) &= \frac{2 L_0 \mu_0}{v_{A0} B_0^2} \frac{p_0}{2 n_0 \kappa_B L_0^2} \hat{\nabla}_{\parallel} \cdot (\kappa_{\parallel} \hat{\nabla}_{\parallel} \hat{T}) \\ &= \frac{1}{2 v_{A0} n_0 L_0 \kappa_B} \hat{\nabla}_{\parallel} \cdot (\kappa_{\parallel} \hat{\nabla}_{\parallel} \hat{T}) \end{aligned} \quad (\text{A.7})$$

which implies for the transport coefficients:

- $\hat{\kappa}_{\parallel} = \frac{10^{-11} T_0^{\frac{5}{2}}}{2 v_{A0} n_0 \kappa_B L_0} \hat{T}^{\frac{5}{2}} = \frac{10^{-11} (7.2 \cdot 10^4)^{5/2}}{50 \cdot 10^3 \cdot 4 \cdot 10^{-3} \cdot 500 \cdot 10^3} \hat{T}^{\frac{5}{2}} = 0.01 \hat{T}^{\frac{5}{2}}$
- $\hat{\chi} = \frac{2 n_0 L_0}{m_p v_{A0}^3} T_0^\alpha \chi = \frac{2.2 \cdot 10^{15} \cdot 500 \cdot 10^3}{1.67 \cdot 10^{-27} \cdot 50^3 \cdot 10^9} T_0^\alpha \chi = 9.6 \cdot 10^{33} T_0^\alpha \chi$

B Derivation of the energy transport equations

For the volume V , the kinetic, magnetic and thermal energies are:

$$\varepsilon_{kin} = \int_V \frac{1}{2} \rho u^2 d^3v \quad (\text{B.1})$$

$$\varepsilon_{mag} = \int_V \frac{1}{2\mu_0} B^2 d^3v \quad (\text{B.2})$$

$$\varepsilon_{th} = \int_V \frac{P}{\gamma - 1} d^3v \quad (\text{B.3})$$

Kinetic energy

$$\begin{aligned} \frac{1}{2} \frac{\partial \rho u^2}{\partial t} &= \frac{1}{2} u^2 \frac{\partial \rho}{\partial t} + \rho \mathbf{u} \cdot \frac{\partial \mathbf{u}}{\partial t} & (\text{B.4}) \\ &= -\frac{1}{2} u^2 (\nabla \cdot \rho \mathbf{u}) + \rho \mathbf{u} \cdot \frac{\partial \mathbf{u}}{\partial t} \\ &= -\frac{1}{2} u^2 \nabla \cdot \rho \mathbf{u} + \mathbf{u} \cdot \frac{\partial \rho \mathbf{u}}{\partial t} - u^2 \frac{\partial \rho}{\partial t} \\ &= \mathbf{u} \cdot \frac{\partial \rho \mathbf{u}}{\partial t} + \frac{1}{2} u^2 \nabla \cdot \rho \mathbf{u} \\ &= \mathbf{u} \cdot [-\nabla \cdot \rho \mathbf{u} \mathbf{u} - \nabla p + \mathbf{j} \times \mathbf{B}] + \frac{1}{2} u^2 \nabla \cdot \rho \mathbf{u} \\ &= -\frac{1}{2} u^2 \nabla \cdot \rho \mathbf{u} + \mathbf{u} \cdot [\mathbf{u} \times (\nabla \times \mathbf{u}) - \frac{1}{2} \rho \nabla u^2 - \nabla p + \mathbf{j} \times \mathbf{B}] \\ &= -\frac{1}{2} \nabla \cdot \mathbf{u} \rho u^2 - \mathbf{u} \cdot \nabla p + \mathbf{u} \cdot \mathbf{j} \times \mathbf{B} \end{aligned}$$

Magnetic energy

$$\begin{aligned}
 \frac{1}{2\mu_0} \frac{\partial B^2}{\partial t} &= \frac{1}{\mu_0} \mathbf{B} \cdot \frac{\partial \mathbf{B}}{\partial t} & (B.5) \\
 &= -\frac{1}{\mu_0} \mathbf{B} \cdot \nabla \times \mathbf{E} \\
 &= -\frac{1}{\mu_0} \nabla \cdot (\mathbf{E} \times \mathbf{B}) - \mathbf{E} \cdot \mathbf{j} \\
 &= \frac{1}{\mu_0} \nabla \cdot [(\mathbf{u} \times \mathbf{B} - \eta \mathbf{j}) \times \mathbf{B}] + (\mathbf{u} \times \mathbf{B} - \eta \mathbf{j}) \cdot \mathbf{j} \\
 &= \frac{1}{\mu_0} \nabla \cdot [-\mathbf{u} B^2 + (\mathbf{u} \cdot \mathbf{B}) \mathbf{B} - \eta \mathbf{j} \times \mathbf{B}] - \mathbf{u} \cdot \mathbf{j} \times \mathbf{B} - \eta j^2
 \end{aligned}$$

Thermal energy

$$\begin{aligned}
 \frac{1}{\gamma - 1} \frac{\partial p}{\partial t} &= \frac{1}{\gamma - 1} [-\mathbf{u} \cdot \nabla p - \gamma p \nabla \cdot \mathbf{u} \pm \gamma \mathbf{u} \cdot \nabla p] + S & (B.6) \\
 &= -\frac{\gamma}{\gamma - 1} \nabla \cdot p \mathbf{u} + [\mathbf{u} \cdot \nabla p + S]
 \end{aligned}$$

Energy conservation

$$\frac{d\varepsilon_{kin}}{dt} = -\frac{1}{2} \int_{S_V} \rho u^2 \vec{u} \cdot d\vec{s} + \int_V (-\vec{u} \cdot \nabla p + \vec{u} \cdot \vec{j} \times \vec{B}) d^3v \quad (B.7)$$

$$\begin{aligned}
 \frac{d\varepsilon_{mag}}{dt} &= -\frac{1}{\mu_0} \int_{S_V} (-\vec{u} \vec{B}^2 + (\vec{u} \cdot \vec{B}) \vec{B} - \eta \vec{j} \times \vec{B}) \cdot d\vec{s} & (B.8) \\
 &\quad + \int_V (-\vec{u} \cdot \vec{j} \times \vec{B} - \eta j^2) d^3v
 \end{aligned}$$

$$\frac{d\varepsilon_{th}}{dt} = -\frac{\gamma}{\gamma - 1} \int_{S_V} p \vec{u} \cdot d\vec{s} + \int_V (\vec{u} \cdot \nabla p + S) d^3v \quad (B.9)$$

Note that when it is mentioned the source term, S, in the thermal energy equation includes the thermal conduction and radiative loss terms in addition to the Joule heating. Therefore the rate of the thermal energy would be:

- For the case without heat conduction and radiative loss:

$$\frac{d\varepsilon_{th}}{dt} = -\frac{\gamma}{\gamma - 1} \int_{S_V} p \vec{u} \cdot d\vec{s} + \int_V (\vec{u} \cdot \nabla p + \eta j^2) d^3v \quad (B.10)$$

- For the case that includes heat conduction and radiative loss:

$$\frac{d\varepsilon_{th}}{dt} = -\frac{\gamma}{\gamma - 1} \int_{S_V} p \vec{u} \cdot d\vec{s} + \int_V (\vec{u} \cdot \nabla p + \eta j^2 - \nabla_{\parallel} \cdot (\kappa_{\parallel} \nabla_{\parallel} T) - 0.83 \rho^2 \chi T^{\alpha}) d^3v \quad (B.11)$$

C Resistivity values

- Resistivity:

$$\eta_0 = \frac{\nu}{\epsilon_0 \omega_{pe}^2} \quad (C.1)$$

- Anomalous resistivity:

$$\eta_{eff} = \frac{\nu_{eff}}{\epsilon_0 \omega_{pe}^2} \quad (C.2)$$

- Collision frequency:

$$\nu_0 = \frac{ne^4 Ln \Lambda T^{-\frac{3}{2}}}{16\pi \epsilon_0^2 m_e^{\frac{1}{2}} K_B^{\frac{3}{2}}} \quad (C.3)$$

- Effective collision frequency:

$$\nu_{eff} = \frac{\omega_{pe}^2}{2\pi} \quad (C.4)$$

- Using out set of normalization values (table. 3.1):

$$\nu_0 = nT^{-\frac{3}{2}} * 3.419 \cdot 10^{-5} = 3540Hz$$

$$\omega_{pe} = \sqrt{\frac{ne^2}{\epsilon_0 m_e}} = 2.522 \cdot 10^9$$

$$\nu_{eff} = \frac{2.522 * 10^9}{2\pi} = 370MHz$$

$$\epsilon_0 \omega_{pe}^2 = 0.5632 * 10^8$$

$$\eta_0 = \frac{3540}{0.5632 * 10^8} = 6.285 * 10^{-5}$$

$$\eta_{eff} = \frac{370 * 10^6}{0.5632 * 10^8} = 6.569$$

$$\eta_{norm} = \mu_0 L_0 \nu_A = 10^4 \pi$$

$$\eta_0 = \frac{6.285 * 10^{-5}}{10^4 \pi} = 2 * 10^{-9}$$

$$\eta_{eff} = \frac{6.569}{10^4 \pi} = 2.09 * 10^{-4}$$

Bibliography

- Alfven, H., 1947, Existence of electromagnetic-Hydrodynamic Wave, *Nature*, 150, 405-406
- Aschwanden, M. J., 2001, *Physics of the solar corona*, Published in association with Praxis Publishing, Chichester, UK
- Aschwanden, M. J., 2002, 2b, *Particle Acceleration and Kinematics in Solar Flares. A Synthesis of Recent Observations and Theoretical Concepts*, Reprinted from *Space Science Reviews* 101, p.1-227, Kluwer Academic Publishers, Dordrecht, The Netherlands.
- Birn, J., Fletcher, L., Hesse, M., and Neukrich, T., 2009, Energy Release and transfer in solar flares: simulation of three-dimensional reconnection, *The Astrophysical Journal*, 695, 1151-1162
- Birn, J., and Priest, E. R., 2007, *Reconnection of magnetic fields : magnetohydrodynamics and collisionless theory and observations*. [S.l.]: Reconnection of magnetic fields : magnetohydrodynamics and collisionless theory and observations / edited by J. Birn and E. R. Priest. Cambridge : Cambridge University Press, 101, 121
- Brown, D.S., Parnell, C.E., Deluca, E., Gloub, L., & McMullun, R.A. 2001, The Magnetic Structure of a Coronal X-Ray Bright Point, *Sol. Phys.*, 201, 305
- Büchner, J., Nikutowski, B., Otto, A., Coronal heating by transition region reconnection , *Proceedings of the SOHO 15 Workshop - Coronal Heating*. 6-9 September 2004, St. Andrews, Scotland, UK (ESA SP-575), 2004a
- Büchner, J., Nikutowski, B., Otto, A., Magnetic coupling of photosphere and corona: MHD simulation for multi-wavelength observations, *Multi-Wavelength Investigations of Solar Activity*, *Proceedings IAU Symposium*, 223, 353-356, 2004b
- Büchner, J., Nikutowski, B., Otto, A., Solar transition region reconnection, in *Space particle acceleration* (ed. D. Gallagher), 201-212, AGU monograph, Washington, 2004c
- Büchner, J., 2006, Locating current sheets in the solar corona, *Space Science Reviews*, 122, 149-160
- Büchner, J. & Daughton, W., 2007, *Reconnection of Magnetic Fields: Magnetohydrodynamics, Collisionless Theory and Observations*, Cambridge University Press, Cambridge, UK, 144-153

- Büchner, J. & Elkina, N., 2005, Vlasov Code Simulation of Anomalous Resistivity, *Space Sci. Rev.*, 121, 237-252
- Büchner, J. & Elkina, N., 2006, Anomalous resistivity of current-driven isothermal plasmas due to phase space structuring, *Phys. Plasmas*, 13, 082304, 1-9
- Büchner, J., in *New Solar Physics with Solar-B Mission*, Astronomical Society of the Pacific, 369, 407-420, 2007
- Carlsson, M. & Stein, R. F., 1992, Non-LTE radiating acoustic shocks and *CAII* K2V bright points *ApJ* 397, L59
- Carlsson, M. & Stein, R. F., 2002, Dynamic Hydrogen Ionization, *ApJ* 572, 626
- Carlsson, M. & Stein, R. F., 2003, Towards 3D NLTE Radiation Magneto-Hydrodynamics, *ASP Conference Series*, Vol. 288, 505-518
- Cook, J. W., Cheng, C. C., Jacobs, V. L., and Antiochos, S. K., Effect of coronal elemental abundances on the radiative loss function. *APJ*, 338:1176-1183, March 1989. doi: 10.1086/167268.
- De Pontieu, B et al., 2007, Chromospheric Alfvénic Waves Strong Enough to Power the Solar Wind, *Science* 318, 1574
- De Moortel, I., Browning, P., Bradshaw, S. J., Pintt'er, B. and Kontar, E. P., The way forward for coronal heating. *Astronomy and Geophysics*, 49(3):030000-3, June 2008. doi: 10.1111/j.1468-4004.2008.49321.x.
- Gary, G. A., Plasma Beta above a Solar Active Region: Rethinking the Paradigm. *Solar Physics*, 203:71-86, October 2001.
- Golub, L., Krieger, A. S., Silk, J.K., Timothy, A.F., & Vaiana, G. S. 1974, Solar X-Ray Bright Points, *ApJ*, 189, L93
- Gudiksen, B. V., and Nordlund, A., An Ab Initio Approach to the Solar Coronal Heating Problem. *APJ*, 618:1020-1030, January 2005. doi: 10.1086-426063.
- Harvey K. L., 1985, The relationship between coronal bright points as seen in He I Lambda 10830 and the evolution of the photospheric network magnetic fields, *Aust. J. Phys.*, 38, 875
- Hudson, H. S., 1991, Solar flares, microflares, nanoflares, and coronal heating, *Sol. Phys.*, vol. 133, 357-369
- Krieger, R. F., Vaiana, G. S., & van Speybroeck, L. P. 1971, The X-Ray Corona and the Photospheric Magnetic Field, Howard, R. (Ed.), in *solar Magnetic Fields*, IAU Symp., 43, 397
- Landi, E., Del Zanna, G., Young, P.R., Dere, K.P., Mason, H.E., and Landini, M., CHI-ANTI - An atomic database for emission lines - Paper VII: New data for x-rays and other improvements. 162:261, 2006.

- Longcope, D.W. , 1998, A model for current sheets and reconnection in X-ray bright points, *Astrophys. J.*, 507, 433-442
- Lundquist, S. , 1952, Studies in magneto-hydrodynamics, *Arkiv fur Fysik*, Band 5, nr. 15
- Madjarska, M. S., Doyle, J. G., Teriaca, L., & Banerjee, D. 2003, An EUV Bright Point as seen by SUMER, CDS, MDI and EIT on-board SoHO, *A&A*, 398,775
- November, L.J.; Simon, G.W. , 1988, Precise proper-motion measurement of solar granulation, *Astrophys. J.*, 333, 427-442
- Neukrich, T., Dreher J. & Birk G.T., 1997, Three dimensional simulation studies on bright points in the solar corona, *Adv. Space Res.*, 19, No. 12, 1861
- Okamoto, S et al., 2007, Coronal Transverse Magnetohydrodynamic Waves in a Solar Prominence, *Science* 318, 1577
- Otto ,A., Büchner, J., Nikutowski, B. , 2007, Force-free magnetic field extrapolation for MHD boundary conditions in simulations of the solar atmosphere, *Astron.& Astrophys.*, 468, 313-321
- Parker, E.N. , 1972, Topological Dissipation and the Small-Scale Fields in Turbulent Gases, *Astrophys. J.*, 174, 499-510
- Parker, E.N. , 1983, Magnetic Neutral Sheets in Evolving Fields - Part Two - Formation of the Solar Corona, *Astrophys. J.*, 264, 642
- Parker, E.N. , 1988, Nanoflares and the solar X-ray corona, *Ap. J.*, 330, 474
- Peter, H. , 2004, Coronal Heating through Braiding of Magnetic Field Lines, *Ap. J.*, 617, L85-L88
- Peter, H., Gudiksen, B., Nordlund, Å., 2006, Forward Modeling of the Corona of the Sun and Solar-like Stars: From a Three-dimensional Magnetohydrodynamic Model to Synthetic Extreme-Ultraviolet Spectra, *Ap. J.*, 638, 1068
- Parnell, C.E., Priest, E.R, Titov, V.S., 1994, A model for X-ray bright points due to unequal cancelling flux sources, *Solar Physics*, 153, 217-235
- Priest, E. R., 1982, *Solar magneto-hydrodynamics*, D. Reidel Publishing Company, Dordrecht, Holland
- Priest, E.R., Parnell, C.E., Martin, S.F., 1994, A converging flux model of an X-ray bright point and an associated canceling magnetic feature, *Astrophys. J.*, 427, 459-474
- Priest, E. R., and Forbes, T., 2000, *Magnetic reconnection: MHD theory and applications*, CUP, Cambridge
- Potter, D., *Computational physics*, John Wiley & Sons, 1973

- von Rekowski, B., Hood, A.W., 2006a, Solar coronal heating by magnetic cancellation - I. Connected equal bipoles, *Monthly Notices of the Royal Astronomical Society*, 366, 125-136
- von Rekowski, B., Hood, A.W., 2006b, Solar coronal heating by magnetic cancellation - II. Disconnected and unequal bipoles, *Monthly Notices of the Royal Astronomical Society*, 369, 43-56
- von Rekowski, B., and Hood, A. W., 2008, Solar coronal heating by magnetic cancellation - III. Thermodynamics, *Monthly Notices of the Royal Astronomical Society*, 384, 92-986
- Rosner, R., Tucker, W. H. and Vaiana, G.S.Judge, P.G., 1978, Dynamics of the quiescent solar corona, *Astrophys. J.* 220, 643
- Roussev, I.; Galsgaard, K.; Judge, P.G., 2002, Physical consequences of the inclusion of anomalous resistivity in the dynamics of 2D magnetic reconnection, *Astron.&Astrophys.*, 382, 639-649
- Solanki, S. K., Lagg, A., Woch, J., Krupp, N. and Collados, M., 2003, Three-dimensional magnetic field topology in a region of solar coronal heating, *Nature*, 425, 692-695
- Santos, J. C., Büchner, J., Alves, M. V., Nikutowski, B., Zhang, H., 2005, Plasma Flow Velocities Inferred from Photospheric Magnetic Field Observations - a Comparison, *Proceedings of the International Scientific Conference on Chromospheric and Coronal Magnetic Fields (ESA SP-596)*
- Santos, J.C., Büchner, J. 2007, MHD simulation of electric currents in the solar atmosphere caused by photospheric plasma motion, *Astrophys. Space Sci. Trans.*, 3, 29
- Santos, J.C., Büchner, J., Madjarska, M. S., Alves, M. V. 2008, On the relation between DC current locations and an EUV bright point: A case study, *A&A*, 490, 345-352
- Scherrer, N. R. Jr., & Golub, L. 1979, *Sol. Phys.*, 162,129
- Schrijver, C.J. and Zwaan, C. 2000, *Solar and Stellar Magnetic Activity*, Cambridge University Press, Cambridge.
- Silin, I., Büchner, J., Vaivads, A., Anomalous resistivity due to nonlinear lower-hybrid drift waves, *Physics of Plasmas*, Vol 12, Issue 6, pp. 062902-062902-8, 2005
- Spitzer, L. 1962, *Physics of fully ionized Gases* (Interscience, New York)
- Titov, V.S., Hornig, G., and Demoulin, P.: 2002, Theory of magnetic connectivity in the solar corona *J. Geophys. Res.* 107, SSH 3-1
- Tomczyk, S., McIntosh, S. W., Keil, S. L., Judge, P. G., Schad, T., Seeley, D. H., Edmondson, J., 2007, Alfvén Waves in the Solar Corona, *Science* 317, 1192
- Ugarte-Urra, I., Doyle, J. G., Madjarska, M. S., & O'Shea, E. 2004, Signature of oscillations in coronal bright points, *A&A*, 418, 313

- Vaiana, G. S., Krieger, A. S., van Speybroeck, L.P., & Zehnpfennig, T. 1970, *Bull. Am. Phys. Soc.*, 15, 611
- Vernazza, J. E., Avrett, E. H. & Loeser, R, 1981, Structure of the solar chromosphere. III - Models of the EUV brightness components of the quiet-sun, *Astrophys. J. Suppl.*, 45, 635-725
- Warren, H. P., & Winebarger, A. R., 2006, Hydrostatic Modeling of the Integrated Soft X-Ray and Extreme Ultraviolet Emission in Solar Active Regions, *App. J.* 645, 711
- Zhang, J., Kundu, M. R., & White, S. M. 2001, Spatial Distribution and Temporal Evolution of Coronal Bright Points, *Sol. Phys.*, 198, 347

Publications

S. Javadi, J. Büchner, A. Otto and J.C. Santos, "About the relative importance of compressional heating and current dissipation for the formation of coronal X-ray Bright Points", submitted in A& A

Contributions in conferences

- S. Javadi, J. Büchner, A. Otto and J.C. Santos, "Influence of photospheric plasma motion on the pressure and temperature enhancement and the generation of electric currents", DPG Frühjahrstagung, Sun and Heliosphere, Freiburg, March 3-7, 2008
- S. Javadi, J. Büchner, A. Otto and J.C. Santos, "Influence of radiative loss and heat conduction on the temperature variation of a coronal bright point", DPG Frühjahrstagung, Sun and Heliosphere, Bonn, March 15-19, 2010
- S. Javadi, J. Büchner, A. Otto and J.C. Santos, "Relative importance of compressional heating and current dissipation for the formation of coronal X-ray bright points", 38th COSPAR Scientific Assembly, Bremen, Germany, 18-25 July 2010

Acknowledgements

I would like to thank the Max-Planck-Society (MPG) and the Max Planck Institute for Solar System Research (MPS) for financial support of my PHD dissertation and for giving me the opportunity of carrying out this work in the framework of the International Max Planck Research School (IMPRS). In particular, I want to thank the coordinator of the IMPRS, Dieter Schmitt, for his heartily support of the students.

I am thankful to my supervisor from MPS, Prof. J. Büchner, for giving me the chance to work on this interesting project and using an advanced simulation code. I must thank the freedom that he gave me during this three years, as well as his patience and support when I needed.

I must thank my colleague, Jean Santos, for his permanent support during my numerous every day questions. I really appreciate his helps and efforts. I would like to thank also my other colleague, Miraslov Barta, who kindly gave a hand anytime I asked.

Special thanks to Prof. Anonius Otto (from UAF) for discussions about the model during his short visits to MPS, which certainly broaden my knowledge about this topic of work. I very much enjoyed the discussions and I appreciate his patience for explaining things so nicely. I should thank Prof. Büchner again for organizing this visits.

I want to thank my doctoral committee at the University of Göttingen, Prof. Dreizler, Prof. Glatzel, Prof. Kollatschny, Prof. Niemeyer and Prof. Lube for being so helpful and supportive.

I am deeply grateful to Dr. Robert Cameron for his help and support. I thank Dr. Nina Elkina for useful discussions during my first few months of stay in MPS. I am thankful to Dr. Maria Madjatska for the time she kindly spent for introducing me some basic steps of data analysis and also for the motivating, friendly conversations. I thank also Dr. Davina Innes for broadening my insight into the field.

I thank my lovely family and friends for their emotional support. By feeling so connected to them, I always felt protected.

Curriculum Vitae

Persönliche Daten

Name: Setareh Javadi Dohgaheh
Geburtsdatum: Am 19. September, 1982
Geburtsort: Tehran, Iran
Staatsangehörigkeit: Iranische

Studium

09.2000 bis 09.2004: Bachelor in Physics, Shahid Beheshti University,
Tehran, Iran
09.2004 bis 01.2007: M.Sc. Plasma Physics, Shahid Beheshti University,
Tehran, Iran
03.2007 bis 10.2010: Doktorarbeit am Max Planck Institut für
Sonnensystemforschung und Georg-August-Universität
Göttingen, Germany

Schulausbildung

09.1988 - 09.2000: Shahid Beheshti School, Tehran, Iran